Three-dimensional Finite Element Computation of Eddy Currents in Synchronous Machines

Marguerite Touma Holmberg

Technical Report No. 350

1998

Three-dimensional Finite Element Computation of Eddy Currents in Synchronous Machines

by

Marguerite Touma Holmberg

Technical Report No. 350

Submitted to the School of Electrical and Computer Engineering
Chalmers University of Technology
in partial fulfilment of the requirements
for the degree of
Doctor of Philosophy

Department of Electric Power Engineering
Chalmers University of Technology
Göteborg, Sweden
December 1998

CHALMERS UNIVERSITY OF TECHNOLOGY
Department of Electric Power Engineering
S-412 96 Göteborg
ISBN: 91-7197-702-3
ISSN: 0346 - 718X
Chalmers Bibliotek, Reproservice
Göteborg, 1998

Abstract

The thesis deals with the computation of eddy-current losses in the end regions of synchronous machines. Various magnetic and electric vector potential formulations of three-dimensional eddy-current problems are investigated. The equations are discretized by the finite element method with nodal or edge finite elements. Special attention is given to modeling the windings of electrical machines and their contribution to the magnetic field. Two benchmark problems are used to compare the different formulations and finite elements. Hexahedral edge finite elements give more accurate results for a given discretization than nodal finite elements and allow for a reduction of the computational effort necessary to achieve a given accuracy. The accuracy obtained by the different vector potential formulations is roughly the same. An end-region model of a hydrogenerator running at no load has been studied; the magnetic flux densities as well as the eddy-current losses obtained by the different formulations and finite elements have been in good agreement with each other. The end region of a turbogenerator has been investigated in no-load and rated-load operations. The results show that in the end region, the calculated eddy-current losses at load are almost twice those at no load. A synchronous motor with solid pole shoes has been studied during starting, and extensive measurements of the temperature and the magnetic flux density in the end regions have been carried out.

Keywords
Three-dimensional, Finite element method, Eddy currents, Synchronous machines

Preface

The work presented in this thesis was carried out at the Department of Electric Power Engineering at Chalmers University of Technology. The work is a part of a research project financed by the Swedish National Board for Industrial and Technical Development (NUTEK), ABB Generation AB, ABB Corporate Research and ABB Industrial Products. The financial support is gratefully acknowledged.

The project aims at developing numerical methods for solving three-dimensional eddy-current problems, and at applying them to problems in electrical machinery. The part of the work not performed by the author, but necessary to the thesis, is the treatment of the periodic boundary conditions, as well as the anisotropic conductivity and permeability of laminated regions carried out by my project co-worker Sonja Lundmark.

I wish to express my deepest gratitude to Professor Jorma Luomi for supervising this work, for his valuable advice and for persistently revising the manuscript. I also would like to thank Dr. Eero Keskinen for allowing the finite element software written by him to be used as a basis for the implementations performed in this research project. I warmly thank Sonja Lundmark for successful co-operation. This co-operation was on the theory and the software concerning formulations in combination with nodal finite elements in the first half of the project, as well as the measurements in the second half of the project. Furthermore, I owe gratitude to Dr. Ole-Morten Midtgård for fruitful e-mail discussions and all his support. I am also indebted to Holger Persson, Anders Nilsson, Patric Nordkvist and Hans Klåvus (ABB Industrial Products), Dr. Piotr Druzynski and Stig Hjärne (ABB Generation AB), Dr. Stefan Toader, Dr. Karl-Erik Karlsson and Sven Carlsson (ABB Corporate Research) for their help and encouragement. In addition, I would like to thank Dr. Torbjörn Thiringer for helping with the post-processing of the measured data, Dr. Anders Grauers for interesting discussions about phasor diagrams, Kjell Siimon for invaluable help with the computers and the staff at the department for a pleasant working atmosphere. Special thanks to Dr. Hillevi Mattsson, my mentor, and Kerstin Yngvesson, my study adviser.

Last but not least, I would like to thank my family for their supporting contribution to this thesis and for always standing by me. I would also like to thank my husband, the flying doctor, and our coming baby for patiently putting up with my late evenings and long weekends at the department.

CONTENTS

LIST OF SYMBOLS 9

1 INTRODUCTION 13

2 NODAL AND EDGE FINITE ELEMENTS 17
2.1 Nodal Finite Elements 17
2.1.1 Representation of Scalar and Vector Functions Using Nodal Finite Elements 17
2.1.2 Nodal Shape Functions 18
2.1.3 Mapping Global and Local Coordinates 19
2.2 Edge Finite Elements 21
2.2.1 Representation of Vector Functions Using Edge Finite Elements 21
2.2.2 Edge Shape Functions and Their Curls 22
2.2.3 Relationship between Nodal and Edge Shape Functions 25
2.3 Brief review of Edge Finite Elements 26

3 FORMULATIONS OF EDDY-CURRENT PROBLEMS 29
3.1 Equations Defining the Electromagnetic Field Problem 29
3.2 Potentials Describing the Electromagnetic Field 31
3.3 Brief Comparison of Various Formulations 34
3.4 Gauging 36
3.5 Formulations Based on the Electric Vector Potential 39
3.5.1 $\boldsymbol{T}-\Psi, \Psi$ Formulation Using Nodal Basis Functions for Approximating $\boldsymbol{T}$ 39
3.5.2 $\boldsymbol{T}-\Psi, \Psi$ Formulation Using Edge Basis Functions for Approximating $\boldsymbol{T}$ 42
3.6 Formulations Based on the Magnetic Vector Potential 42
3.6.1 $\boldsymbol{A}-V, \Psi$ Formulation Using Nodal Basis Functions for Approximating $\boldsymbol{A}$ 43
3.6.2 $\boldsymbol{A}-V, \Psi$ Formulation Using Edge Basis Functions for Approximating $\boldsymbol{A}$ 45
3.6.3 $\boldsymbol{A}, \Psi$ Formulation 45
3.7 Review of Earlier Work 46

3.8 Discretization of the Equations....51
3.8.1 Discretization of the $\boldsymbol{T}-\Psi, \Psi$ Equations Using Nodal Basis Functions for Approximating $\boldsymbol{T}$....51
3.8.2 Discretization of the $\boldsymbol{T}-\Psi, \Psi$ Equations Using Edge Basis Functions for Approximating $\boldsymbol{T}$....54
3.8.3 Discretization of the $\boldsymbol{A}-V, \Psi$ Equations Using Nodal Basis Functions for Approximating $\boldsymbol{A}$....57
3.8.4 Discretization of the $\boldsymbol{A}-V, \Psi$ Equations Using Edge Basis Functions for Approximating $\boldsymbol{A}$....59
3.9 Iterative Solution of the Equation System....60

4 Computation of the Source Field....63
4.1 Windings of a Turbogenerator....63
4.2 Review of Source-field Calculations....66
4.3 Surface-source Modeling Method....70
4.3.1 Magnetization and Equivalent Current and Charge Densities....70
4.3.2 Equations Defining the Method....71
4.3.3 Computation of the Free-space Field $\boldsymbol{H}_{\mathrm{s}}$ Due to a Coil....72
4.4 Computation of the Free-space Field $\boldsymbol{H}_{\mathrm{s}}$ Due to the Windings of an Electrical Machine....76

5 SAMPLE CALCULATIONS....81
5.1 Program Package....82
5.2 Bath Cube Problem....83
5.2.1 Accuracy of the Field Solution....84
5.2.2 Use of the Computational Resources....87
5.3 Asymmetrical Conductor with a Hole Problem....88
5.3.1 Accuracy of the Field Solution....90
5.3.2 Use of the Computational Resources....95
5.4 Eddy-current Losses in Hydrogenerator End Region....99
5.4.1 Model of the Hydrogenerator....99
5.4.2 Results and Discussion....103
5.5 Eddy-current Losses in Turbogenerator End Region....110
5.5.1 Model of the Turbogenerator....110
5.5.2 Results and Discussion....113
5.6 Asynchronous Starting of a Synchronous Motor....119
5.6.1 Background....119
5.6.2 Measuring System....120

5.6.3 MeasuringEquipment 121
5.6.4 Post-processing 125
5.6.5 Model of the Synchronous Motor 127
5.6.6 Results and Discussion 129

6 CONCLUSIONS 139

REFERENCES 143

APPENDIX TREATMENT OF THE INDETERMINACY OF THE FREE-SPACE FIELD $\boldsymbol{H}_{\mathrm{S}}$ 155

List of symbols

$\boldsymbol{A}$	magnetic vector potential
$\boldsymbol{A}'$	modified magnetic vector potential
$\boldsymbol{a}$	column vector containing the nodal values of the potentials
a	width of a coil
$\boldsymbol{B}$	magnetic flux density
$\boldsymbol{B}_1, \boldsymbol{B}_2$	magnetic flux density at sides 1 and 2 of a surface, respectively
B_{calc}	calculated magnetic flux density
B_{meas}	measured magnetic flux density
$\mathrm{d}l'$	infinitesimal conducting element curve
$\mathrm{d}S'$	infinitesimal conducting element surface
$\mathrm{d}V'$	infinitesimal conducting element volume
$\mathrm{d}l$	infinitesimal element curve
$\mathrm{d}\Gamma$	infinitesimal element surface
$\mathrm{d}\Omega$	infinitesimal element volume
$\boldsymbol{E}$	electric field intensity
e	number of edges in a finite element
$\boldsymbol{f}$	source vector containing the right-hand side of the system of equations
g	side of a coil segment
$\boldsymbol{H}$	magnetic field intensity
$\boldsymbol{H}_1, \boldsymbol{H}_2$	magnetic field intensity at sides 1 and 2 of a surface, respectively
$\boldsymbol{H}_{\mathrm{s}}$	magnetic field produced by a given source current distribution in free space
Im	imaginary part of a vector
i_a, i_b, i_c	currents in the stator winding
i_f	field current referred to the stator winding
i_F	actual field current
$\boldsymbol{i}_s^r$	space vector of the stator current in the rotor reference frame
$\hat{\imath}_s$	stator current amplitude
$\boldsymbol{J}$	current density
$\boldsymbol{J}_{\mathrm{c}}$	source current density
$\boldsymbol{J}_{\mathrm{sc}}$	surface current density
L_d, L_q	direct- and quadrature-axis synchronous inductances, respectively
L_{md}	direct-axis magnetizing inductance
$\boldsymbol{M}$	magnetization vector
$\boldsymbol{M}_1, \boldsymbol{M}_2$	magnetization vectors at sides 1 and 2 of a surface, respectively

m number of nodes in a finite element
$\boldsymbol{N}_{ei}$ edge shape function corresponding to edge i
$\boldsymbol{N}_i$ vector weight function corresponding to node i
N_i nodal shape function corresponding to node i
$\boldsymbol{n}$ unit normal vector directed outward from a considered surface or region
$\boldsymbol{n}_1$, $\boldsymbol{n}_2$ unit normal vectors directed outward from the conducting and non-conducting regions, respectively
$\boldsymbol{n}_{12}$ unit normal vector oriented from side 1 to side 2 of a surface
n_n total number of nodes in the finite element mesh
n_c number of nodes in the conducting region
n_{nc} number of nodes in the non-conducting region
n_e total number of edges in the finite element mesh
n_{ec} number of edges in the conducting region
n_{enc} number of edges in the non-conducting region
$\boldsymbol{P}$ Jacobian matrix
$\boldsymbol{P}^{-1}$ Inverse of the Jacobian matrix
$\boldsymbol{p}$ point within a finite element in the global coordinate system
$\boldsymbol{R}$ vector difference between $\boldsymbol{r}$ and $\boldsymbol{r}'$
Re real part of a vector
R_s stator resistance
R, θ, z cylindrical coordinate system
$\boldsymbol{r}$, $\boldsymbol{r}'$ position vectors defining the field point and the source point, respectively
$\boldsymbol{S}$ matrix where the terms multiplying the potentials are collected
S' surface of one side of a coil segment
surface bounded by curve l' (used in Section 4.2)
$\boldsymbol{s}$ image point of $\boldsymbol{p}$ in the local coordinate system associated to the finite element in question
$\boldsymbol{T}$ electric vector potential
$\boldsymbol{T}_0$ magnetic field whose curl is the source current density $\boldsymbol{J}_c$
t time
$\boldsymbol{U}$ matrix where the terms multiplying the time derivatives of the potentials are collected
$\boldsymbol{u}_s^r$ space vector of the stator voltage in the rotor reference frame
$\hat{u}_s$ stator phase voltage amplitude
$\boldsymbol{V}_\xi$, $\boldsymbol{V}_\eta$, $\boldsymbol{V}_\zeta$ row vectors of $\boldsymbol{P}$
V electric scalar potential
V' current-carrying volume

W^0	finite-dimensional space made of scalars
W^1	finite-dimensional space made of vectors
$\boldsymbol{x}, \boldsymbol{y}, \boldsymbol{z}$	unit vectors of the Cartesian x, y, z coordinate system
$\boldsymbol{x}_1, \boldsymbol{y}_1, \boldsymbol{z}_1$	unit vectors of the Cartesian x_1, y_1, z_1 coordinate system associated to a coil segment
y_{10}	reference point of $\boldsymbol{M}$ in the Cartesian x_1, y_1, z_1 coordinate system
α	angle between the stator current space vector and the d-axis
β	angle between the magnetic axis of phase A and the axis where the finite element model lies
Γ_1	boundary of the conducting region
Γ_2	boundary of the non-conducting region
Γ_{12}	interface between conducting and non-conducting regions
Γ_B	boundary to which the field is parallel
Γ_{B1}	part of Γ_B belonging to the conducting region
Γ_{B2}	part of Γ_B belonging to the non-conducting region
Γ_H	boundary to which the field is perpendicular
Γ_{H1}	part of Γ_H belonging to the conducting region
Γ_{H2}	part of Γ_H belonging to the non-conducting region
γ	angle between the magnetic axis of phase A and the d-axis
δ	load angle
λ_i	barycentric coordinate of node i
μ	magnetic permeability
μ_0	magnetic permeability in free space
μ_1, μ_2	magnetic permeability at sides 1 and 2 of a surface, respectively
ν	scalar function
$\boldsymbol{\xi}, \boldsymbol{\eta}, \boldsymbol{\zeta}$	unit vectors of the Cartesian ξ, η, ζ coordinate system
ρ_c	volume charge density
ρ_{sc}	surface charge density
σ	electrical conductivity
φ	angle of the stator voltage vector with respect to the stator current vector
ψ_s	space vector of the stator flux linkage
Ψ	reduced magnetic scalar potential
Ω	total magnetic scalar potential
Ω_1	conducting region
Ω_2	non-conducting region
ω	angular frequency

Subscripts

d, q	subscripts denoting the direct- and quadrature-axis components
i	subscript denoting node or edge i
im	subscript denoting imaginary component
n	subscript denoting normal component
re	subscript denoting real component
$t1$, $t2$	subscripts denoting tangential components
ti	subscript denoting line integral along edge i
x, y, z	subscripts denoting the Cartesian x, y, z components of a vector
x_1, y_1, z_1	subscripts denoting the Cartesian x_1, y_1, z_1 components of a vector
ξ, η, ζ	subscripts denoting the Cartesian ξ, η, ζ components of a vector

1 Introduction

Varying magnetic fields induce currents in conducting parts of electrical machines. Induced currents are, in many cases, necessary for the operation of these machines, but eddy currents also cause harmful effects: additionallosses and heat generation. The end parts of large synchronous machines are of particular interest, since the losses caused by eddy currents are high. Technical problems due to hot spots may arise, and the economic value of the losses is substantial.

The efficient and economical design of electrical machines requires accurate knowledge of magnetic field distribution. Computer software for solving two-dimensional eddy-current problems is increasingly used in the industry. Although a two-dimensional approximation has proved to be a powerful tool in the analysis of electrical machines, there still remains a variety of problems where it cannot give acceptable results and a three-dimensional analysis is required.The evaluation of, for instance, eddy-current losses in the end regions of electrical machines requires calculationofthree-dimensionalfielddistribution.

Extensive research has been devoted to the numerical solution of three-dimensional eddy-current problems. Several commercial codes are available on the market. The methods are, however, not yet generally applicable to all kinds of problems, and the solution requires plenty of computer resources and human work.

Three-dimensional eddy-current problems can be mathematically formulated in various ways. The variable to be solved may be the field intensity vector, a vector potential, a scalar potential, or a combination of these. A formulation is defined by the choice of the unknown variables and the application of Maxwell's equations supplemented by suitable boundary conditions and additional constraints. Many efforts have been devoted to the study of various formulations and their efficiency in terms of computer resources, since the system of equations to be solved is very large.

The equations of a formulation can be solved by various numerical methods, such as the finite element method, the finite difference method and the boundary element method. The finite element method has become a standard tool for the solution of electrical machine problems. Various finite element types have been developed. Nodal finite elements are widely used. In recent years, edge finite elements have received increasing attention because of several useful properties.

One main property is that they can model the discontinuities of field variables, caused by abrupt changes in electric conductivity and magnetic permeability. Consequently, the formulations can be chosen more freely if edge finite elements are used.

Several problems are encountered when modeling the electromagnetic field of an electrical machine in three dimensions. The magnetic saturation of the iron core makes the equations non-linear. The laminated parts of the iron core are anisotropic, since their permeability and conductivity depend on the direction of the field. The geometry of the end regions is complicated because of the presence of various ferromagnetic and conducting parts for the support of the iron core and, in some cases, for reducing the losses in the supporting structure and iron core. Furthermore, the shape of the end windings is complicated, which makes their modeling a difficult task and their exclusion from the discretization by the finite elements an attractive issue. Thus, for practical purposes, the efficiency of the formulation and its solution, as well as the modeling of the windings, are of crucial importance.

This work deals with linear eddy-current problems and is one part of a research project at the department. The other part of the research project takes into account magnetic saturation. Examples of combining both parts have been published earlier by the research group [1, 2].

The objective of this work is to calculate the eddy-current losses in the end regions of synchronous machines efficiently. Various formulations for the numerical solution of three-dimensional eddy-current problems are investigated and applied to problems in electrical machinery. The accuracy of the solution as well as the computer storage and the CPU time are influenced by both the formulation and the finite element type chosen. Therefore, a comparison of the formulations is made in conjunction with a comparison of the finite elements. Both nodal and edge finite elements are used. Special attention is given to modeling the windings and their contribution to the magnetic field.

Chapter 2 briefly describes the first-order nodal finite elements and the low-order edge finite elements, as well as their properties. The approximations of scalar or vector functions by means of these finite elements are discussed, and the relationship between the approximation spaces of these elements is pointed out. A brief review of edge finite elements is also given.

Chapter 3 describes and compares various ways of formulating three-dimensional eddy-current problems. In addition, the equations are discretized by the finite element method with nodal or edge finite elements.

Chapter 4 illustrates the geometry of the windings of an electrical machine and reviews various methods for modeling a coil and its contribution to the magnetic field. Among these methods, the surface-source modeling method is chosen and described in detail. This method is based on replacing volume distributions of current by means of equivalent distributions of fictitious magnetization, surface currents and charges.

In Chapter 5, various formulations in combination with nodal or edge finite elements are applied to five eddy-current problems. Two benchmark problems from International Eddy Current Workshops are used to compare the formulations, as well as the finite elements. Three problems deal with electrical machinery. The eddy-current losses in the stator end regions of a hydrogenerator and a turbogenerator are evaluated. A synchronous motor with solid pole shoes is studied during starting, and measurements of the temperature and the magnetic flux density in the end regions are presented.

2 Nodal and Edge Finite Elements

The finite element method (FEM) is a numerical technique for finding approximate solutions to partial differential equations. The fundamental idea of the FEM is to subdivide the region to be studied into small subregions called finite elements. This subdivision results in a finite element mesh. The unknown scalar or vector functions to be solved are approximated in each finite element by simple functions called shape functions. A shape function is a continuous function defined over a single finite element. The shape functions of individual finite elements are combined into global shape functions, also called the basis functions.

This chapter deals with nodal and edge finite elements. First-order nodal elements and low-order edge elements are the simplest nodal and edge finite elements, respectively. They are presented in Sections 2.1 and 2.2. Section 2.3 is a literature study of edge finite elements.

2.1 Nodal Finite Elements

2.1.1 Representation of Scalar and Vector Functions Using Nodal Finite Elements

Inside each nodal finite element, a scalar or a vector function is approximated by a linear combination of shape functions associated with nodes. Within an element, a scalar function Ψ is approximated as

$$\Psi = \sum_{i=1}^{m} \Psi_i N_i \tag{2.1}$$

where N_i is the nodal shape function corresponding to node i. The index m is the number of nodes in the element and equal to 8 or 4 depending on whether the element is hexahedral or tetrahedral, respectively. The coefficient Ψ_i — the degree of freedom — is the value of Ψ at node i.

A vector function $\boldsymbol{T}$ is treated simply as three scalar components, T_x, T_y and T_z in a Cartesian x, y, z coordinate system. Each node then has three degrees of freedom instead of one, and $\boldsymbol{T}$ is approximated as

$$\boldsymbol{T} = \sum_{i=1}^{m} \boldsymbol{T}_i \, N_i = \sum_{i=1}^{m} \left(T_{xi} \, \boldsymbol{x} + T_{yi} \, \boldsymbol{y} + T_{zi} \, \boldsymbol{z} \right) N_i \tag{2.2}$$

where the coefficient $\boldsymbol{T}_i$ is the value of $\boldsymbol{T}$ at node i, and T_{xi}, T_{yi} and T_{zi} are the three components of $\boldsymbol{T}_i$. When two elements share a node i, the nodal values $\boldsymbol{T}_i$ at node i are set to be equal. Applying this procedure throughout a mesh makes the vector function $\boldsymbol{T}$ normally and tangentially continuous across all element interfaces.

However, vectors are not simply triplets of numbers. They have a physical and mathematical identity that goes beyond their representation in any particular coordinate frame. By dividingthe vector into three Cartesian parts, node-based elements fail to take this into account. For example, boundary conditions in electromagnetics often take the form of a specification of only the part of the vector function that is tangential to the boundary. With node-based elements, this physical constraint must be transformed into linear relationships between the Cartesian components.

2.1.2 Nodal Shape Functions

The first-order hexahedral and tetrahedral nodal finite elements in the global x, y, z and the local ξ, η, ζ coordinate systems are shown in Figs. 2.1 and 2.2, respectively. $\boldsymbol{p}$ is a point within the element in the global coordinate system, whereas $\boldsymbol{s}$ is the image point of $\boldsymbol{p}$ in the local coordinate system. The numbers on the local element indicate the local ordering of nodes. Reference [3] gives a detailed description of the nodal finite elements.

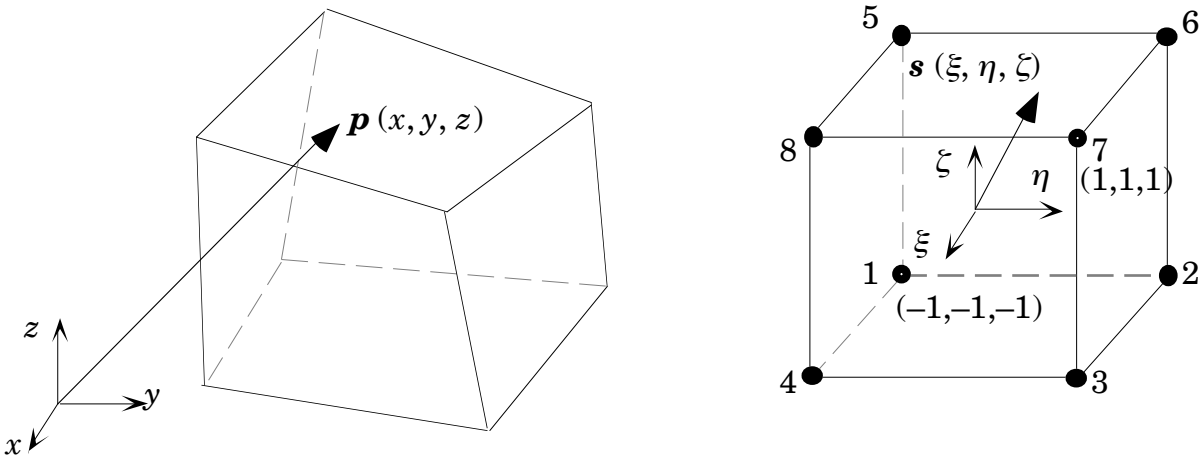

Figure 2.1 First-order hexahedral nodal finite element in global and local coordinates.

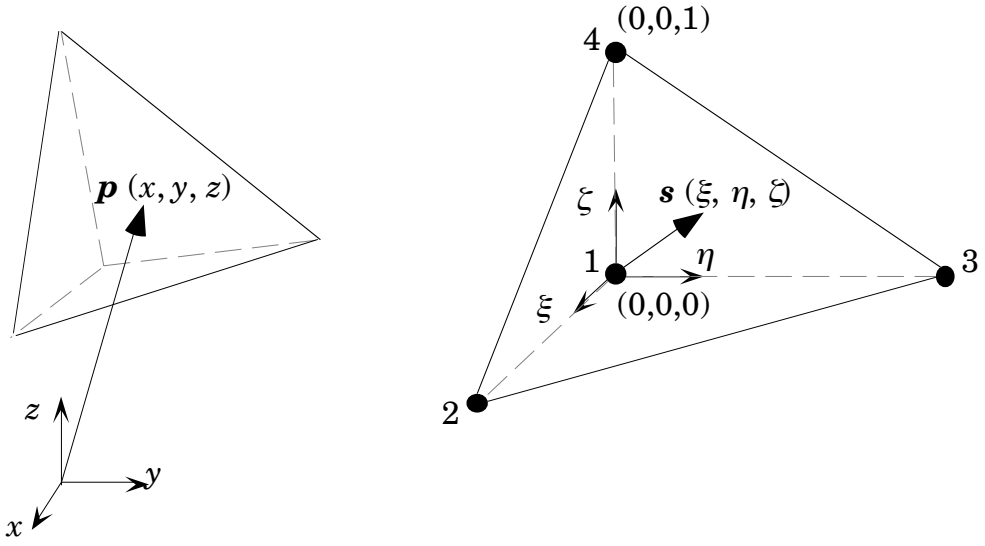

Figure 2.2 First-order tetrahedral nodal finite element in global and local coordinates.

The nodal shape functions in local coordinates for the hexahedral element in Fig. 2.1 can be written as

$$N_i = \frac{1}{8}\left(1+\xi_i\ \xi\right)\left(1+\eta_i\ \eta\right)\left(1+\zeta_i\ \zeta\right) \qquad i = 1, \ldots . 8 \tag{2.3}$$

where (ξ_i, η_i, ζ_i) are the local coordinates of node i. The nodal shape functions in local coordinates for the tetrahedral element in Fig. 2.2 can be written as

$$\begin{aligned} N_1 &= \lambda_1 = 1 \pm \xi \pm \eta \pm \zeta \\ N_2 &= \lambda_2 = \xi \\ N_3 &= \lambda_3 = \eta \\ N_4 &= \lambda_4 = \zeta \end{aligned} \tag{2.4}$$

where λ_1, λ_2, λ_3 and λ_4 are the barycentric coordinates of nodes 1, 2, 3 and 4. Within the hexahedral or tetrahedral finite elements, a nodal shape function N_i equals unity at node i and zero at all other nodes.

2.1.3 Mapping Global and Local Coordinates

Consider the finite elements shown in Figs. 2.1 and 2.2. In the global x, y, z coordinate system, the hexahedral and the tetrahedral elements are seen as the image of the hexahedron and the tetrahedron in the local ξ, η, ζ coordinate system under a tri-linear and a linear coordinate transformation, respectively. These

transformations can be established by the nodal shape functions and are then given by

$$\begin{aligned} x &= \sum_{i=1}^{m} N_i(\xi,\eta,\zeta)\, x_i \\ y &= \sum_{i=1}^{m} N_i(\xi,\eta,\zeta)\, y_i \\ z &= \sum_{i=1}^{m} N_i(\xi,\eta,\zeta)\, z_i \end{aligned} \tag{2.5}$$

where x_i, y_i and z_i are the coordinates of node i in the global coordinate system [3].

When presenting the edge finite elements in the next section, the elements of the Jacobian matrix and its inverse will be present in the expressions of the edge shape functions and their curls. The Jacobian matrix $\boldsymbol{P}$ is introduced by the transformation of the partial derivatives

$$\begin{bmatrix} \frac{\partial N_i}{\partial \xi} \\ \frac{\partial N_i}{\partial \eta} \\ \frac{\partial N_i}{\partial \zeta} \end{bmatrix} = \begin{bmatrix} \frac{\partial x}{\partial \xi} & \frac{\partial y}{\partial \xi} & \frac{\partial z}{\partial \xi} \\ \frac{\partial x}{\partial \eta} & \frac{\partial y}{\partial \eta} & \frac{\partial z}{\partial \eta} \\ \frac{\partial x}{\partial \zeta} & \frac{\partial y}{\partial \zeta} & \frac{\partial z}{\partial \zeta} \end{bmatrix} \begin{bmatrix} \frac{\partial N_i}{\partial x} \\ \frac{\partial N_i}{\partial y} \\ \frac{\partial N_i}{\partial z} \end{bmatrix} = \boldsymbol{P} \begin{bmatrix} \frac{\partial N_i}{\partial x} \\ \frac{\partial N_i}{\partial y} \\ \frac{\partial N_i}{\partial z} \end{bmatrix} \tag{2.6}$$

The left-hand side can be evaluated since the shape functions N_i are specified in the local coordinates. The Jacobian matrix $\boldsymbol{P}$ is a function of the coordinates within the finite element. In terms of the shape functions, $\boldsymbol{P}$ is written as

$$\boldsymbol{P} = \begin{bmatrix} \sum_{i=1}^{m} \frac{\partial N_i}{\partial \xi} x_i & \sum_{i=1}^{m} \frac{\partial N_i}{\partial \xi} y_i & \sum_{i=1}^{m} \frac{\partial N_i}{\partial \xi} z_i \\ \sum_{i=1}^{m} \frac{\partial N_i}{\partial \eta} x_i & \sum_{i=1}^{m} \frac{\partial N_i}{\partial \eta} y_i & \sum_{i=1}^{m} \frac{\partial N_i}{\partial \eta} z_i \\ \sum_{i=1}^{m} \frac{\partial N_i}{\partial \zeta} x_i & \sum_{i=1}^{m} \frac{\partial N_i}{\partial \zeta} y_i & \sum_{i=1}^{m} \frac{\partial N_i}{\partial \zeta} z_i \end{bmatrix} \tag{2.7}$$

The row vectors of $\boldsymbol{P}$ are denoted by

$$\boldsymbol{V}_{\xi} = \frac{\partial x}{\partial \xi}\, \boldsymbol{\xi} + \frac{\partial y}{\partial \xi}\, \boldsymbol{\eta} + \frac{\partial z}{\partial \xi}\, \boldsymbol{\zeta}$$

$$\boldsymbol{V}_\eta = \frac{\partial x}{\partial \eta}\,\boldsymbol{\xi} + \frac{\partial y}{\partial \eta}\,\boldsymbol{\eta} + \frac{\partial z}{\partial \eta}\,\boldsymbol{\zeta} \tag{2.8}$$

$$\boldsymbol{V}_\zeta = \frac{\partial x}{\partial \zeta}\,\boldsymbol{\xi} + \frac{\partial y}{\partial \zeta}\,\boldsymbol{\eta} + \frac{\partial z}{\partial \zeta}\,\boldsymbol{\zeta}$$

The vectors defined in Eq. (2.8) point along the parametric lines, for instance, $\boldsymbol{V}_\xi$ points along the lines of constant η and ζ. By inverting the Jacobian matrix $\boldsymbol{P}$, the global derivatives can be written as

$$\begin{bmatrix} \frac{\partial N_i}{\partial x} \\ \frac{\partial N_i}{\partial y} \\ \frac{\partial N_i}{\partial z} \end{bmatrix} = \begin{bmatrix} \frac{\partial \xi}{\partial x} & \frac{\partial \eta}{\partial x} & \frac{\partial \zeta}{\partial x} \\ \frac{\partial \xi}{\partial y} & \frac{\partial \eta}{\partial y} & \frac{\partial \zeta}{\partial y} \\ \frac{\partial \xi}{\partial z} & \frac{\partial \eta}{\partial z} & \frac{\partial \zeta}{\partial z} \end{bmatrix} \begin{bmatrix} \frac{\partial N_i}{\partial \xi} \\ \frac{\partial N_i}{\partial \eta} \\ \frac{\partial N_i}{\partial \zeta} \end{bmatrix} = \boldsymbol{P}^{-1} \begin{bmatrix} \frac{\partial N_i}{\partial \xi} \\ \frac{\partial N_i}{\partial \eta} \\ \frac{\partial N_i}{\partial \zeta} \end{bmatrix} \tag{2.9}$$

The columns of $\boldsymbol{P}^{-1}$ correspond to the gradients of the local coordinates. The first column, for instance, yields $\nabla\xi$ which is always perpendicular to the planes of constant ξ. Moreover, Eqs. (2.7), (2.8) and (2.9) yield

$$\begin{aligned} \nabla\xi &= \frac{\left(\boldsymbol{V}_\eta \times \boldsymbol{V}_\zeta\right)}{|\boldsymbol{P}|} \\ \nabla\eta &= \frac{\left(\boldsymbol{V}_\zeta \times \boldsymbol{V}_\xi\right)}{|\boldsymbol{P}|} \\ \nabla\zeta &= \frac{\left(\boldsymbol{V}_\xi \times \boldsymbol{V}_\eta\right)}{|\boldsymbol{P}|} \end{aligned} \tag{2.10}$$

2.2 Edge Finite Elements

2.2.1 Representation of Vector Functions Using Edge Finite Elements

Inside each edge finite element, a vector function is approximated by a linear combination of shape functions associated with edges. Within an element, a vector function $\boldsymbol{T}$ is approximated as

$$\boldsymbol{T} = \sum_{i=1}^{e} T_{ti}\,\boldsymbol{N}_{ei} \tag{2.11}$$

where the coefficient T_{ti} is the degree of freedom at edge i and $\boldsymbol{N}_{ei}$ is the edge shape function corresponding to edge i. The index e is the number of edges in the element and is equal to 12 or 6 depending on whether the element is hexahedral or tetrahedral, respectively. The line integral of $\boldsymbol{N}_{ei}$ along edge i equals unity, yielding that the line integral of $\boldsymbol{T}$ along edge i can be written as

$$\int_i \boldsymbol{T} \cdot \mathrm{d}\boldsymbol{l} = \int_i T_{ti}\, \boldsymbol{N}_{ei} \cdot \mathrm{d}\boldsymbol{l} = T_{ti} \tag{2.12}$$

Thus, T_{ti} is the line integral of $\boldsymbol{T}$ along edge i, and the degrees of freedom, instead of being components of the vector function at element nodes, are to be interpreted as the line integrals of the approximated vector function along element edges.

When two elements share an edge i, the degrees of freedom T_{ti} at edge i are set to be equal. Applying this procedure throughout a mesh makes the vector function $\boldsymbol{T}$ tangentially continuous across all element interfaces. The vector function thus constructed is not normally continuous.

2.2.2 Edge Shape Functions and Their Curls

The edge finite element is geometrically the same as its nodal counterpart. Therefore, the mapping of local and global coordinates is as described in Section 2.1.3. Whereas the nodal element has one shape function associated with each of the nodes, the edge element has one shape function for each of the edges. The low-order hexahedral and tetrahedral edge finite elements in the global x, y, z and the local ξ, η, ζ coordinate systems are shown in Figs. 2.3 and 2.4, respectively. The arrows and the numbers on the edges of the global element indicate the direction and the local ordering of edges.

The edge shape functions in local coordinates for the hexahedral element in Fig. 2.3 can be written as

$$\boldsymbol{N}_{ei} = \frac{1}{8}\left(1+\eta_i\ \eta\right)\left(1+\zeta_i\ \zeta\right)\nabla\xi \tag{2.13}$$

Equation (2.13) is given for edges running along ξ where η_i and ζ_i are equal to ± 1 and are the local coordinates of the i-th edge. Cyclic permutations give the shape functions for edges running along η and ζ. The edge shape functions in local coordinates for the tetrahedral element in Fig. 2.4 can be written as

$$\boldsymbol{N}_{ei} = \lambda_k \nabla\lambda_l \pm \lambda_l \nabla\lambda_k \tag{2.14}$$

where edge i goes from node k to node l. Within the hexahedral or tetrahedral finite elements, the line integral of an edge shape function $\boldsymbol{N}_{ei}$ along edge i equals unity and is zero along all other edges.

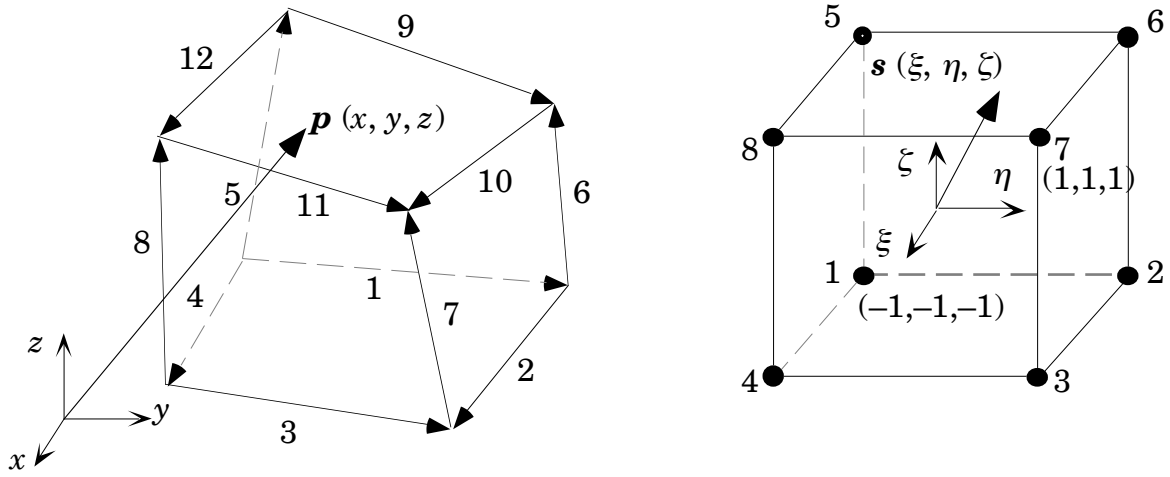

Figure 2.3 Low-order hexahedral edge finite element in global and local coordinates.

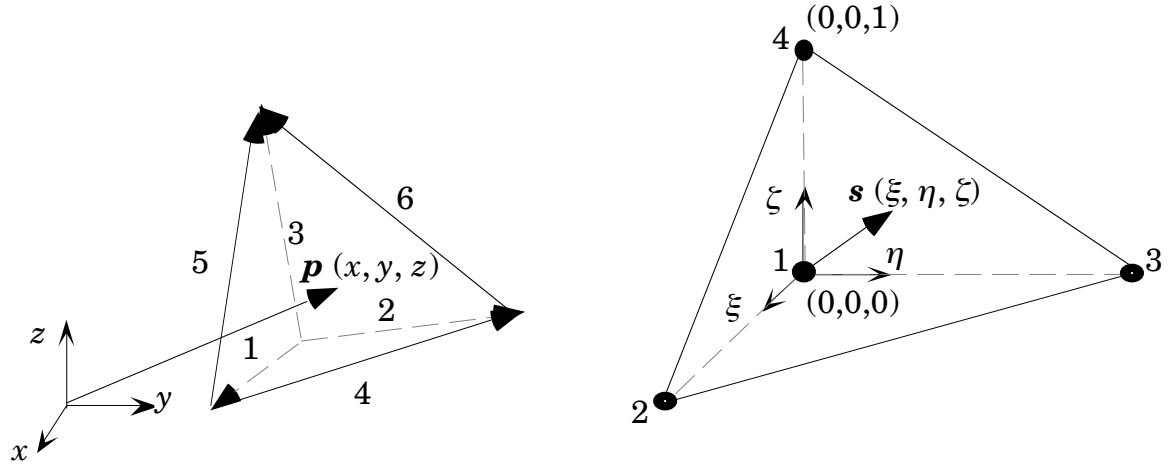

Figure 2.4 Low-order tetrahedral edge finite element in global and local coordinates.

The edge shape functions of the low-order hexahedral and tetrahedral finite elements, as well as their curls, are given in Tables 2.1 and 2.2, respectively. References [4, 5, 6] give a detailed description of the evaluation of these terms. In addition, Dular et al. [6] have shown that the low-order hexahedral edge elements give more accurate solutions than the low-order tetrahedral edge elements since

the hexahedral shape functions are bi-linear and the tetrahedral shape functions are linear. However, the tetrahedral finite elements are useful for modeling complicated geometries.

Table 2.1 The edge shape functions of a low-order hexahedron and their curls.

Edge i	Shape function $\boldsymbol{N}_{ei}$	$\nabla \times \boldsymbol{N}_{ei}$
1	$\frac{1}{8}(1\pm\xi)(1\pm\zeta)\nabla\eta$	$\frac{1}{8\lvert\boldsymbol{P}\rvert}\left[(1\pm\xi)\boldsymbol{V}_{\xi}\pm(1\pm\zeta)\boldsymbol{V}_{\zeta}\right]$
2	$\frac{1}{8}(1+\eta)(1\pm\zeta)\nabla\xi$	$\frac{1}{8\lvert\boldsymbol{P}\rvert}\left[\pm(1+\eta)\boldsymbol{V}_{\eta}\pm(1\pm\zeta)\boldsymbol{V}_{\zeta}\right]$
3	$\frac{1}{8}(1+\xi)(1\pm\zeta)\nabla\eta$	$\frac{1}{8\lvert\boldsymbol{P}\rvert}\left[(1+\xi)\boldsymbol{V}_{\xi}+(1\pm\zeta)\boldsymbol{V}_{\zeta}\right]$
4	$\frac{1}{8}(1\pm\eta)(1\pm\zeta)\nabla\xi$	$\frac{1}{8\lvert\boldsymbol{P}\rvert}\left[\pm(1\pm\eta)\boldsymbol{V}_{\eta}+(1\pm\zeta)\boldsymbol{V}_{\zeta}\right]$
5	$\frac{1}{8}(1\pm\xi)(1\pm\eta)\nabla\zeta$	$\frac{1}{8\lvert\boldsymbol{P}\rvert}\left[\pm(1\pm\xi)\boldsymbol{V}_{\xi}+(1\pm\eta)\boldsymbol{V}_{\eta}\right]$
6	$\frac{1}{8}(1\pm\xi)(1+\eta)\nabla\zeta$	$\frac{1}{8\lvert\boldsymbol{P}\rvert}\left[(1\pm\xi)\boldsymbol{V}_{\xi}+(1+\eta)\boldsymbol{V}_{\eta}\right]$
7	$\frac{1}{8}(1+\xi)(1+\eta)\nabla\zeta$	$\frac{1}{8\lvert\boldsymbol{P}\rvert}\left[(1+\xi)\boldsymbol{V}_{\xi}\pm(1+\eta)\boldsymbol{V}_{\eta}\right]$
8	$\frac{1}{8}(1+\xi)(1\pm\eta)\nabla\zeta$	$\frac{1}{8\lvert\boldsymbol{P}\rvert}\left[\pm(1+\xi)\boldsymbol{V}_{\xi}\pm(1\pm\eta)\boldsymbol{V}_{\eta}\right]$
9	$\frac{1}{8}(1\pm\xi)(1+\zeta)\nabla\eta$	$\frac{1}{8\lvert\boldsymbol{P}\rvert}\left[\pm(1\pm\xi)\boldsymbol{V}_{\xi}\pm(1+\zeta)\boldsymbol{V}_{\zeta}\right]$
10	$\frac{1}{8}(1+\eta)(1+\zeta)\nabla\xi$	$\frac{1}{8\lvert\boldsymbol{P}\rvert}\left[(1+\eta)\boldsymbol{V}_{\eta}\pm(1+\zeta)\boldsymbol{V}_{\zeta}\right]$
11	$\frac{1}{8}(1+\xi)(1+\zeta)\nabla\eta$	$\frac{1}{8\lvert\boldsymbol{P}\rvert}\left[\pm(1+\xi)\boldsymbol{V}_{\xi}+(1+\zeta)\boldsymbol{V}_{\zeta}\right]$
12	$\frac{1}{8}(1\pm\eta)(1+\zeta)\nabla\xi$	$\frac{1}{8\lvert\boldsymbol{P}\rvert}\left[(1\pm\eta)\boldsymbol{V}_{\eta}+(1+\zeta)\boldsymbol{V}_{\zeta}\right]$

Table 2.2 The edge shape functions of a low-order tetrahedron and their curls.

Edge i	Shape function $\boldsymbol{N}_{ei}$	$\nabla \times \boldsymbol{N}_{ei}$
1	$(1\pm\eta\pm\zeta)\nabla\xi+\xi\nabla\eta+\xi\nabla\zeta$	$\frac{2}{\lvert\boldsymbol{P}\rvert}\left[\boldsymbol{V}_{\zeta}-\boldsymbol{V}_{\eta}\right]$
2	$\eta\nabla\xi+(1\pm\xi\pm\zeta)\nabla\eta+\eta\nabla\zeta$	$\frac{2}{\lvert\boldsymbol{P}\rvert}\left[\boldsymbol{V}_{\xi}-\boldsymbol{V}_{\zeta}\right]$

3	$\zeta \nabla\xi + \zeta \nabla\eta + (1 \pm \xi \pm \eta) \nabla\zeta$	$\frac{2}{\lvert \boldsymbol{P} \rvert} \left[\boldsymbol{V}_\eta - \boldsymbol{V}_\xi \right]$
4	$-\eta \nabla\xi + \xi \nabla\eta$	$\frac{2}{\lvert \boldsymbol{P} \rvert} \boldsymbol{V}_\zeta$
5	$-\zeta \nabla\xi + \xi \nabla\zeta$	$\frac{-2}{\lvert \boldsymbol{P} \rvert} \boldsymbol{V}_\eta$
6	$-\zeta \nabla\eta + \eta \nabla\zeta$	$\frac{2}{\lvert \boldsymbol{P} \rvert} \boldsymbol{V}_\xi$

The divergence of the edge shape functions is zero for the low-order tetrahedral finite element [7]. Inside such an element, the vector function approximated by edge basis functions is then divergence free. However, since the normal component of the edge basis functions is free to jump at each of the faces of the finite element, this freedom of divergence within the element does not imply that vector fields approximated by edge basis functions are free of divergence. For a hexahedral finite element, the divergence of the approximated field may be non-zero inside the element because the edge shape functions themselves may have a non-zero divergence [4].

2.2.3 Relationship between Nodal and Edge Shape Functions

Two finite-dimensional spaces, W^0 and W^1, can be associated with a finite element discretization. Space W^0 is made of scalars, whereas space W^1 is made of vectors. The dimension of W^0 is the total number of nodes in the finite element mesh n_n, whereas the dimension of W^1 is the total number of edges in the finite element mesh n_e. The space W^0 is defined as

$$W^0 = \left\{ \Psi \,\middle|\, \Psi(\boldsymbol{p}) = \sum_{i \in n_n} \Psi_i \, N_i(\boldsymbol{p}) \right\} \tag{2.15}$$

The space W^1 is defined as

$$W^1 = \left\{ \boldsymbol{T} \,\middle|\, \boldsymbol{T}(\boldsymbol{p}) = \sum_{i \in n_e} T_{ti} \, \boldsymbol{N}_{ei}(\boldsymbol{p}) \right\} \tag{2.16}$$

The gradient of any function included in W^0 is included in W^1 [8], i.e.,

$$\nabla W^0 = \left\{ \boldsymbol{F} \,\middle|\, \boldsymbol{F} = \nabla \Psi ,\ \Psi \in W^0 \right\} \subset W^1 \tag{2.17}$$

where $\boldsymbol{F}$ is a vector function. This is obvious when comparing, for instance, the hexahedral edge shape function given in Eq. (2.13) and the gradient of the hexahedral nodal shape function written as

$$\begin{aligned} \nabla N_i = \frac{1}{8} \big[& \xi_i \left(1 + \eta_i\ \eta\right)\left(1 + \zeta_i\ \zeta\right) \nabla\ \xi + \\ & \eta_i \left(1 + \zeta_i\ \zeta\right)\left(1 + \xi_i\ \xi\right) \nabla\ \eta + \\ & \zeta_i \left(1 + \xi_i\ \xi\right)\left(1 + \eta_i\ \eta\right) \nabla\ \zeta \big] \end{aligned} \tag{2.18}$$

2.3 Brief review of Edge Finite Elements

As early as 1980, Nedelec [9] introduced some families of finite elements in R^3, one of which, the edge elements, has an important property: the tangential component of a vector function is continuous across the element boundaries whereas this is not necessarily true for the normal component. Later on, Bossavit [8] exposed the relevance of the edge elements introduced by Nedelec to numerical calculations. Webb [10] and Ratnajeevan and Hoole [11] presented a review of edge elements: what they are, and how they have been used in electromagnetics.

An edge element, in contrast to a nodal element, has shape functions with both magnitudes and directions. The low-order edge elements have one degree of freedom at each edge. For a tetrahedral element, the direction of a shape function $\boldsymbol{N}_{ei}$ changes along edge i, but its tangential component remains constant. The tetrahedral low-order edge elements permit a linear interpolation for a vector function in certain spatial directions while in other spatial directions these elements give a constant approximation.

Consistently linear tetrahedral edge elements were first introduced by Mur and De Hoop [12]. These elements belong to a family of finite elements given by Nedelec [13]. Each edge has two degrees of freedom. The direction of a shape function $\boldsymbol{N}_{ei}$ is fixed and its magnitude changes linearly along edge i. This type of elements, the Mur-type, yields a linear approximation of a vector function in all spatial directions. On the other hand, the Mur-type elements rapidly increase the number of degrees of freedom. In order to improve the accuracy of the numerical modeling without a significant increase of the number of degrees of freedom, Ren and Vérité [14] have proposed combining the two tetrahedral edge elements: the low-order and

the Mur-type edge elements, leading to an edge element with a number of degrees of freedom between six and twelve.

Mur [15] has compared the tetrahedral low-order edge elements, consistently linear edge elements and first-order nodal elements. He has concluded that the consistently linear edge element and the nodal element give more accurate solutions than the low-order edge element. As regards the storage requirements, the consistently linear edge element is more than twice as expensive as the nodal element.

Having the Mur-type element, two additional degrees of freedom associated with each face, to which these two unknowns are normal, have been defined in order to provide a linear approximation of the curl of a vector function [16]. This element is called the Lee-type element. The direction and the magnitude of a shape function of the Lee-type element are the same as those of the Mur-type element. Ahagon [17] has introduced another type of first-order triangular edge element, the Ahagon-type. Although the number of degrees of freedom is the same as that of the triangular Lee-type element, the directions of vectorial variables are different. The direction of a shape function $\boldsymbol{N}_{ei}$ of the Ahagon-type element changes along edge i, and its tangential component also changes linearly. Ahagon has discussed the accuracy of the Mur-type, the Lee-type and the Ahagon-type elements. He has concluded that the Lee-type and the Ahagon-type elements have the same accuracy and give more accurate results than the Mur-type element. In addition, the results obtained by means of the Ahagon-type element are not affected by the selection of the direction of the two additional degrees of freedom in contrast to the results obtained by means of the Lee-type element.

Kameari [18] has constructed quadratic hexahedral edge elements. Wang and Ida [19] have presented a systematic method of constructing higher-order edge elements based on nodal elements. Both hexahedral and tetrahedral elements have been presented. In addition, Yioultsis and Tsiboukis [20] have developed a unified theory of higher-order tetrahedral and hexahedral edge elements based on the systematic approach presented in [21].

Coulomb et al. [22] have presented first- and second-order pyramidal edge elements based on pyramidal nodal elements. These new elements can be useful in linking meshes of different types, that is to say hexahedral, tetrahedral and prismatic edge elements.

When the geometry can be modeled with few finite elements, and high accuracy is required, then high-order elements are the best choice. However, when the geometry is more complicated, the use of high-order elements is not always suitable. A large number of finite elements may be requiredsimply to adequately represent the shapes of the devices. It may then not be possible, dependingon the computational resources available, to have every element at the highest order. Hierarchal elements offer the best of both worlds: high-orderelements can be used in regions where high accuracy is required, and low-order elements elsewhere. Webb and Forghani have developed a set of scalar and vector tetrahedral elements [23]. These elements are hierarchal, allowing a mixture of polynomial orders: scalar orders up to 3 and vector orders up to 2. In addition, Midtgård [4] has constructed hierarchal hexahedral edge elements. These elements have given up to second-order approximations for vector functions.

3 Formulations of Eddy-current Problems

3.1 Equations Defining the Electromagnetic Field Problem

In this work, the electromagnetic field problems studied are steady-state, three-dimensional eddy-current problems at power frequencies and in bounded and simply-connected domains. The material properties, i.e., the electric conductivity and the magnetic permeability, can be inhomogeneous and anisotropic but are assumed to be independent of the field. The problems are neither current-forced nor voltage-forced.

At power frequencies and with normal conducting materials, the displacement currents are small compared with the conductive currents. Consequently, the electromagnetic field is described by quasi-static Maxwell's equations. These can be written in their differential form as

$$\nabla \times \boldsymbol{E} = -\frac{\partial \boldsymbol{B}}{\partial t} \tag{3.1}$$

$$\nabla \times \boldsymbol{H} = \boldsymbol{J} \tag{3.2}$$

$$\nabla \cdot \boldsymbol{B} = 0 \tag{3.3}$$

where $\boldsymbol{E}$ is the electric field intensity, $\boldsymbol{H}$ is the magnetic field intensity, $\boldsymbol{B}$ is the magnetic flux density, t is the time and $\boldsymbol{J}$ is the current density. The material properties are defined by the constitutive relations

$$\boldsymbol{B} = \mu \boldsymbol{H} \tag{3.4}$$

$$\boldsymbol{J} = \sigma \boldsymbol{E} \tag{3.5}$$

where μ is the magnetic permeability, and σ is the electrical conductivity. These quantities may be scalars or tensors. Equation (3.2) gives the continuity condition for the current

$$\nabla \cdot \boldsymbol{J} = 0 \tag{3.6}$$

A typical structure of an eddy-current problem with conducting and non-conducting regions is shown in Fig. 3.1. The boundaries of the conducting region Ω_1

and the non-conducting region Ω_2 are denoted by Γ_1 and Γ_2, respectively. The interface between these two regions is denoted by Γ_{12} and is a part of Γ_1 and Γ_2. Coils carrying known source current densities $\boldsymbol{J}_c$ are included in the non-conducting region Ω_2. The arrows illustrate the flow of a magnetic field. These arrows are used to distinguish between the two parts Γ_H and Γ_B of the outer boundary where different conditions apply. Those parts of Γ_1 and Γ_2 which belong to Γ_H are denoted by Γ_{H1} and Γ_{H2}, respectively. Similarly, those parts of Γ_1 and Γ_2 which belong to Γ_B are denoted by Γ_{B1} and Γ_{B2}, respectively.

At the interface Γ_{12}, Maxwell's equations imply continuity conditions on the normal component of the magnetic flux density and on the tangential component of the magnetic field intensity,

$$\boldsymbol{B}_1 \cdot \boldsymbol{n}_1 + \boldsymbol{B}_2 \cdot \boldsymbol{n}_2 = 0 \tag{3.7}$$

$$\boldsymbol{H}_1 \times \boldsymbol{n}_1 + \boldsymbol{H}_2 \times \boldsymbol{n}_2 = \boldsymbol{0} \tag{3.8}$$

where $\boldsymbol{n}_1$ and $\boldsymbol{n}_2$ are the unit normal vectors directed outward from the conducting and the non-conducting regions, respectively.

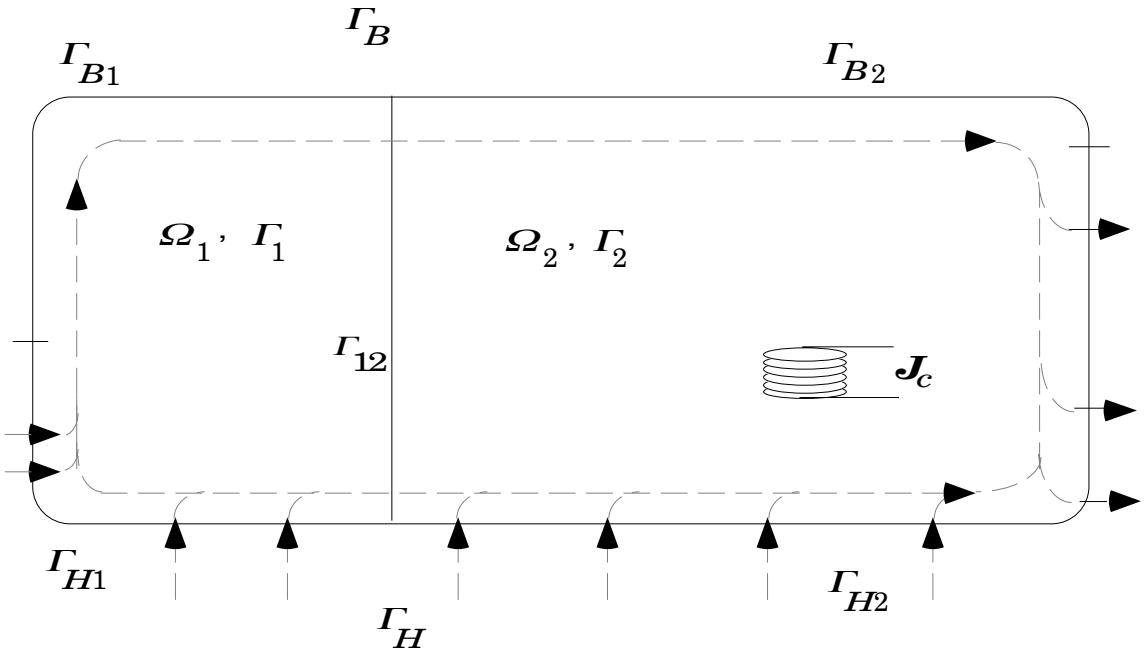

Figure 3.1. Typical structure of an eddy-current problem with conducting and non-conducting regions.

On the outer boundary, three conditions are imposed: the tangential component of the magnetic field intensity is zero on Γ_H

$$\boldsymbol{H} \times \boldsymbol{n} = \boldsymbol{0} \tag{3.9}$$

the normal component of the magnetic flux density is zero on Γ_B

$$\boldsymbol{B} \cdot \boldsymbol{n} = 0 \tag{3.10}$$

and the normal component of the current density is zero on Γ_1

$$\boldsymbol{J} \cdot \boldsymbol{n}_1 = 0 \tag{3.11}$$

where $\boldsymbol{n}$ is the unit normal vector directed outward from the region in question. The boundary and interface conditions are assumed to be homogeneous for the sake of simplicity.

The electromagnetic field problems are described by various field formulations. The variable to be solved may be the field intensity vector, a vector potential, a scalar potential, or a combination of these. A field formulation is defined by the choice of the unknown variables and the application of constitutive equations, as well as quasi-static Maxwell's equations supplemented by appropriate boundary conditions and additional constraints. The finite element method is used to solve the system of equations obtained, and the finite elements used are the first-order nodal elements and the low-order edge elements.

3.2 Potentials Describing the Electromagnetic Field

The electromagnetic field variables $\boldsymbol{H}$ and $\boldsymbol{E}$ can be solved directly, but it is often found to be advantageous to use potentials describing the field. If $\boldsymbol{H}$ or potentials describing $\boldsymbol{H}$ are used as unknowns, the formulations are called magnetic formulations. The magnetic field intensity $\boldsymbol{H}$ is expressed by means of the electric vector potential $\boldsymbol{T}$, the reduced magnetic scalar potential Ψ or the total magnetic scalar potential Ω. Conversely, the electric field intensity $\boldsymbol{E}$ or potentials expressing $\boldsymbol{E}$ are used as unknowns in electric formulations. The magnetic vector potential $\boldsymbol{A}$ and the electric scalar potential V are often used to define $\boldsymbol{E}$. The potentials can be modified and used either separately or together in different regions in order to find a suitable formulation. Various authors use various

notations for the potentials and the formulations. This section presents the notations used in this work.

In the quasi-static approximation, the divergence of the eddy-current density vanishes, Eq. (3.6), which implies the existence of the electric vector potential $\boldsymbol{T}$ defined by

$$\nabla \times \boldsymbol{T} = \boldsymbol{J} \tag{3.12}$$

The magnetic field intensity can be partitioned into two terms

$$\boldsymbol{H} = \boldsymbol{T}_0 + \boldsymbol{H}_{\mathrm{m}} \tag{3.13}$$

where $\boldsymbol{T}_0$ is a magnetic field whose curl is the source current density $\boldsymbol{J}_{\mathrm{c}}$, i.e.,

$$\nabla \times \boldsymbol{T}_0 = \boldsymbol{J}_{\mathrm{c}} \tag{3.14}$$

The vector field $\boldsymbol{T}_0$ is referred to as the source field in this work. The most straightforward choice for $\boldsymbol{T}_0$ is $\boldsymbol{H}_{\mathrm{s}}$, the magnetic field due to the source current density in free space. The magnetic field $\boldsymbol{H}_{\mathrm{m}}$ is the remaining part of the magnetic field intensity $\boldsymbol{H}$.

In the conducting region, no source currents are present and the magnetic field $\boldsymbol{T}_0$ is irrotational. Thus, the comparison of Eqs. (3.2) and (3.12) gives for the magnetic fieldintensity

$$\boldsymbol{H} = \boldsymbol{T}_0 + \boldsymbol{T} - \nabla \Psi \tag{3.15}$$

where Ψ is the reduced magnetic scalar potential. In the non-conducting region, the induced field $\boldsymbol{H}_{\mathrm{m}}$ is irrotational and the magnetic field intensity is given by

$$\boldsymbol{H} = \boldsymbol{T}_0 - \nabla \Psi \tag{3.16}$$

This combination of the potentials is denoted by the $\boldsymbol{T} - \Psi, \Psi$ formulation. The magnetic field intensity in the conducting region may also be given by

$$\boldsymbol{H} = \boldsymbol{T} - \nabla \Omega \tag{3.17}$$

where Ω is the total magnetic scalar potential. Then, the magnetic field intensity in the non-conducting region is expressed as

$$\boldsymbol{H} = -\nabla\Omega \tag{3.18}$$

This combination of the potentials is denoted by the $\boldsymbol{T}-\Omega, \Omega$ formulation.

At the interface of two materials with different permeabilities, the normal component of the magnetic field intensity is discontinuous. In the $\boldsymbol{T}-\Psi, \Psi$ or the $\boldsymbol{T}-\Omega, \Omega$ formulations where $\boldsymbol{T}$ is approximated by nodal basis functions, this discontinuity is included in the magnetic scalar potential, or more precisely, in the jump of the normal derivative of the magnetic scalar potential at the interface. This ensures that the normal component of $\boldsymbol{T}$ can be continuous over the interface. On the other hand, in the $\boldsymbol{T}-\Psi, \Psi$ or the $\boldsymbol{T}-\Omega, \Omega$ formulations where $\boldsymbol{T}$ is approximated by edge basis functions, the discontinuity of the normal component of the magnetic field intensity can be included in the jump of the normal component of $\boldsymbol{T}$ at the interface. This is true since the edge elements allow the normal component of a vector function to jump across the interface of two materials with different permeabilities.

The divergence of the magnetic flux density vanishes, Eq. (3.3), and the magnetic vector potential $\boldsymbol{A}$ may be defined as

$$\nabla \times \boldsymbol{A} = \boldsymbol{B} \tag{3.19}$$

In the conducting region, the electric and the magnetic field depend on each other, and Eq. (3.1) must also be considered. Equation (3.1) together with Eq. (3.19) give for the electric field intensity

$$\boldsymbol{E} = -\frac{\partial \boldsymbol{A}}{\partial t} - \nabla V \tag{3.20}$$

where V is the reduced electric scalar potential. If $\boldsymbol{A}$ is defined in the whole region, the formulation is called the $\boldsymbol{A}-V, \boldsymbol{A}$ formulation. On the other hand, if Ψ, instead of $\boldsymbol{A}$, is defined in the non-conducting region, the formulation is denoted by the $\boldsymbol{A}-V, \Psi$ formulation.

The magnetic vector potential can also be defined so that the electric field intensity is described by the magnetic vector potential alone. The modified magnetic vector potential is, thus, defined as

$$\boldsymbol{A} \mathrel{\textcircled{=}} \boldsymbol{A} + \int_0^t \nabla V \, \mathrm{d}t \tag{3.21}$$

At the interface of two materials with different conductivities, the normal component of the electric field intensity is discontinuous. In the $\boldsymbol{A} - V, \Psi$ formulation where $\boldsymbol{A}$ is approximated by nodal basis functions, this discontinuity is included in the electric scalar potential V, or more precisely, in the jump of the normal derivative of V at the interface. This ensures that the normal component of $\boldsymbol{A}$ can be continuous over the interface. On the other hand, in the $\boldsymbol{A} - V, \Psi$ formulation where $\boldsymbol{A}$ is approximated by edge basis functions, the discontinuity of the normal component of the electric field intensity can be included in the jump of the normal component of $\boldsymbol{A}$ at the interface.

If the conductivity is homogeneous, the normal component of $\boldsymbol{A}$ can also be continuous without the use of V, and the electric scalar potential can be eliminated. This idea has first been applied to the $\boldsymbol{A} \textcircled{\scriptstyle \psi} \Psi$ formulation which is obtained by using $\boldsymbol{A}'$ [24, 25, 26]. Another way of eliminating V is to set V equal to zero resulting in the $\boldsymbol{A}, \Psi$ formulation [27].

3.3 Brief Comparison of Various Formulations

The formulations used for solving eddy-current problems are usually based either on the electric vector potential $\boldsymbol{T}$, such as the $\boldsymbol{T} - \Psi, \Psi$ and the $\boldsymbol{T} - \Omega, \Omega$ formulations, or on the magnetic vector potential $\boldsymbol{A}$, such as the $\boldsymbol{A} - V, \boldsymbol{A}$, the $\boldsymbol{A} - V, \Psi$ and the $\boldsymbol{A}, \Psi$ formulations. A comparison of various formulations concerning the degrees of freedom can be seen in Table 3.1. The scalar potentials are approximated by nodal basis functions, whereas the vector potentials are approximated either by nodal basis functions or by edge basis functions.

Table 3.1 Comparison of various formulations concerning the degrees of freedom.

Formulations	Potentials in the non-conducting region	Potentials in the conducting region when nodal elements are used	Potentials in the conducting region when edge elements are used
$\boldsymbol{T}-\Omega,\Omega$	Ω	T_x, T_y, T_z and Ω	T_{ti} and Ω
$\boldsymbol{T}-\Psi,\Psi$	Ψ	T_x, T_y, T_z and Ψ	T_{ti} and Ψ
$\boldsymbol{A}-V,\boldsymbol{A}$	A_x, A_y and A_z when nodal elements are used A_{ti} when edge elements are used	A_x, A_y, A_z and V	A_{ti} and V
$\boldsymbol{A}-V,\Psi$	Ψ	A_x, A_y, A_z and V	A_{ti} and V
$\boldsymbol{A},\Psi$	Ψ	A_x, A_y, A_z	A_{ti}

The use of the magnetic vector potential approximated by nodal basis functions in the non-conducting region requires three components of $\boldsymbol{A}$ to be solved. Furthermore, the use of $\boldsymbol{A}$ in the non-conducting region necessitates the inclusion of the coils in the discretization, which increases the number of unknowns and complicates the construction of the finite element mesh, especially in the presence of coils of geometrically complex shapes.

The use of the reduced magnetic scalar potential in the non-conducting region reduces the number of degrees of freedom from three components for $\boldsymbol{A}$ to one component for Ψ, when $\boldsymbol{A}$ is approximated by nodal basis functions. Consequently, computational costs are reduced. In addition, Ψ allows us to exclude the current sources in the non-conducting region from the discretization by evaluating the vector field $\boldsymbol{T}_0$, defined by Eq. (3.14). This is an important advantage of reducing the number of unknowns.

In the non-conducting region where Ψ is defined, the rotational part of the magnetic field produced by the given source current distribution in free space is modelled by the field $\boldsymbol{H}_s$. If $\boldsymbol{H}_s$ is approximated by nodal basis functions, then cancellation problems can occur in high-permeability regions [28]. In such regions, the magnetic field intensity $\boldsymbol{H}$ is close to zero. The approximated field $\boldsymbol{H}_s$ contains polynomial terms not present in the solution space of $-\nabla\Psi$, since $-\nabla\Psi$ and $\boldsymbol{H}_s$ lie in different approximation spaces. Consequently, $-\nabla\Psi$ cannot cancel the approximated field $\boldsymbol{H}_s$ as it should have done, and $-\nabla\Psi$ and the approximated field $\boldsymbol{H}_s$ are nearly equal in magnitude and opposite in direction.

The cancellation problems can be avoided by using a total scalar potential in high-permeability regions [29, 30], by approximating $\boldsymbol{H}_s$ by means of the edge basis functions or by an edge element representation of $\boldsymbol{T}_0$, which is usually carried out by using Ampère's law [31, 32, 33].

The use of the total magnetic scalar potential in the non-conducting region comprising the current sources also necessitates the inclusion of these sources in the discretization. Nakata et al. [34] have enforced a constant and uniformly distributed current density by assuming that a low-conducting material is placed between the coil sides. Since the current density is equal to the curl of the vector potential, Eq. (3.12), $\boldsymbol{T}$ is distributed uniformly in the low-conducting material and linearly in the current sources. The $\boldsymbol{T}-\Omega,\Omega$ formulation is effective when the shape of the current sources is simple. For current sources of complicated shapes, this procedure may become cumbersome.

The electric vector potential formulations show a distinct advantage when solving the field in laminated regions. Since the eddy currents induced in laminated regions flow only in a plane parallel to the laminations, the components of $\boldsymbol{T}$ that are tangential to the laminations may be omitted according to Eq. (3.12), thus, reducing the number of degrees of freedom.

3.4 Gauging

The definitions of the vector and scalar potentials presented in Section 3.2 are sufficient to define the field variables uniquely, but they leave the potentials themselves non-unique [35]. A scalar potential is made unique by fixing the value of the potential somewhere in the problem region, in case no Dirichlet boundary condition on the scalar potential is present.

As pertains to the use of nodal finite elements, a vector potential can be made unique by satisfying a divergence condition in the whole conducting region and by determining the normal or the tangential component of the vector potential on the boundary of the conducting region [36]. The Coulomb gauge is a widely applied divergence condition which is written for the electric and the magnetic vector potentials as

$$\nabla \cdot \boldsymbol{T} = 0 \tag{3.22}$$

$$\nabla \cdot \boldsymbol{A} = 0 \tag{3.23}$$

Another divergence condition is the Lorentz gauge, which is written for the electric and the magnetic vector potentials as

$$\nabla \cdot \boldsymbol{T} = \sigma \mu \frac{\partial \Psi}{\partial t} \tag{3.24}$$

$$\nabla \cdot \boldsymbol{A} = \pm \sigma \mu V \tag{3.25}$$

The choice between determining the normal or the tangential component of the vector potential on the boundary of the conducting region depends on the potential and on the physical boundary condition applied to the boundary. The boundary condition of the electric vector potential is determined by Eq. (3.11), which is given by

$$\boldsymbol{n}_1 \times \boldsymbol{T} = \boldsymbol{0} \tag{3.26}$$

on Γ_1. Equation (3.26) is a Dirichlet boundary condition valid for both gauges [37].

The boundary conditions of the magnetic vector potential are determined by Eqs. (3.9) and (3.10). On Γ_{B1}, the condition (3.10) is written as the Dirichlet boundary condition

$$\boldsymbol{n}_1 \times \boldsymbol{A} = \boldsymbol{0} \tag{3.27}$$

which is valid for both gauges [38]. On Γ_{H1}, the condition (3.9) is expressed as [27]

$$\boldsymbol{n}_1 \times \frac{1}{\mu} \nabla \times \boldsymbol{A} = \boldsymbol{0} \tag{3.28}$$

Moreover, on Γ_{12}, the tangential component of the magnetic field intensity is continuous, Eq. (3.8). This interface condition is described by the reduced magnetic scalar potential used in the non-conducting region. The condition, $\boldsymbol{n}_1 \cdot \boldsymbol{A} = 0$, is applied to the magnetic vector potential on Γ_{12} and Γ_{H1} [27, 37]. Thus, on $\Gamma_{H1} \cup \Gamma_{12}$

$$\boldsymbol{n}_1 \cdot \boldsymbol{A} = 0 \tag{3.29}$$

$$\boldsymbol{n}_1 \cdot \boldsymbol{A} = k^2 \, V \tag{3.30}$$

have to be specified for the Coulomb and the Lorentz gauges, respectively, where k is a real constant.

As pertains to the use of edge finite elements, the edge basis functions span a space of the dimension n_e. This space can be separated into two sub-spaces: a sub-space for the tree edges and a sub-space for the co-tree edges. The definitions of a tree and a co-tree necessitate defining a graph. A graph describes the topology of a finite element mesh and consists of the nodes and the edges connecting the nodes. A tree is a graph that has a path from any node to any other node and has no cycles. If the tree contains all the nodes in the graph, it is called a spanning tree. The rest of the edges of the graph then form a co-tree. Reference [39] gives more details about the graphs, trees and the co-trees.

Splitting the space spanned by the edge basis functions corresponds to splitting the graph into a spanning tree and a co-tree. The tree space is of the dimension n_n–1 and contains functions of the form ∇h only, where h is a scalar. The co-tree space is of the dimension n_e–n_n+1 and contains no functions of the form ∇h. Consequently, a vector function, such as $\boldsymbol{T}$ can be separated into two parts

$$\boldsymbol{T} = \boldsymbol{T}_{\mathrm{c}} + \nabla h \tag{3.31}$$

where $\boldsymbol{T}_{\mathrm{c}}$ is the part of $\boldsymbol{T}$ lying in the co-tree space. Specifying ∇h yields a unique $\boldsymbol{T}_{\mathrm{c}}$ and, thus, a unique $\boldsymbol{T}$ for a given $\boldsymbol{J}$. The vector potential $\boldsymbol{T}$ is gauged by setting ∇h to zero. Thus, the function space of solutions is restricted to contain no functions of the form ∇h. This gauging procedure, called the tree-gauge method, is the equivalent of imposing the gauge condition

$$\boldsymbol{T} \cdot \boldsymbol{u} = 0 \tag{3.32}$$

where $\boldsymbol{u}$ is a prescribed auxiliary vector field which does not possess closed field lines [40]. The direction of $\boldsymbol{u}$ is identified along an arbitrary tree of the graph, connecting all the nodes without forming closed loops. Thus, the tree-gauge method can be implemented by simply eliminating the degrees of freedom associated with the edges of the tree. The tree-gauge method was introduced by Albanese and Rubinacci [41, 42].

3.5 Formulations Based on the Electric Vector Potential

The $\boldsymbol{T}-\Omega,\Omega$ and the $\boldsymbol{T}-\Psi,\Psi$ formulations are the chosen electric vector potential formulations in this work. These formulations are based on $\boldsymbol{T}$ and either Ω or Ψ in the conducting region and only Ω or Ψ in the non-conducting region. The scalar potentials Ω and Ψ are approximated by nodal basis functions, whereas the vector potential $\boldsymbol{T}$ is approximated either by nodal basis functions or by edge basis functions. For the sake of brevity, Sections 3.5.1 and 3.5.2 present the $\boldsymbol{T}-\Psi,\Psi$ formulation when $\boldsymbol{T}$ is approximated by nodal basis functions and edge basis functions, respectively.

3.5.1 $\boldsymbol{T}-\Psi,\Psi$ Formulation Using Nodal Basis Functions for Approximating $\boldsymbol{T}$

In the $\boldsymbol{T}-\Psi,\Psi$ formulation, $\boldsymbol{T}$ is defined by Eq. (3.12) whereas Ψ is defined by Eq. (3.15) in the conducting region and by Eq. (3.16) in the non-conducting region. In the conducting region, Eq. (3.1) remains to be solved. Substituting Eqs. (3.5) and (3.12) in Eq. (3.1) and considering the constitutive equation (3.4) and the relationship (3.15) give

$$\nabla\times\left(\frac{1}{\sigma}\nabla\times\boldsymbol{T}\right)+\mu\left(\frac{\partial\boldsymbol{T}_0}{\partial t}+\frac{\partial\boldsymbol{T}}{\partial t}-\nabla\frac{\partial\Psi}{\partial t}\right)=\boldsymbol{0} \tag{3.33}$$

By taking the divergence on both sides of Eq. (3.33), the solenoidality of the magnetic flux density (3.3) is satisfied. The vector potential $\boldsymbol{T}$ is approximated by nodal basis functions. In order to ensure the uniqueness of $\boldsymbol{T}$, a divergence condition is applied. This is done by adding a penalty term to the original equation (3.33), as presented by Biro and Preis in [43]. Equation (3.33) is, thus, replaced by

$$\nabla\times\left(\frac{1}{\sigma}\nabla\times\boldsymbol{T}\right)-\nabla\left(\frac{1}{\sigma}\nabla\cdot\boldsymbol{T}\right)+\mu\left(\frac{\partial\boldsymbol{T}_0}{\partial t}+\frac{\partial\boldsymbol{T}}{\partial t}-\nabla\frac{\partial\Psi}{\partial t}\right)=\boldsymbol{0} \tag{3.34}$$

where the second term is the penalty term. By taking the divergence on both sides of Eq. (3.34), the solenoidality of the magnetic flux density (3.3) is not satisfied due to the penalty term. Thus, the solenoidality of the flux density

$$\nabla\cdot\mu\left(\boldsymbol{T}_0+\boldsymbol{T}-\nabla\Psi\right)=0 \tag{3.35}$$

and the boundary condition (3.10) on Γ_{B1}

$$\boldsymbol{n}_1 \cdot \mu \left(\boldsymbol{T}_0 + \boldsymbol{T} - \nabla \Psi \right) = 0 \tag{3.36}$$

are required. On Γ_{B1}, Eq. (3.36) is improved by applying a homogeneous Dirichlet condition to the normal component of the electric vector potential [44].

If the Coulomb gauge is satisfied in the whole region, then Eqs. (3.33) and (3.34) are equivalent and the inclusion of the additional term in Eq. (3.34) is justified. The satisfaction of the Coulomb gauge in the whole region is done by fulfilling the homogeneous Dirichlet boundary condition on Γ_1 [27]

$$\frac{1}{\sigma} \nabla \cdot \boldsymbol{T} = 0 \tag{3.37}$$

Equations (3.9), (3.15) and (3.26) give the boundary condition for Ψ on Γ_{H1}

$$\boldsymbol{n}_1 \times \left(\boldsymbol{T}_0 - \nabla \Psi \right) = \boldsymbol{0} \tag{3.38}$$

Equation (3.38) can be integrated to give the value of the reduced magnetic scalar potential in an arbitrary point on the surface Γ_{H1}

$$\Psi = \Psi_0 + \int_{p_1}^{p_2} \boldsymbol{T}_0 \cdot d\boldsymbol{l} \tag{3.39}$$

which is an inhomogeneous Dirichlet boundary condition with p_2 as the considered point on Γ_{H1} where Ψ is to be determined, and p_1 as the reference point on Γ_{H1} where $\Psi = \Psi_0$.

In the non-conducting region, Eqs. (3.3), (3.4) and (3.16) give

$$\nabla \cdot \mu \left(\boldsymbol{T}_0 - \nabla \Psi \right) = 0 \tag{3.40}$$

Equations (3.4), (3.10) and (3.16) give the boundary condition for Ψ on Γ_{B2}

$$\boldsymbol{n}_2 \cdot \mu \left(\boldsymbol{T}_0 - \nabla \Psi \right) = 0 \tag{3.41}$$

Equations (3.9) and (3.16) give the boundary condition for Ψ on Γ_{H2}

$$\boldsymbol{n}_2 \times \left(\boldsymbol{T}_0 - \nabla \Psi \right) = \boldsymbol{0} \tag{3.42}$$

Eq. (3.42) can be integrated to give the value of the reduced magnetic scalar potential on Γ_{H2}. This integration is obtained by Eq. (3.39).

The interface conditions (3.7) and (3.8) have to be satisfied on Γ_{12}. Substituting Eqs. (3.4), (3.15) and (3.16) into Eqs. (3.7) and (3.8) gives

$$\boldsymbol{n}_1 \cdot \mu_1 \left(\boldsymbol{T}_0 + \boldsymbol{T} - \nabla \Psi \right) + \boldsymbol{n}_2 \cdot \mu_2 \left(\boldsymbol{T}_0 - \nabla \Psi \right) = 0 \tag{3.43}$$

$$\boldsymbol{n}_1 \times \left(\boldsymbol{T}_0 + \boldsymbol{T} - \nabla \Psi \right) + \boldsymbol{n}_2 \times \left(\boldsymbol{T}_0 - \nabla \Psi \right) = \boldsymbol{0} \tag{3.44}$$

In the discretization of the equations by the finite element method, Eq. (3.43) is satisfied implicitly. The continuity of the reduced magnetic scalar potential across Γ_{12} together with Eq. (3.26) ensure that Eq. (3.44) is satisfied. The differential equations (3.34), (3.35), (3.40), the interface condition (3.43) and the boundary conditions (3.39) on Γ_{H1} and Γ_{H2}, (3.26), (3.36), (3.37), (3.41) are the equations applied in the $\boldsymbol{T} - \Psi, \Psi$ formulation.

A laminated region implies that the permeability and the conductivity in this region are dependent on the direction of the field. Hence, a laminated region is anisotropic. Chapter 4 in [1] gives a detailed description of the treatment of anisotropic conductivity and permeability. In laminated regions, the electric anisotropy is treated by fulfilling

$$T_{t1} = T_{t2} = 0 \tag{3.45}$$

where T_{t1} and T_{t2} are the components of $\boldsymbol{T}$ tangential to the laminated sheets [45]. The conductivity in the tangential directions is then assumed to be a scalar.

In laminated regions, the permeability must be represented by a tensor in order to take into account magnetic anisotropy. For instance, by assuming the laminations to be in the xy or yz or xz-plane, the permeability tensor can be written as

$$\mu = \begin{bmatrix} \mu_x & 0 & 0 \\ 0 & \mu_y & 0 \\ 0 & 0 & \mu_z \end{bmatrix} \tag{3.46}$$

where μ_x, μ_y and μ_z are the permeability components in the x-, y- and z-directions.

3.5.2 $\boxed{T-\Psi,\Psi}$ Formulation Using Edge Basis Functions for Approximating T

When the $T-\Psi,\Psi$ formulation is used and the vector potential T is approximated by edge basis functions, Eq. (3.33) must be solved in the conducting region. In order to ensure the uniqueness of T, the tree-gauge method described in Section 3.4 is applied.

The boundary condition (3.26) is satisfied by eliminating the degrees of freedom associated with the edges of the tree and the co-tree on Γ_1. Therefore, it is essential that all the co-tree edges of Γ_1 are closed by the tree edges also lying on Γ_1 [41]. In addition, the boundary conditions (3.36) and (3.39) are required. The second term in the right-hand side of Eq. (3.39) is integrated along the edges of the finite element mesh.

In the non-conducting region, the differential equation and the boundary conditions applied are the same as those presented in Section 3.5.1, since the scalar potential Ψ is approximated by nodal basis functions. Furthermore, the interface conditions (3.43) and (3.44) are also valid here, and are satisfied in accordance with the discussion presented in Section 3.5.1.

In laminated regions, the electric anisotropy is treated by fulfilling Eq. (3.45). When edge elements are used, the line integrals of T along the edges are the degrees of freedom. Consequently, by using hexahedral elements where all the edges are orthogonal to each other, Eq. (3.45) is fulfilledby treating the edges lying in the plane of the laminated sheets as tree edges. On the other hand, by using tetrahedral elements or hexahedral elements where the edges are not orthogonal to each other, the anisotropic conductivity cannot be treated. This is because the conductivity in these cases has to be explicitly set to zero in the direction normal to the laminated sheets, which is impossible because of the first term in Eq. (3.33). Magnetic anisotropy is taken into account by representing the permeability by the diagonal tensor (3.46).

3.6 Formulations Based on the Magnetic Vector Potential

The $\boxed{A-V,\Psi}$ and the A,Ψ formulations are the chosen magnetic vector potential formulations in this work. These formulations are based on A and V (V is eliminated in the A,Ψ formulation) in the conducting region and only Ψ in the non-

conducting region. The scalar potentials V and Ψ are approximated by nodal basis functions, whereas the vector potential $\boldsymbol{A}$ is approximated either by nodal basis functions or by edge basis functions.

In the non-conducting region where Ψ is defined, the differential equation and the boundary conditions applied are the same as those presented in Section 3.5.1. Furthermore, in laminated regions, the permeability is represented by the diagonal tensor (3.46).

3.6.1 $\boldsymbol{A}$ – V, Ψ Formulation Using Nodal Basis Functions for Approximating $\boldsymbol{A}$

In the $\boxed{\boldsymbol{A}-V,\Psi}$ formulation, $\boldsymbol{A}$ and V are defined by Eqs. (3.19) and (3.20), respectively. In the conducting region, Eq. (3.2) remains to be solved. Considering the constitutive equations (3.4) and (3.5) and substituting Eqs. (3.19) and (3.20) into Eq. (3.2) yield

$$\nabla \times \left(\frac{1}{\mu} \nabla \times \boldsymbol{A} \right) + \sigma \frac{\partial \boldsymbol{A}}{\partial t} + \sigma \nabla V = \boldsymbol{0} \tag{3.47}$$

By taking the divergence on both sides of Eq. (3.47), the solenoidality of the current density (3.6) is satisfied. The vector potential $\boldsymbol{A}$ is approximated by nodal basis functions. In order to ensure the uniqueness of $\boldsymbol{A}$, a divergence condition is applied. This is done by adding a penalty term to the original equation (3.47), as presented by Biro and Preis in [27]. Equation (3.47) is, thus, replaced by

$$\nabla \times \left(\frac{1}{\mu} \nabla \times \boldsymbol{A} \right) - \nabla \left(\frac{1}{\mu} \nabla \cdot \boldsymbol{A} \right) + \sigma \frac{\partial \boldsymbol{A}}{\partial t} + \sigma \nabla V = \boldsymbol{0} \tag{3.48}$$

where the second term is the penalty term. By taking the divergence on both sides of Eq. (3.48), the solenoidality of the current density (3.6) is not satisfied due to the penalty term. Thus, the solenoidality of the current density

$$\nabla \cdot \left(- \sigma \frac{\partial \boldsymbol{A}}{\partial t} - \sigma \nabla V \right) = 0 \tag{3.49}$$

and the boundary condition (3.11) on Γ_1

$$\boldsymbol{n}_1 \cdot \left(- \sigma \frac{\partial \boldsymbol{A}}{\partial t} - \sigma \nabla V \right) = 0 \tag{3.50}$$

arerequired.

Similar to the $\boldsymbol{T} - \Psi, \Psi$ formulation, the homogeneous Dirichlet boundary condition on Γ_{B1}

$$\frac{1}{\mu} \nabla \cdot \boldsymbol{A} = 0 \tag{3.51}$$

has to be fulfilled in order to satisfy the Coulomb gauge in the whole region.

The interface conditions (3.7) and (3.8) have to be satisfied on Γ_{12}. Substituting Eqs. (3.4), (3.16) and (3.19) into Eqs. (3.7) and (3.8) gives

$$\boldsymbol{n}_1 \cdot \left(\nabla \times \boldsymbol{A} \right) + \boldsymbol{n}_2 \cdot \mu_2 \left(\boldsymbol{T}_0 - \nabla \Psi \right) = 0 \tag{3.52}$$

$$\boldsymbol{n}_1 \times \frac{1}{\mu_1} \nabla \times \boldsymbol{A} + \boldsymbol{n}_2 \times \left(\boldsymbol{T}_0 - \nabla \Psi \right) = \boldsymbol{0} \tag{3.53}$$

In the discretization of the equations by the finite element method, Eqs. (3.52) and (3.53) are satisfied implicitly. The differential equations (3.40), (3.48), (3.49), the interface conditions (3.52), (3.53) and the boundary conditions (3.39) on Γ_{H2}, (3.27), (3.28), (3.29), (3.41), (3.50), (3.51) are the equations applied in the $\boldsymbol{A} - V, \Psi$ formulation.

In laminated regions, the conductivity has to be explicitly set to zero in the direction normal to the laminated sheets and is represented by a tensor. For instance, by assuming the laminations to be in the *xy*-plane, the conductivity tensor can be written as

$$\underline{\sigma} = \begin{bmatrix} \sigma & 0 & 0 \\ 0 & \sigma & 0 \\ 0 & 0 & 0 \end{bmatrix} \tag{3.54}$$

where σ is the conductivity in the directions tangential to the laminated sheets.

3.6.2 $\boxed{\boldsymbol{A}-V,\Psi}$ Formulation Using Edge Basis Functions for Approximating $\boldsymbol{A}$

When the $\boldsymbol{A}-V,\Psi$ formulation is used and the vector potential $\boldsymbol{A}$ is approximated by edge basis functions, Eq. (3.47) must be solved in the conducting region. In order to ensure the uniqueness of $\boldsymbol{A}$, the tree-gauge method described in Section 3.4 is applied.

The boundary condition (3.27) is satisfied by eliminating the degrees of freedom associated with the edges of the tree and the co-tree on Γ_{B1}. Therefore, it is essential that all the co-tree edges of Γ_{B1} are closed by the tree edges also lying on Γ_{B1} [41]. In addition, the boundary conditions (3.28) and (3.50) are required.

The interface conditions (3.52) and (3.53) are also valid here, and are satisfied in accordance with the discussion presented in Section 3.6.1. In laminated regions, the electric anisotropy is represented by the diagonal tensor (3.54).

3.6.3 $\boxed{\boldsymbol{A},\Psi}$ Formulation

When the $\boldsymbol{A},\Psi$ formulation is used and the vector potential $\boldsymbol{A}$ is approximated by nodal basis functions, the differential equation

$$\nabla\times\left(\frac{1}{\mu}\nabla\times\boldsymbol{A}\right)-\nabla\left(\frac{1}{\mu}\nabla\cdot\boldsymbol{A}\right)+\sigma\frac{\partial\boldsymbol{A}}{\partial t}=\boldsymbol{0} \tag{3.55}$$

must be solved in the conducting region. In addition, the differential equation (3.40) in the non-conducting region, the interface conditions (3.52), (3.53), as well as the boundary conditions (3.39) on Γ_{H2}, (3.27), (3.28), (3.29), (3.41), (3.50), (3.51) are the equations applied in the $\boldsymbol{A},\Psi$ formulation.

On the other hand, if the vector potential $\boldsymbol{A}$ is approximated by edge basis functions, the differential equation

$$\nabla\times\left(\frac{1}{\mu}\nabla\times\boldsymbol{A}\right)+\sigma\frac{\partial\boldsymbol{A}}{\partial t}=\boldsymbol{0} \tag{3.56}$$

must be solved in the conducting region. In addition, the boundary and interface conditions presented in Section 3.6.2 are also applied here.

In laminated regions, the electric anisotropy is represented by the diagonal tensor (3.54).

3.7 Review of Earlier Work

In this section, a review of three-dimensional field calculation is presented, with special attention to the properties of various formulations and finite element types. In order to keep the presentation within reasonable limits, the weight is put on the formulations applying the finite element discretization with nodal or edge finite elements to steady-state problems.

Carpenter [36] has examined the electric and the magnetic formulations in their early stages, as well as ways of reducing the number of non-zero components of the applied vector potentials. The ambiguity of a vector potential may be removed by reducing the number of its non-zero components to two. He has also implied that the $\boldsymbol{T}-\Omega,\Omega$ formulation is more favourable than the $\boldsymbol{A}-V,\boldsymbol{A}$ formulation since a scalar potential is used in the non-conducting region rather than a vector potential.

Emson and Simkin [25] have presented the $\boldsymbol{A}$–Ω formulation which uses the modified magnetic vector potential in the conducting region and the total magnetic scalar potential in the non-conducting region. No scalar potential is needed in the conducting region. They have claimed to have found the optimal method for three-dimensional eddy-current problems as it requires a minimum set of degrees of freedom. However, their formulation assumes a constant electric conductivity. It has been shown by Morisue [24] that the electric scalar potential is necessary if the conductivity varies in the conducting region. Another disadvantage of the $\boldsymbol{A}$–Ω formulation has been pointed out by Emson et al. [46], who have found that the equations are not limited to the static case in a satisfactory way.

Biró and Preis [27] have examined the use of a penalty term in the $\boldsymbol{A}-V,\Psi$ formulation in order to satisfy the Coulomb gauge. In the case of homogeneous conductivity, they have shown that the electric scalar potential can be eliminated from the conducting region resulting in the $\boldsymbol{A},\Psi$ formulation. This formulation is correctly limited to the static case, in contrast to the $\boldsymbol{A}$–Ψ formulation.

For linear eddy-current problems, Nakata et al. [47] have compared the accuracy, computer storage and the CPU time for various formulations ($\boldsymbol{A}-V,\boldsymbol{A}$; $\boldsymbol{A}-V,\Psi$;

$\boldsymbol{A}$©Ψ; $\boldsymbol{T}-\Psi, \Psi$), where the vector potentials were approximated by nodal basis functions. They have shown that the $\boldsymbol{A}-V, \Psi$ and the $\boldsymbol{T}-\Psi, \Psi$ formulations are preferable from the viewpoint of accuracy. The $\boldsymbol{A}$©Ψ formulation is preferable from the viewpoint of computer storage and CPU time.

Albanese and Rubinacci [41] have presented a formulation based on the use of a two-component electric vector potential approximated by edge basis functions. The eliminated component of the vector potential is determined by an auxiliary vector field which does not possess closed field lines. In addition, Albanese and Rubinacci [48] have solved magnetostatic field problems in terms of the magnetic vector potential approximated by either nodal basis functions or edge basis functions. They have shown that the use of edge elements is advantageous because it results in a sparser matrix for the hexahedral elements. Thus, there is a trade-off, which happens to favour edge elements, since the amount of numerical work required to solve a linear system iteratively depends on the number of non-zero entries in the matrix.

Kameari [49] has used the $\boldsymbol{A}-V, \boldsymbol{A}$ formulation for the solution of three-dimensional eddy-current fields. The magnetic vector potential was approximated by edge basis functions, whereas V was approximated by nodal basis functions. The electric scalar potential can be replaced with the degrees of freedom of $\boldsymbol{A}$ in the tree. Having $\boldsymbol{A}$ on all the edges of the conductive region with no V corresponds to the $\boldsymbol{A}'$ formulation. The results obtained by the $\boldsymbol{A}-V, \boldsymbol{A}$ formulation with edge elements are almost equal to the results obtained by the $\boldsymbol{A}-V, \boldsymbol{A}$ formulation with nodal elements, in spite of fewer degrees of freedom. The degrees of freedom of the $\boldsymbol{A}-V, \boldsymbol{A}$ formulation with edge elements decrease to about three quarters of those of the $\boldsymbol{A}-V, \boldsymbol{A}$ formulation with nodal elements in the conductive region and are nearly equal to those of the $\boldsymbol{A}'$ formulation with nodal elements, when hexahedral elements are used.

Nakata et al. [50, 51, 52] have compared the accuracy, computer storage and the CPU time for various formulations ($\boldsymbol{A}-V, \boldsymbol{A}$ and $\boldsymbol{T}-\Psi, \Psi$) and various types of elements (first-order tetrahedral, triangular prism and brick nodal elements, as well as low-order brick edge elements). They have used a linear eddy-current problem in [50], a non-linear eddy-current problem in [51], and both a non-linear magnetostatic problem and a linear eddy-current problem in [52]. No gauge was imposed. Concerning the formulations, they have shown that the $\boldsymbol{T}-\Psi, \Psi$ formulation is favourable from the viewpoint of CPU time, and the $\boldsymbol{A}-V, \boldsymbol{A}$ formulation is favourable from the viewpoint of accuracy. In the case of the non-

linear magnetostatic problem, the most accurate results are obtained when the $\boldsymbol{A} - V, \boldsymbol{A}$ formulation with edge elements is used. In the non-linear analysis, the convergence of the Newton-Raphson iterations for the $\boldsymbol{T} - \Psi, \Psi$ formulation is not as fast as that for the $\boldsymbol{A} - V, \boldsymbol{A}$ formulation. Concerning the type of elements, they have shown that the discrepancies in the results obtained by means of the brick element are smaller than those obtained by means of the tetrahedral or triangular prism elements. The accuracy and the CPU time for the brick edge element is better than those for the brick nodal element.

Albanese and Rubinacci [53] have analyzed a three-dimensional non-linear eddy-current problem using the $\boldsymbol{A} - V, \boldsymbol{A}$ and the $\boldsymbol{T} - \Psi, \Psi$ formulations. They used edge basis functions to approximate the vector potentials and nodal basis functions for the scalar potentials. Concerning the solution of the non-linear system, they have shown that only the results obtained by the $\boldsymbol{A} - V, \boldsymbol{A}$ formulation using a fine mesh are in good agreement with the experimental results. They have found that the choice of the tree does not affect the solution of the problem in terms of fields and currents. This means that the different solutions obtained with different trees are clearly different in terms of $\boldsymbol{A}$ and $\boldsymbol{T}$ but provide the same $\boldsymbol{H}$, $\boldsymbol{B}$, $\boldsymbol{J}$ and $\boldsymbol{E}$. However, the choice of the tree does affect the properties of the systems of equations and, thereby, the convergence of the iterative process — an iterative solver is necessary to solve very large systems of equations corresponding to three-dimensional eddy-current problems. Similarly, Golias and Tsiboukis [54] have shown that the numerical accuracy, as well as the rate of convergence of the iterative process depend on the choice of the tree. They have solved a magnetostatic problem and have used the edge basis functions to approximate the magnetic vector potential.

Furthermore, Albanese and Rubinacci [55] have applied the $\boldsymbol{A} - V, \boldsymbol{A}$ and the $\boldsymbol{T} - \Psi, \Psi$ formulations to magnetostatic and eddy-current problems. The vector potentials were approximated by edge basis functions. They have investigated the effects of the choice of formulation, the choice of additional constraints, as well as cancellation and interface problems. The tree gauge applied to edge elements allows for a dramatic reduction of the computational effort necessary to achieve a given degree of accuracy. This reduction is due to a smaller number of unknown variables, mainly caused by forcing one component of the vector potential to zero, and due to a sparser coefficient matrix. Cancellation and interface problems are overcome when edge elements are used. Concerning the choice of formulations, they have found that neither the $\boldsymbol{A} - V, \boldsymbol{A}$ nor the $\boldsymbol{T} - \Psi, \Psi$ formulation is the

most favourable for a general problem and that the choice of the formulation might be made according to the particular problem.

Biro et al. [56] have applied the $\boldsymbol{A},\boldsymbol{A}$ formulation to a magnetostatic problem defined in [57] and consisting of highly permeable iron parts. The system of equations obtained was solved by the conjugate gradient method with incomplete Cholesky preconditioning.They have shown that the formulation without gauging and with nodal elements gives results very close to the measured values, but the convergence of the iterative process is catastrophic. The formulation with nodal elements and the Coulomb gauge gives a good convergence, but has difficulty in satisfying the interface conditions, which leads to inaccurate results. This difficulty can be eliminated by allowing the normal component of the vector potential to be discontinuous at these interfaces. The formulation with edge elements and the tree gauge yields a poor convergence when an arbitrary tree is used. The formulation without gauging and with edge elements gives results very close to the measured values and a good convergence.

If gauging is abandoned when edge elements are used, a singular matrix is obtained in the course of the numerical solution. The conjugate gradient method is capable of solving such a system [7], and a gauge condition is not necessary in a vector potential formulation to get a good solution of the system. A singular system can only be solved if the right-hand side is consistent, as shown by Fujiwara et al. [58] and Ren [59]. The consistence of the right-hand side is equivalent to the current density being exactly divergence free. They have shown that this requirement can be fulfilled by expressing the current density by the curl of a vector potential approximated by edge basis functions, and by projecting this vector potential on the curl of the space W^1 of the edge basis functions.

Fujiwara [60] has investigated the effect of V in the $\boldsymbol{A}-V,\boldsymbol{A}$ formulation on the convergence characteristic of the Incomplete Cholesky Conjugate Gradient (ICCG) method using edge elements. He has shown that the convergence is fairly improved by adding the electric scalar potential V. Even in the case when the $\boldsymbol{A},\boldsymbol{A}$ formulation fails to converge, the $\boldsymbol{A}-V,\boldsymbol{A}$ formulation can give a convergent solution. However, the memory requirement is increased if V is taken into account.

Dular et al. [61, 62] have presented finite element spaces built on tetrahedra, hexahedra and prisms. They have solved three-dimensional eddy-current problems by means of a formulation based on the modified magnetic vector potential

approximated by edge basis functions. Hexahedra give better results than prisms and tetrahedra for equivalent meshes. In order to increase accuracy, higher-order elements are to be developed.

Touma Holmberg and Luomi [110] have compared the $\boldsymbol{T} - \Psi, \Psi$ and the $\boldsymbol{A} - V, \Psi$ formulations, as well as nodal and edge finite elements in the solution of three-dimensional eddy-current problems. The methods were compared using the Asymmetrical Conductor with a Hole problem, which is benchmark problem 7, and a model of the end region of a 120 MVA hydrogenerator. The examples have shown a good correspondence between the results obtained by different methods, and have indicated that edge elements are computationally more efficient than nodal elements.

The nodal elements do not allow for the direct evaluation of discontinuous fields. Therefore, potentials describing the fields are used instead of the field vectors, which are obtained by differentiation from the potentials. The normal components of the magnetic field intensity $\boldsymbol{H}$ and the electric field intensity $\boldsymbol{E}$ are discontinuous on surfaces where there is an abrupt change in permeability and conductivity, respectively. Since the edge elements allow the normal component of a vector function to jump across the interface of two materials with different properties, the edge elements allow for the direct computation of the field of interest, be it the magnetic field $\boldsymbol{H}$ or the electric field $\boldsymbol{E}$ [63]. The edge elements do not impose more continuity on $\boldsymbol{H}$ or $\boldsymbol{E}$ than physics requires.

In the $\boldsymbol{T} - \Psi, \Psi$ formulation where $\boldsymbol{T}$ is approximated by edge basis functions, the magnetic field is solved by means of the nodal Ψ and the line integrals of $\boldsymbol{T}$ along the co-tree edges in the conductive region. The nodal Ψ can be replaced with the degrees of freedom of $\boldsymbol{T}$ in the tree. Having $\boldsymbol{T}$ on all the edges with no Ψ in the conductive region corresponds to the $\boldsymbol{H}, \Psi$ formulation. The degrees of freedom in the $\boldsymbol{T} - \Psi, \Psi$ and the $\boldsymbol{H}, \Psi$ formulations are the same. In addition, Webb and Forghani [64] have shown that the $\boldsymbol{T} - \Psi, \Psi$ and the $\boldsymbol{H}, \Psi$ formulations approximate the magnetic field in the same way and provide identical answers. However, these methods are not equally efficient. The $\boldsymbol{H}, \Psi$ formulation is unstable at low frequencies and should be avoided. The matrix equation obtained from the $\boldsymbol{T} - \Psi, \Psi$ formulation is better conditioned at low frequencies and can be solved more efficiently. The $\boldsymbol{T} - \Psi, \Psi$ formulation converges well down to DC.

Bossavit and Vérité [65, 66, 67, 68, 69] and Onuki et al. [70] have reported on a mixed finite element and boundary element method to solve three-dimensional

eddy-current problems with open boundaries. The $\boldsymbol{H}, \Psi$ formulation where $\boldsymbol{H}$ is approximated by edge basis functions is used. The conducting region is discretized by the finite element method adopting $\boldsymbol{H}$, whereas the non-conducting region is discretized by the boundary element method adopting Ψ. In addition, Onuki et al. [70] have proposed a new boundary element discretization in the $\boldsymbol{H}, \Psi$ formulation, which makes it easy to couple the boundary element region with the finite element region by introducing the edge boundary element.

Similarly, Wakao and Onuki [71] have presented a mixed finite element and boundary element method adopting the modified magnetic vector potential $\boldsymbol{A}'$ and the magnetic field intensity $\boldsymbol{H}$ as the physical quantities. The conducting region is discretized by the finite element method adopting $\boldsymbol{A}'$ and the non-conducting region by the boundary element method adopting $\boldsymbol{H}$. Both $\boldsymbol{A}'$ and $\boldsymbol{H}$ are approximated by edge basis functions.

Various formulations and finite elements have been investigated. It is, however, important to compare different techniques and to apply them to problems in electrical machinery. This work investigates the $\boldsymbol{T}-\Psi, \Psi$, the $\boldsymbol{T}-\Omega, \Omega$, the $\boldsymbol{A}-V, \Psi$ and the $\boldsymbol{A}, \Psi$ formulations in association with nodal and edge finite elements.

3.8 Discretization of the Equations

There are several possibilities for forming finite element equations. In the method of weighted residuals, the differential equations associated with the problem are multiplied with suitable weight functions and integrated over the solution region. In the Galerkin form of the weighted residual method, the nodal or the edge shape functions are selected as weight functions. In this work, the derivation of the finite element equations is based on the Galerkin method. For the sake of brevity, the discretization of the $\boldsymbol{T}-\Psi, \Psi$ and the $\boldsymbol{A}-V, \Psi$ equations is presented.

3.8.1 Discretization of the $\boldsymbol{T}-\Psi, \Psi$ Equations Using Nodal Basis Functions for Approximating $\boldsymbol{T}$

In this section, the equations of the $\boldsymbol{T}-\Psi, \Psi$ formulation are discretized in the case where the vector potential $\boldsymbol{T}$ is approximated by nodal basis functions. The vector field $\boldsymbol{T}_0$ and the potential Ψ are also approximated by nodal basis functions. The approximations of $\boldsymbol{T}$, $\boldsymbol{T}_0$ and Ψ are

$$\boldsymbol{T} = \boldsymbol{x}\sum_{i=1}^{n_c} N_i T_{xi} + \boldsymbol{y}\sum_{i=1}^{n_c} N_i T_{yi} + \boldsymbol{z}\sum_{i=1}^{n_c} N_i T_{zi} \tag{3.57}$$

$$\boldsymbol{T}_0 = \boldsymbol{x}\sum_{i=1}^{n_n} N_i T_{0xi} + \boldsymbol{y}\sum_{i=1}^{n_n} N_i T_{0yi} + \boldsymbol{z}\sum_{i=1}^{n_n} N_i T_{0zi} \tag{3.58}$$

$$\Psi = \sum_{i=1}^{n_n} N_i \Psi_i \tag{3.59}$$

where $\boldsymbol{x}, \boldsymbol{y}, \boldsymbol{z}$ are the unit vectors in the Cartesian coordinate system, T_{xi}, T_{yi}, T_{zi}, T_{0xi}, T_{0yi} and T_{0zi} are the Cartesian components of the respective vector quantities at node i, Ψ_i is the value of Ψ at node i, N_i is the nodal shape function associated with node i, n_c is the number of nodes in the conducting region and n_n is the total number of nodes in the finite element mesh. The summations in Eq. (3.57) are made over n_c since $\boldsymbol{T}$ exists in the conducting region. The summations in Eqs. (3.58) and (3.59) are made over n_n since $\boldsymbol{T}_0$ and Ψ exist in the whole problem region.

The dimension of the system matrices is considerable, even if the geometry of a three-dimensional problem would be relatively simple. In addition, even if the system matrices are sparse, the number of non-zero matrix elements is large. Therefore, it is desirable that the system matrices are symmetric. In order to obtain symmetric system matrices, the Galerkin method is applied to the time derivatives of the differential equations (3.35) and (3.40) instead of the equations themselves. The Galerkin form of Eqs. (3.34), (3.35) and (3.40) associated with node i is

$$\int_{\Omega_1} \boldsymbol{N}_i \left\{ \nabla \times \left(\frac{1}{\sigma} \nabla \times \boldsymbol{T} \right) - \nabla \left(\frac{1}{\sigma} \nabla \cdot \boldsymbol{T} \right) + \mu \left(\frac{\partial \boldsymbol{T}_0}{\partial t} + \frac{\partial \boldsymbol{T}}{\partial t} - \nabla \frac{\partial \Psi}{\partial t} \right) \right\} \mathrm{d}\Omega = 0 \tag{3.60}$$

$$\int_{\Omega_1} N_i \left\{ \nabla \cdot \mu \left(\frac{\partial \boldsymbol{T}_0}{\partial t} + \frac{\partial \boldsymbol{T}}{\partial t} - \nabla \frac{\partial \Psi}{\partial t} \right) \right\} \mathrm{d}\Omega = 0 \tag{3.61}$$

$$\int_{\Omega_2} N_i \left\{ \nabla \cdot \mu \left(\frac{\partial \boldsymbol{T}_0}{\partial t} - \nabla \frac{\partial \Psi}{\partial t} \right) \right\} \mathrm{d}\Omega = 0 \tag{3.62}$$

where the scalar weight function N_i is the nodal shape function, and the vector weight function $\boldsymbol{N}_i$ is defined by

$$\boldsymbol{N}_i = N_i\,\boldsymbol{x} + N_i\,\boldsymbol{y} + N_i\,\boldsymbol{z} \tag{3.63}$$

Applying vector identities, Gauss's theorem, as well as the boundary and interface conditions (3.36), (3.37), (3.41) and (3.43), Eqs. (3.60) to (3.62) can be written as

$$\int_{\Omega_1} \left[\frac{1}{\sigma} \left(\nabla \times \boldsymbol{N}_i\right) \cdot \left(\nabla \times \boldsymbol{T}\right) + \frac{1}{\sigma} \left(\nabla \cdot \boldsymbol{N}_i\right) \left(\nabla \cdot \boldsymbol{T}\right) + \mu\, \boldsymbol{N}_i \cdot \left(\frac{\partial \boldsymbol{T}}{\partial t} - \nabla \frac{\partial \Psi}{\partial t} \right) \right] \mathrm{d}\Omega$$

$$= - \int_{\Omega_1} \mu\, \boldsymbol{N}_i \cdot \frac{\partial \boldsymbol{T}_0}{\partial t}\, \mathrm{d}\Omega \tag{3.64}$$

$$\int_{\Omega_1} \mu \left(- \nabla N_i \cdot \frac{\partial \boldsymbol{T}}{\partial t} + \nabla N_i \cdot \nabla \frac{\partial \Psi}{\partial t} \right) \mathrm{d}\Omega = \int_{\Omega_1} \mu\, \nabla N_i \cdot \frac{\partial \boldsymbol{T}_0}{\partial t}\, \mathrm{d}\Omega \tag{3.65}$$

$$\int_{\Omega_2} \mu\, \nabla N_i \cdot \nabla \frac{\partial \Psi}{\partial t}\, \mathrm{d}\Omega = \int_{\Omega_2} \mu\, \nabla N_i \cdot \frac{\partial \boldsymbol{T}_0}{\partial t}\, \mathrm{d}\Omega \tag{3.66}$$

where the terms of $\boldsymbol{T}_0$ have been moved to the right of the equations. Equations (3.26) and (3.39) are the conditions that are not satisfied by Eqs. (3.64) to (3.66), and must be fulfilled explicitly.

If the terms multiplying the potentials are collected in a matrix $\boldsymbol{S}$ and the terms multiplying the time derivatives of the potentials are collected in a matrix $\boldsymbol{U}$, Eqs. (3.64) to (3.66) can be written as

$$\boldsymbol{S}\,\boldsymbol{a} + \boldsymbol{U} \frac{\mathrm{d}\boldsymbol{a}}{\mathrm{d}\boldsymbol{t}} = \boldsymbol{f} \tag{3.67}$$

where the column vector $\boldsymbol{a}$ contains the nodal values of the potentials and the right-hand side of the equations forms the source vector $\boldsymbol{f}$. Since the potentials are assumed to vary sinusoidally with time, they can be represented by phasors. The matrix equation is, thus,

$$\boldsymbol{S}\underline{\boldsymbol{a}} + \mathrm{j}\omega \boldsymbol{U}\underline{\boldsymbol{a}} = \underline{\boldsymbol{f}} \tag{3.68}$$

where ω is the angular frequency of the source current. The variables are complex variables that can be divided into real and imaginary parts

$$\begin{aligned} \underline{\boldsymbol{a}} &= \boldsymbol{a}_{\mathrm{re}} + \mathrm{j}\boldsymbol{a}_{\mathrm{im}} \\ \underline{\boldsymbol{T}}_0 &= \boldsymbol{T}_{0\mathrm{re}} + \mathrm{j}\boldsymbol{T}_{0\mathrm{im}} \end{aligned} \tag{3.69}$$

which leads to the matrix equation

$$\begin{bmatrix} \boldsymbol{S} & -\omega\boldsymbol{U} \\ \omega\boldsymbol{U} & \boldsymbol{S} \end{bmatrix} \begin{bmatrix} \boldsymbol{a}_{\mathrm{re}} \\ \boldsymbol{a}_{\mathrm{im}} \end{bmatrix} = \begin{bmatrix} \boldsymbol{f}_{\mathrm{re}} \\ \boldsymbol{f}_{\mathrm{im}} \end{bmatrix} \tag{3.70}$$

Eq. (3.70) can be written as

$$\boldsymbol{S}_1 \boldsymbol{a}_1 = \boldsymbol{f}_1 \tag{3.71}$$

where $\boldsymbol{S}_1$ is the first matrix in the left-hand side of Eq. (3.70), and the column vectors $\boldsymbol{a}_1$ and $\boldsymbol{f}_1$ contain the real and imaginary parts of $\underline{\boldsymbol{a}}$ and $\underline{\boldsymbol{f}}$, respectively. In addition to the symmetry, the system matrices of the $\boldsymbol{T}-\Psi,\Psi$ formulation are diagonally dominant [72], i.e.,

$$|d_{ii}| > \sum_{\substack{j=1 \\ j \neq i}}^{c} |d_{ij}| \qquad i = 1, \ldots, c \tag{3.72}$$

where d_{ii} is a diagonal matrix element at row i, d_{ij} is a matrix element at row i and column j and c is the total number of rows or columns.

3.8.2 Discretization of the $\boldsymbol{T}-\Psi,\Psi$ Equations Using Edge Basis Functions for Approximating $\boldsymbol{T}$

In this section, the equations of the $\boldsymbol{T}-\Psi,\Psi$ formulation are discretized in the case where the vector potential $\boldsymbol{T}$ is approximated by edge basis functions. The vector field $\boldsymbol{T}_0$ is also approximated by edge basis functions. On the other hand, the approximation of Ψ is expressed by nodal basis elements, and given by Eq. (3.59). The approximations of $\boldsymbol{T}$ and $\boldsymbol{T}_0$ are

$$\boldsymbol{T} = \sum_{i=1}^{n_{ec}} \boldsymbol{N}_{ei}\, T_{ti} \tag{3.73}$$

$$\boldsymbol{T}_0 = \sum_{i=1}^{n_e} \boldsymbol{N}_{ei}\, T_{0ti} \tag{3.74}$$

where $\boldsymbol{N}_{ei}$ is the edge shape function associated with edge i, n_e is the total number of edges in the finite element mesh, n_{ec} is the number of edges in the conducting region, and T_{0ti} and T_{ti} are the line integrals of $\boldsymbol{T}_0$ and $\boldsymbol{T}$ along edge i, respectively. The summation in Eq. (3.73) is made over n_{ec} because $\boldsymbol{T}$ is restricted to the conducting region. On the other hand, the summation in Eq. (3.74) is made over n_e since $\boldsymbol{T}_0$ exists in the whole problem region. The edge shape function $\boldsymbol{N}_{ei}$ is expressed as

$$\boldsymbol{N}_{ei} = \begin{bmatrix} N_{eix} \\ N_{eiy} \\ N_{eiz} \end{bmatrix} \tag{3.75}$$

The curl of $\boldsymbol{T}$ is a linear combination of the curls of the edge shape functions $\boldsymbol{N}_{ei}$

$$\nabla \times \boldsymbol{T} = \sum_{i=1}^{n_{ec}} \left(\nabla \times \boldsymbol{N}_{ei}\right) T_{ti} \tag{3.76}$$

where $\nabla \times \boldsymbol{N}_{ei}$ is, in its turn, a matrix given by

$$\nabla \times \boldsymbol{N}_{ei} = \begin{bmatrix} \left(\nabla \times \boldsymbol{N}_{ei}\right)_x \\ \left(\nabla \times \boldsymbol{N}_{ei}\right)_y \\ \left(\nabla \times \boldsymbol{N}_{ei}\right)_z \end{bmatrix} = \begin{bmatrix} \dfrac{\partial N_{eiz}}{\partial y} - \dfrac{\partial N_{eiy}}{\partial z} \\ \dfrac{\partial N_{eix}}{\partial z} - \dfrac{\partial N_{eiz}}{\partial x} \\ \dfrac{\partial N_{eiy}}{\partial x} - \dfrac{\partial N_{eix}}{\partial y} \end{bmatrix} \tag{3.77}$$

In addition, the gradient of Ψ is a linear combination of the gradients of the nodal shape functions N_i

$$\nabla \Psi = \sum_{i=1}^{n_n} \left(\nabla N_i\right) \Psi_i \tag{3.78}$$

where ∇N_i is a matrix given by

$$\nabla N_i = \begin{bmatrix} \dfrac{\partial N_i}{\partial x} \\ \dfrac{\partial N_i}{\partial y} \\ \dfrac{\partial N_i}{\partial z} \end{bmatrix} \tag{3.79}$$

The Galerkin form of Eq. (3.33) with the weight functions being the edge shape function associated with edge i and the gradient of the nodal shape function associated with node j results in

$$\int_{\Omega_1} \boldsymbol{N}_{ei} \cdot \left\{ \nabla \times \left(\frac{1}{\sigma} \nabla \times \boldsymbol{T} \right) + \mu \left(\frac{\partial \boldsymbol{T}_0}{\partial t} + \frac{\partial \boldsymbol{T}}{\partial t} - \nabla \frac{\partial \Psi}{\partial t} \right) \right\} \mathrm{d}\Omega = 0 \tag{3.80}$$

$$\int_{\Omega_1} \nabla N_j \cdot \left\{ \nabla \times \left(\frac{1}{\sigma} \nabla \times \boldsymbol{T} \right) + \mu \left(\frac{\partial \boldsymbol{T}_0}{\partial t} + \frac{\partial \boldsymbol{T}}{\partial t} - \nabla \frac{\partial \Psi}{\partial t} \right) \right\} \mathrm{d}\Omega = 0 \tag{3.81}$$

respectively. Similarly, the Galerkin form of Eq. (3.40) with the weight function being the nodal shape function associated with node j is written as

$$\int_{\Omega_2} N_j \left\{ \nabla \cdot \mu \left(\frac{\partial \boldsymbol{T}_0}{\partial t} - \nabla \frac{\partial \Psi}{\partial t} \right) \right\} \mathrm{d}\Omega = 0 \tag{3.82}$$

Applying vector identities, the divergence theorem, as well as the boundary and interface conditions (3.36), (3.41) and (3.43), Eqs. (3.80) to (3.82) can be written as

$$\begin{aligned} &\int_{\Omega_1} \left(\nabla \times \boldsymbol{N}_{ei} \right) \cdot \left(\frac{1}{\sigma} \nabla \times \boldsymbol{T} \right) \mathrm{d}\Omega + \int_{\Omega_1} \boldsymbol{N}_{ei} \cdot \mu \left(\frac{\partial \boldsymbol{T}}{\partial t} - \nabla \frac{\partial \Psi}{\partial t} \right) \mathrm{d}\Omega = \\ &\qquad = - \int_{\Omega_1} \boldsymbol{N}_{ei} \cdot \mu \frac{\partial \boldsymbol{T}_0}{\partial t} \mathrm{d}\Omega \end{aligned} \tag{3.83}$$

$$- \int_{\Omega_1} \mu \, \nabla N_j \cdot \frac{\partial \boldsymbol{T}}{\partial t} \mathrm{d}\Omega + \int_{\Omega_1} \mu \, \nabla N_j \cdot \nabla \frac{\partial \Psi}{\partial t} \mathrm{d}\Omega = \int_{\Omega_1} \mu \, \nabla N_j \cdot \frac{\partial \boldsymbol{T}_0}{\partial t} \mathrm{d}\Omega \tag{3.84}$$

$$\int_{\Omega_2} \mu \, \nabla N_j \cdot \nabla \frac{\partial \Psi}{\partial t} \mathrm{d}\Omega = \int_{\Omega_2} \mu \, \nabla N_j \cdot \frac{\partial \boldsymbol{T}_0}{\partial t} \mathrm{d}\Omega \tag{3.85}$$

where the terms of $\boldsymbol{T}_0$ have been moved to the right of the equations. Equations (3.26) and (3.39) are the conditions that are not satisfied by Eqs. (3.83) to (3.85), and must be fulfilled explicitly.

When the terms multiplying the potentials are collected in a matrix $\boldsymbol{S}$ and the terms multiplying the time derivatives of the potentials are collected in a matrix $\boldsymbol{U}$, Eqs. (3.83) to (3.85) can be written as Eq. (3.68). The column vector $\boldsymbol{a}$ in Eq. (3.68) contains the line integrals of $\boldsymbol{T}$ along the edges in the conducting region and the nodal values of Ψ in the whole region.

3.8.3 Discretization of the $\boldsymbol{A} - V, \Psi$ Equations Using Nodal Basis Functions for Approximating $\boldsymbol{A}$

In this section, the equations of the $\boldsymbol{A} - V, \Psi$ formulation are discretized in the case where the vector potential $\boldsymbol{A}$ is approximated by nodal basis functions. The vector field $\boldsymbol{T}_0$ and the potentials V and Ψ are also approximated by nodal basis functions. The approximations of $\boldsymbol{A}$, $\boldsymbol{T}_0$, V and Ψ are

$$\boldsymbol{A} = \boldsymbol{x}\sum_{i=1}^{n_c} N_i A_{xi} + \boldsymbol{y}\sum_{i=1}^{n_c} N_i A_{yi} + \boldsymbol{z}\sum_{i=1}^{n_c} N_i A_{zi} \tag{3.86}$$

$$\boldsymbol{T}_0 = \boldsymbol{x}\sum_{i=1}^{n_{nc}} N_i T_{0xi} + \boldsymbol{y}\sum_{i=1}^{n_{nc}} N_i T_{0yi} + \boldsymbol{z}\sum_{i=1}^{n_{nc}} N_i T_{0zi} \tag{3.87}$$

$$V = \sum_{i=1}^{n_c} N_i V_i \tag{3.88}$$

$$\Psi = \sum_{i=1}^{n_{nc}} N_i \Psi_i \tag{3.89}$$

where A_{xi}, A_{yi} and A_{zi} are the Cartesian components of $\boldsymbol{A}$ at node i, V_i is the value of V at node i and n_{nc} is the number of nodes in the non-conducting region. The summations in Eqs. (3.86) and (3.88) are made over n_c since $\boldsymbol{A}$ and V exist in the conducting region. The summations in Eqs. (3.87) and (3.89) are made over n_{nc} since $\boldsymbol{T}_0$ and Ψ are defined in the non-conducting region.

In order to obtain symmetric system matrices, V is defined by means of a new scalar function ν as

$$V = \frac{\partial \nu}{\partial t} \tag{3.90}$$

By taking into account Eq. (3.90), the Galerkin form of the partial differential equations (3.40), (3.48) and (3.49) associated with node i is

$$\int_{\Omega_1} \boldsymbol{N}_i \left\{ \nabla \times \frac{1}{\mu} \nabla \times \boldsymbol{A} + \sigma \frac{\partial \boldsymbol{A}}{\partial t} + \sigma \nabla \frac{\partial \nu}{\partial t} \right\} \mathrm{d}\Omega = 0 \tag{3.91}$$

$$\int_{\Omega_1} N_i \left\{ \nabla \cdot \left(\pm \sigma \frac{\partial \boldsymbol{A}}{\partial t} \pm \sigma \nabla \frac{\partial \nu}{\partial t} \right) \right\} \mathrm{d}\Omega = 0 \tag{3.92}$$

$$\int_{\Omega_2} N_i \left\{ \nabla \cdot \mu \left(\boldsymbol{T}_0 - \nabla \Psi \right) \right\} \mathrm{d}\Omega = 0 \tag{3.93}$$

Applying vector identities, Gauss's theorem, as well as the boundary and interface conditions (3.28), (3.41), (3.50), (3.51), (3.52) and (3.53), Eqs. (3.91) to (3.93) can be written as

$$\begin{aligned} \int_{\Omega_1} \left[\frac{1}{\mu} \left(\nabla \times \boldsymbol{N}_i \right) \cdot \left(\nabla \times \boldsymbol{A} \right) + \frac{1}{\mu} \left(\nabla \cdot \boldsymbol{N}_i \right) \left(\nabla \cdot \boldsymbol{A} \right) + \sigma \boldsymbol{N}_i \cdot \frac{\partial \boldsymbol{A}}{\partial t} + \sigma \boldsymbol{N}_i \cdot \nabla \frac{\partial \nu}{\partial t} \mathrm{d}\Omega \right] \\ + \int_{\Gamma_{12}} \boldsymbol{N}_i \cdot \left(\nabla \Psi \times \boldsymbol{n}_1 \right) \mathrm{d}\Gamma = \int_{\Gamma_{12}} \boldsymbol{N}_i \cdot \left(\boldsymbol{T}_0 \times \boldsymbol{n}_1 \right) \mathrm{d}\Gamma \end{aligned} \tag{3.94}$$

$$\int_{\Omega_1} \left(\sigma \nabla N_i \cdot \frac{\partial \boldsymbol{A}}{\partial t} + \sigma \nabla N_i \cdot \nabla \frac{\partial \nu}{\partial t} \right) \mathrm{d}\Omega = 0 \tag{3.95}$$

$$\int_{\Omega_2} \mu \nabla N_i \cdot \nabla \Psi \ \mathrm{d}\Omega - \int_{\Gamma_{12}} N_i \left(\nabla \times \boldsymbol{A} \right) \cdot \boldsymbol{n}_1 \ \mathrm{d}\Gamma = \int_{\Omega_2} \mu \nabla N_i \cdot \boldsymbol{T}_0 \ \mathrm{d}\Omega \tag{3.96}$$

where the terms of $\boldsymbol{T}_0$ have been moved to the right of the equations. Equations (3.27), (3.29) and (3.39) are the conditions that are not satisfied by Eqs. (3.94) to (3.96), and must be fulfilled explicitly. Similar to the $\boldsymbol{T}-\Psi, \Psi$ formulation, Eqs. (3.94) to (3.96) can be written in the form of Eq. (3.68). Furthermore, the system matrix $\boldsymbol{S}$ is not diagonally dominant due to the surface integral term in Eq. (3.96) [72].

3.8.4 Discretization of the $\boxed{A - V, \Psi}$ Equations Using Edge Basis Functions for Approximating A

In this section, the equations of the $\boldsymbol{A} - V, \Psi$ formulation are discretized in the case where the vector potential $\boldsymbol{A}$ is approximated by edge basis functions. The vector field $\boldsymbol{T}_0$ is also approximated by edge basis functions. On the other hand, the approximations of V and Ψ are expressed by nodal basis elements, and given by Eqs. (3.88) and (3.89), respectively. The approximations of $\boldsymbol{A}$ and $\boldsymbol{T}_0$ are

$$\boldsymbol{A} = \sum_{i=1}^{n_{ec}} \boldsymbol{N}_{ei} \, A_{ti} \tag{3.97}$$

$$\boldsymbol{T}_0 = \sum_{i=1}^{n_{enc}} \boldsymbol{N}_{ei} \, T_{0ti} \tag{3.98}$$

where A_{ti} is the line integral of $\boldsymbol{A}$ along edge i, and n_{enc} is the number of edges in the non-conducting region. The summation in Eq. (3.97) is made over n_{ec} since $\boldsymbol{A}$ exists in the conducting region. The summation in Eq. (3.98) is made over n_{enc} since $\boldsymbol{T}_0$ is defined in the non-conducting region.

By taking into account Eq. (3.90), the Galerkin form of Eq. (3.47) with the weight functions being the edge shape function associated with edge i and the gradient of the nodal shape function associated with node j results in

$$\int_{\Omega_1} \boldsymbol{N}_{ei} \cdot \left\{ \nabla \times \frac{1}{\mu} \nabla \times \boldsymbol{A} + \sigma \frac{\partial \boldsymbol{A}}{\partial t} + \sigma \nabla \frac{\partial \nu}{\partial t} \right\} \mathrm{d}\Omega = 0 \tag{3.99}$$

$$\int_{\Omega_1} \nabla N_j \cdot \left\{ \nabla \times \frac{1}{\mu} \nabla \times \boldsymbol{A} + \sigma \frac{\partial \boldsymbol{A}}{\partial t} + \sigma \nabla \frac{\partial \nu}{\partial t} \right\} \mathrm{d}\Omega = 0 \tag{3.100}$$

respectively. Similarly, the Galerkin form of Eq. (3.40) with the weight function being the nodal shape function associated with node j is written as

$$\int_{\Omega_2} N_j \left\{ \nabla \cdot \mu \left(\boldsymbol{T}_0 - \nabla \Psi \right) \right\} \mathrm{d}\Omega = 0 \tag{3.101}$$

Applying vector identities, the divergence theorem, as well as the boundary and interface conditions (3.28), (3.41), (3.50), (3.52) and (3.53), the Galerkin form of Eqs. (3.99) to (3.101) can be rewritten as

$$\int_{\Omega_1}\left[\frac{1}{\mu}\left(\nabla\times\boldsymbol{N}_{ei}\right)\cdot\left(\nabla\times\boldsymbol{A}\right)+\sigma\,\boldsymbol{N}_{ei}\cdot\frac{\partial\boldsymbol{A}}{\partial t}+\sigma\,\boldsymbol{N}_{ei}\cdot\nabla\frac{\partial\nu}{\partial t}\,\mathrm{d}\Omega\right] + \int_{\Gamma_{12}}\boldsymbol{N}_{ei}\cdot\left(\nabla\Psi\times\boldsymbol{n}_1\right)\mathrm{d}\Gamma=\int_{\Gamma_{12}}\boldsymbol{N}_{ei}\cdot\left(\boldsymbol{T}_0\times\boldsymbol{n}_1\right)\mathrm{d}\Gamma \tag{3.102}$$

$$\int_{\Omega_1}\sigma\left(\nabla N_j\cdot\frac{\partial\boldsymbol{A}}{\partial t}+\nabla N_j\cdot\nabla\frac{\partial\nu}{\partial t}\right)\mathrm{d}\Omega=0 \tag{3.103}$$

$$\int_{\Omega_2}\mu\,\nabla N_j\cdot\nabla\Psi\;\mathrm{d}\Omega\;-\int_{\Gamma_{12}}N_j\left(\nabla\times\boldsymbol{A}\right)\cdot\boldsymbol{n}_1\;\mathrm{d}\Gamma\;=\int_{\Omega_2}\mu\,\nabla N_j\cdot\boldsymbol{T}_0\;\mathrm{d}\Omega \tag{3.104}$$

where the source terms have been moved to the right-hand side of the equations. Equations (3.27) and (3.39) are the conditions that are not satisfied by Eqs. (3.102) to (3.104), and must be fulfilled explicitly. Similar to the $\boldsymbol{T}-\Psi,\Psi$ formulation, Eqs. (3.102) to (3.104) can be written in the form of Eq. (3.68). The column vector $\boldsymbol{a}$ in Eq. (3.68) contains the line integrals of $\boldsymbol{A}$ along the edges in the conducting region, the nodal values of V in the conducting region, and the nodal values of Ψ in the non-conducting region.

3.9 Iterative Solution of the Equation System

In order to solve very large systems of equations corresponding to three-dimensional eddy-current problems, it is necessary to use an iterative solver. The Preconditioned Conjugate Gradient Square (PCG_S) method, which has been developed by Kristensen [73] and Korneliussen [74], is used in this work. PCG_S uses the direct solver SESYS developed by Houbak [75] as an incomplete Cholesky preconditioner. PCG_S solves unsymmetric systems of linear equations.

The total number of iterations required in iterative solution methods depends on the accuracy desired from the solution. The iterations are stopped when the convergence criteria

$$\begin{aligned} \left| \boldsymbol{f}_1 \pm \boldsymbol{S}_1 \boldsymbol{a}_1 \right|_\infty &< \varepsilon \\ \left| \boldsymbol{f}_1 \pm \boldsymbol{S}_1 \boldsymbol{a}_1 \right|_2 &< \varepsilon \end{aligned} \tag{3.105}$$

are satisfied simultaneously, where ε is the error tolerance. In all computations presented in Chapter 5, ε is set equal to 10^{-4}.

4 Computation of the Source Field

In order to obtain a small number of unknowns, it is reasonable to use a magnetic scalar potential in non-conducting regions. In electrical machine problems, the shape of the end windings is complicated and it is important that the coils themselves are not modeled by the finite element mesh. Therefore, the regions with known source current densities should also be modeled using a magnetic scalar potential and, thus, included in the non-conducting regions.

In the non-conducting regions, the rotational part of the magnetic field produced by the given source current distribution must be modeled by the source field $\boldsymbol{T}_0$. This chapter gives an overall review of the different methods used for calculating $\boldsymbol{T}_0$. The method based on replacing volume distributions of current by equivalent distributions of fictitious magnetization, volume charges, as well as surface currents and charges, is given and described in detail.

4.1 Windings of a Turbogenerator

This section illustrates the geometry of the windingsof an electrical machine. As an example, a 635 MVA two-pole turbogenerator is considered.

StatorWinding

The stator winding is a double-layer diamond winding with 30 stator slots. The slot angle is 12 °, and the number of slots per pole and phase is 5. The coils are short-pitched, and the coil span is 4/5 of the pole pitch.

Each coil of the stator windingconsists of a curved end part and a straight slot part known as the coil side. Two coil sides are fitted in each slot since the windingis a double-layer winding. Figure 4.1 describes the different sections of the curved end part of a typical coil. A coil has a short straight section as it emerges from the slot, followed by a radial bend in the same plane called the "knuckle". The knuckle is, in turn, followed by a peripheral bend or an involute laid upon the surface of a fictitious cone of angle τ. The coil ends as an axial straight section called the "nose". The nose joins the halves of the stator coil. The bottom half-coil has the same features as the top half-coil, but the dimensions are different and the peripheral bend is in the opposite direction. Since all the stator coils are identical, only one coil is geometrically modeled and the remaining coils are obtained by rotating the

geometrically modeled coil by a multiple of the slot angle. Figure 4.2 illustrates the end parts of a stator coil, whereas Fig. 4.3 shows the overall configuration of the end parts of the stator winding. For practical purposes, the stator winding was parameterized by Torsein and the author [76] for an automatic generation of windingmodels.

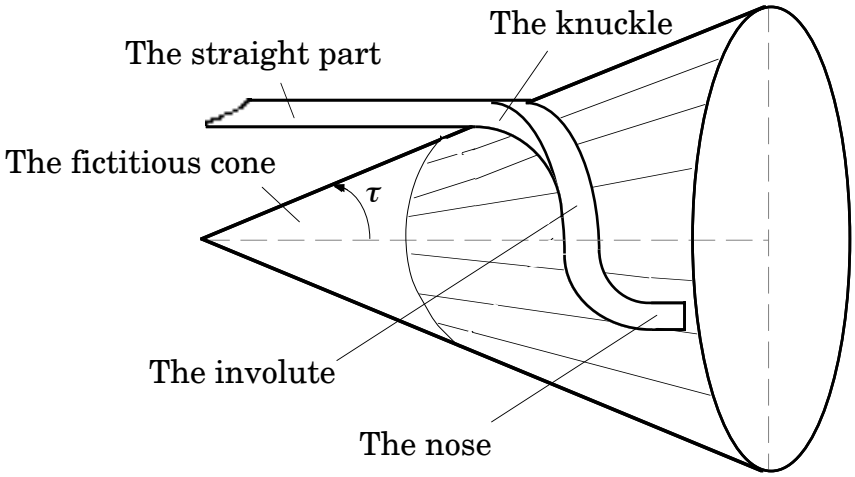

Figure 4.1 Different sections of the end part of a stator coil with a fictitious cone.

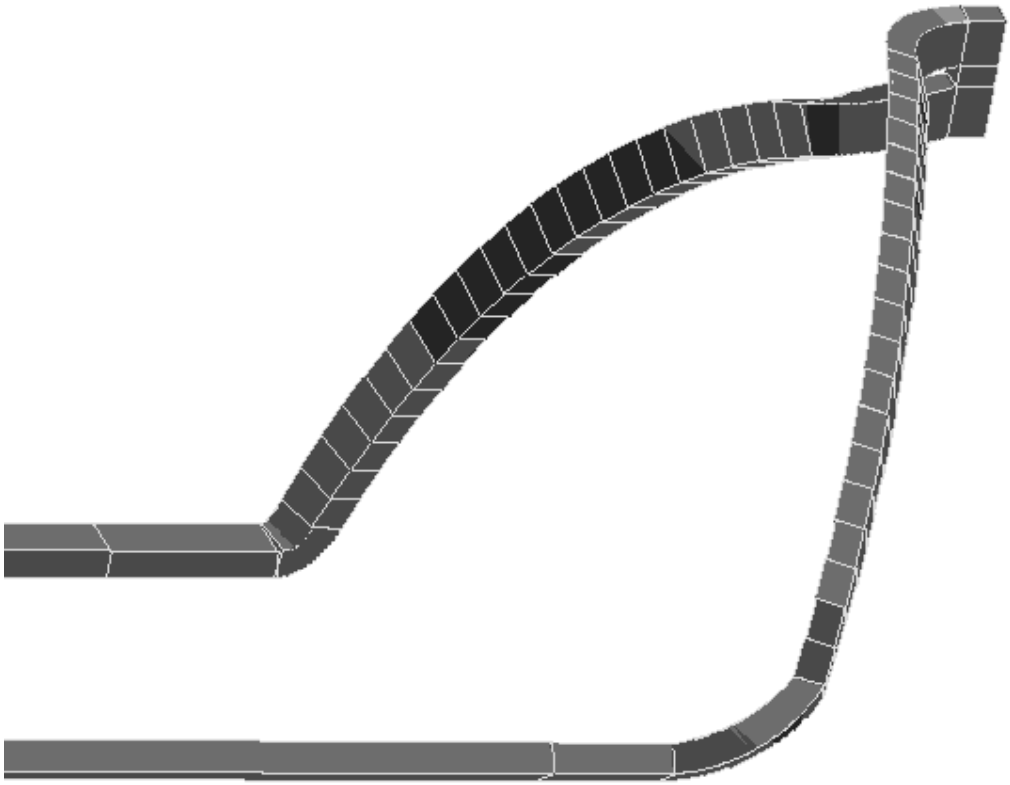

Figure 4.2 End parts of a stator coil.

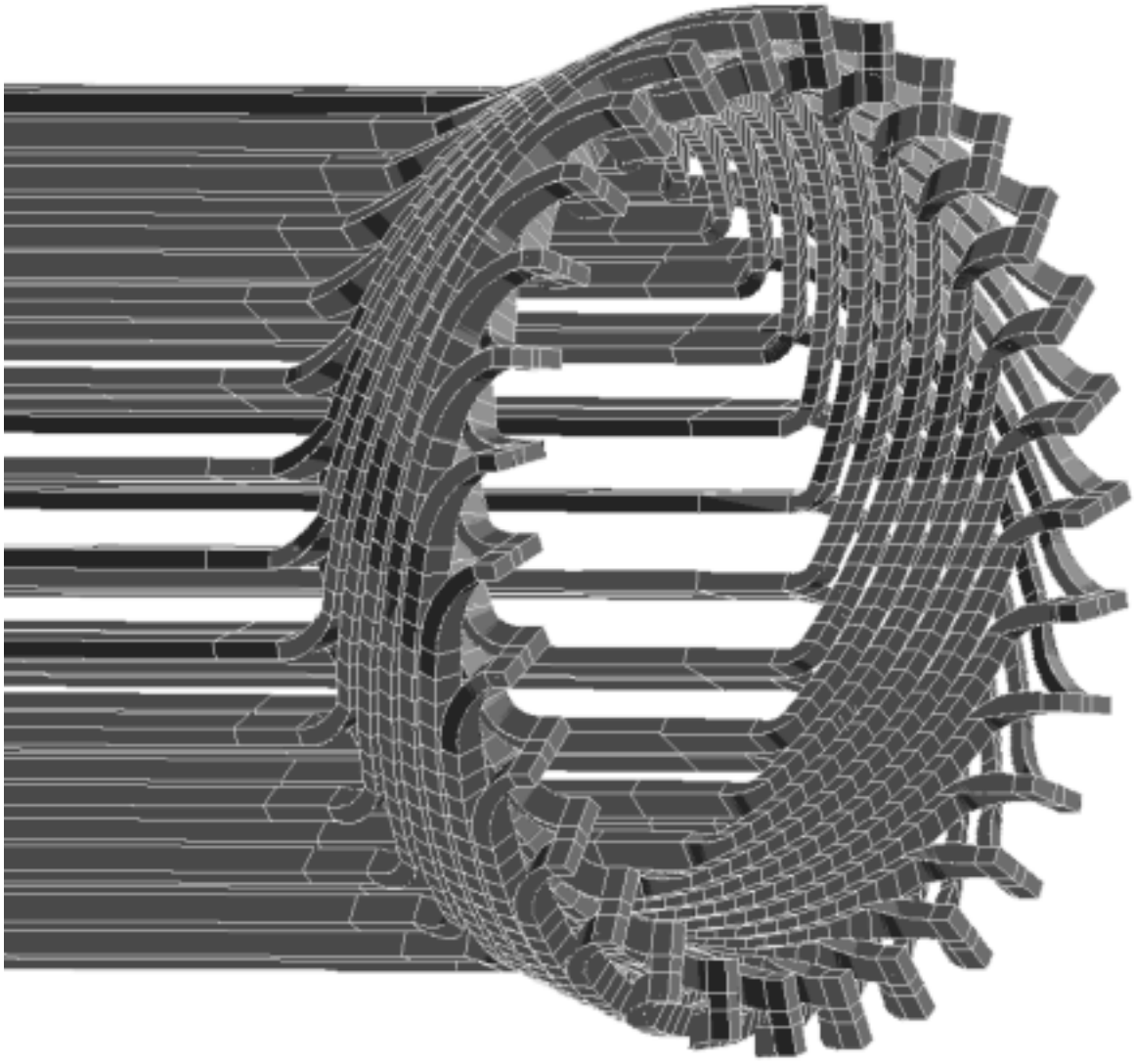

Figure 4.3 End parts of the stator winding.

Field Winding

Figure 4.4 describes the end parts of the field windingin one pole. The field winding consists of 12 coils. A typical coil is axial as it leaves the rotor body. Afterwards, the coil proceeds peripherally to the appropriate rotor slot on the other side of the pole. The coils lying nearest to the pole axis, i.e., the d-axis, are called pole coils. These pole coils differ from other coils of the field windingby the number of turns. In the considered machine, there are 2 pole coils and each pole coil has 6 turns, whereas the other coils, i.e., the normal coils, have 9 turns each. Because of symmetry, the coils in one pole have been geometrically modeled, and the remaining coils have been obtained by rotating the geometrically modeled coils by π radians. The field winding has also been parameterized.

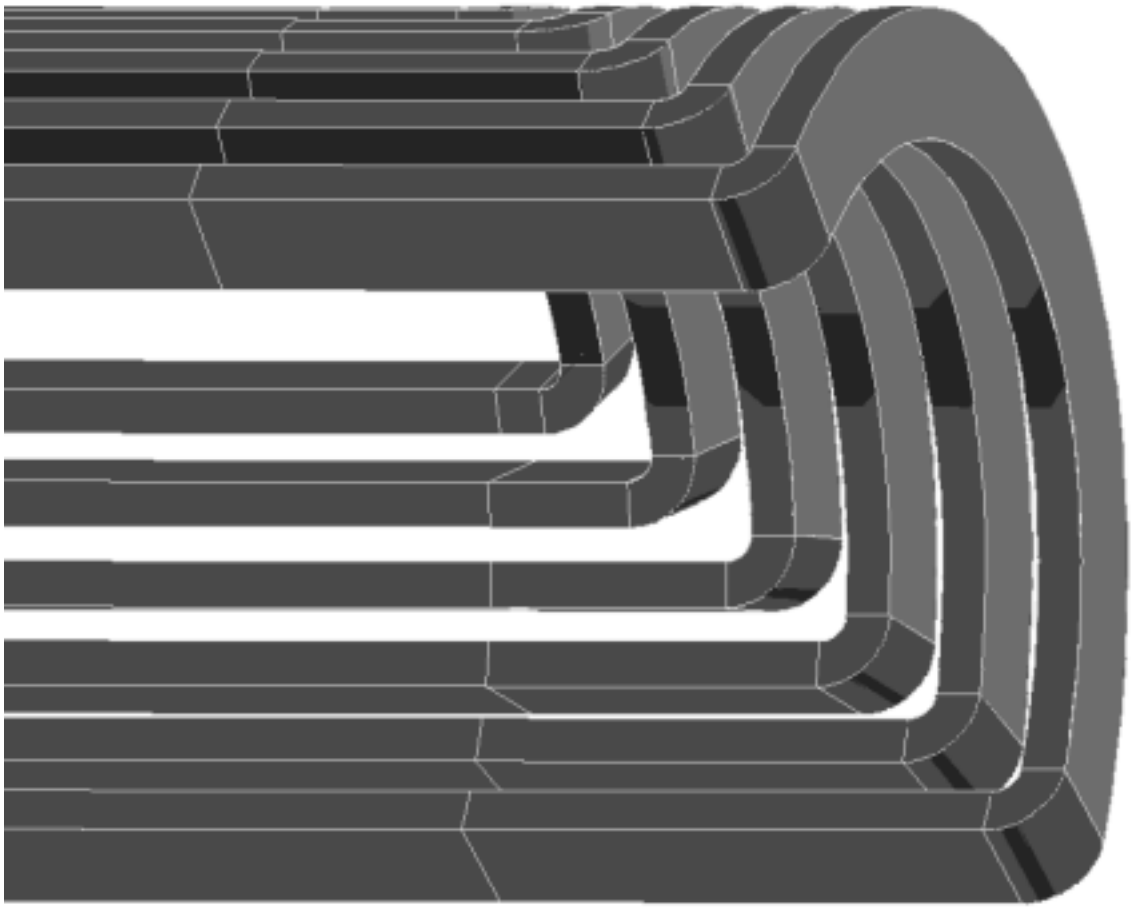

Figure 4.4 End parts of the field winding in one pole.

4.2 Review of Source-field Calculations

This section reviews various methods of calculating the source field $\boldsymbol{T}_0$. The vector field $\boldsymbol{T}_0$ can be evaluated from either Biot-Savart's law or Ampère's circuital law.

Biot-Savart's Law

The most straightforward choice for $\boldsymbol{T}_0$ is $\boldsymbol{H}_s$, the magnetic field due to the current density in free space, which can be computed from Biot-Savart's law. The magnetic field $\boldsymbol{H}_s$ can be expressed as

$$\boldsymbol{H}_s(\boldsymbol{r}) = \frac{1}{4\pi} \int_{V'} \frac{\boldsymbol{J}_c(\boldsymbol{r}') \times (\boldsymbol{r} - \boldsymbol{r}')}{|\boldsymbol{r} - \boldsymbol{r}'|^3} \, dV' \tag{4.1}$$

where V' is the volume of current-carrying coils and $\boldsymbol{r}$ and $\boldsymbol{r}'$ are the position vectors defining the field point and the source point, respectively.

In many problems, it is sufficient to assume that the cross-sectional area of the coils is negligible. This assumption is known as the filament approximation. Analytical expressions for $\boldsymbol{H}_S$ produced by filaments of various shapes, such as a circular arc of arbitrary length [77] and an infinitely long helical solenoid [78] have been studied. Concerning the windings of an electrical machine, Lawrenson [79] and Reece and Pramanik [80] took into account the involute shape of the stator end windings, replaced each coil with its central filament and evaluated the field $\boldsymbol{H}_S$ on the basis of Biot-Savart's law.

Furthermore, a coil may be decomposed into finite filaments, and the field $\boldsymbol{H}_S$, due to the coil, can then be obtained by superimposing the field contributions generated by each filament. This kind of numerical integration over the cross-section of the coil is time-consuming.

Analytical expressions for $\boldsymbol{H}_S$ produced by sheets of various shapes, such as a thin circular conic cylinder have been studied [81]. Concerning the windings of an electrical machine, Hammond and Ashworth [82, 83], as well as Tegopoulos [84] and Okuda [85] have considered the involute shape of the stator end windings and have represented each coil as a current sheet of zero thickness along its centre line. This representation has resulted in a thin cylindrical current sheet modeling the slot part and a thin conical current sheet modeling the end part.

In addition, a coil may, in general, be decomposed into finite sheets instead of filaments [86, 87]. In many cases, this kind of numerical integration across the coil is less time-consuming in comparison with the numerical integration over the cross-section of the coil.

Another method of calculating the magnetic field due to a coil consists of decomposing the coil into finite volumes, such as straight segments and circular arcs, whose contributions to the field $\boldsymbol{H}_S$ can be computed. After such a decomposition, the field $\boldsymbol{H}_S$, due to the coil, is obtained by summing up the expressions for the contributions from each minor volume. This method of decomposing a coil into finite volumes shows its distinct advantage in accuracy, stability and computation time over the method of decomposing the coil into filaments or sheets. An average time-saving by a factor of at least 4 is easily

achieved for the same accuracy [89]. Collie [90] has calculated the field $\boldsymbol{H}_s$ from a linearly varying current density with the only assumption that the sides of the elementary coil volume are planes. Urankar [91, 92] has evaluated the field $\boldsymbol{H}_s$ due to a finite arc segment of an n-sided polygonal cross-section with an arbitrarily oriented current density. Babic et al. [93, 94] have calculated the field $\boldsymbol{H}_s$ produced by a finite arc of a circular and rectangular cross-section with a constant current density. Azzerboni and Cardelli [88, 95] have calculated the field $\boldsymbol{H}_s$ due to an annular arc segment of a rectangular cross-section with a constant current density, as well as a sector or an entire disk coil with a radial current. Bodner et al. [96] have calculated the field $\boldsymbol{H}_s$ produced by a wedge-shaped prism.

The modeling method based on replacing volume distributions of current with equivalent distributions of fictitious magnetization, volume charges, as well as surface currents and charges has long been known. On the basis of this modeling technique, Ciric has presented a method called the surface-source modeling method [97, 98, 99, 100]. A coil is subdivided into segments of the same cross-sectional area as that of the coil. The segments lie in the direction of the current density, and their sides are generally of a trapezoidal shape. Ciric has calculated the field $\boldsymbol{H}_s$ due to coils of polygonal and rectangular cross-sections.

Ampère's Circuital Law

The use of edge elements for constructing the vector field $\boldsymbol{T}_0$ based on Ampère's circuital law, which is expressed as

$$\oint_{l'} \boldsymbol{T}_0 \cdot d\boldsymbol{l}' = \int_{S'} \boldsymbol{J}_c \cdot d\boldsymbol{S}' \tag{4.2}$$

has obtained attention in recent years. Equation (4.2) holds for any closed path l' with S' being the surface bounded by the curve l'. Moreover, Eq. (4.2) is the integral form of Eq. (3.14), which is the only requirement on $\boldsymbol{T}_0$.

The source field $\boldsymbol{T}_0$ is not uniquely defined by Eq. (4.2), so several possible choices are at our disposal. Webb and Forghani [31] have proposed a method based on holding Ampère's law around each face of the finite elements used in the discretization of the problem considered. In addition, Biro et al. [33] have described a method based on identifyingthe tree and the co-tree edges of the finite element mesh of the problem studied. Then, within each finite element, Ampère's law is enforced around the loop associated with a co-tree edge after assigning the value

zero to the line integrals of $\boldsymbol{T}_0$ along the tree edges of the loop. Furthermore, Albanese and Rubinacci [55] have proposed solving Eq. (3.14) by the FEM with edge elements to find $\boldsymbol{T}_0$.

An edge element representation of $\boldsymbol{T}_0$ prevents numerical difficulties in highly permeable regions when the reduced magnetic scalar potential Ψ is used in the non-conducting region comprising the coils, as discussed in Section 3.3. This is an important advantage of an edge element representation of $\boldsymbol{T}_0$.

Choice of Calculation Method

Constructing the vector field $\boldsymbol{T}_0$ based on Ampère's circuital law and following the methods proposed in [31, 33] requires the numerical integration of the current densities of the coils over either loops or finite element faces. This numerical integration presents no difficulties if the coils themselves are modeled by the finite element mesh. In addition, the method proposed in [55] requires the inclusion of the coils in the finite element mesh. The discretization of the coils presents a clear disadvantage in the case of complex coil geometries, such as stator end windings.

The calculation of the field $\boldsymbol{H}_s$ from Biot-Savart's law allows for the exclusion of the coils from the finite element mesh. The calculation methods based on decomposing a coil into thin filaments or sheets are time-consuming and suffer from the presence of singularities on the filaments and the sheets making accurate computations in the vicinity of and inside the coil difficult. Nevertheless, good results can be obtained at points remote from the coil. The calculation method based on decomposing a coil into finite volumes has a drawback in the case of complex coil geometries, such as stator end windings. This drawback is that stator end windings consist of twisted sections whose expressions for the field $\boldsymbol{H}_s$ are complicated. In addition, it is cumbersome to adjust twisted sections to each other in order to form stator end windings.

The surface-source modeling method is based on Biot-Savart's law and, thus, allows for the exclusion of the coils from the finite element mesh. This calculation method, based on decomposing a coil into segments, shows its distinct advantage in computation time over the method of decomposing the coil into finite volumes [99]. In addition, an appropriate number of segments can model complex coil geometries with a desired accuracy. Furthermore, the analytical expressions for the field $\boldsymbol{H}_s$ due to each segment contain only elementary functions. One drawback

is that these expressions become indeterminate for field points lying on the edges of the segment sides.

In this work, the surface-source modeling method is chosen to calculate the free-space field $\boldsymbol{H}_s$ from the complicated windings of electrical machines. In nodal elements, $\boldsymbol{H}_s$ is first computed at the nodes of the finite element mesh of the problem studied. Then, $\boldsymbol{H}_s$ is approximated by means of the nodal basis functions, as given by Eq. (3.58). In edge elements, the line integrals of $\boldsymbol{H}_s$ is first computed along the edges of the finite element mesh. The field $\boldsymbol{H}_s$ is then approximated by means of the edge basis functions, as given by Eq. (3.74).

4.3 Surface-source Modeling Method

4.3.1 Magnetization and Equivalent Current and Charge Densities

The surface-source modeling method is based on the following idea. In regions with ferromagnetic materials, the stationary or quasi-stationary magnetic field is described by

$$\boldsymbol{B} = \mu_0 \left(\boldsymbol{H} + \boldsymbol{M} \right) \tag{4.3}$$

where $\boldsymbol{M}$ is the magnetization vector. From the point of view of the magnetic field produced, a magnetized volume element is equivalent either to an elementary duplet of charges (electric dipole) or to an elementary current loop (magnetic dipole) [101]. On the basis of this equivalence, a distribution of magnetization can be modeled by means of an equivalent distribution of charges or currents.

In the case of a given volume distribution of magnetization $\boldsymbol{M}$, the equivalent volume and surface fictitious charge distributions in free space are given by

$$\rho_c = - \mu_0 \, \nabla \cdot \boldsymbol{M} \tag{4.4}$$

$$\rho_{sc} = - \mu_0 \, \boldsymbol{n}_{12} \cdot \left(\boldsymbol{M}_2 - \boldsymbol{M}_1 \right) \tag{4.5}$$

respectively, where $\boldsymbol{n}_{12}$ is the unit normal vector from side 1 to side 2 of each surface of discontinuity of $\boldsymbol{M}$, and $\boldsymbol{M}_1$ and $\boldsymbol{M}_2$ are the magnetization vectors at sides 1 and 2, respectively. Similarly, for the same case, the equivalent volume and surface fictitious current distributions in free space are given by

$$\boldsymbol{J}_{\mathrm{c}} = \nabla \times \boldsymbol{M} \tag{4.6}$$

$$\boldsymbol{J}_{\mathrm{sc}} = -\boldsymbol{n}_{12} \times \left(\boldsymbol{M}_2 - \boldsymbol{M}_1\right) \tag{4.7}$$

respectively.

4.3.2 Equations Defining the Method

A known distribution of volume current density $\boldsymbol{J}_{\mathrm{c}}$ in a non-magnetic material region of permeability μ_0 is considered. The surface-source modeling method is based on treating $\boldsymbol{J}_{\mathrm{c}}$ as if it would correspond to a fictitious magnetization vector $\boldsymbol{M}$. Consequently, $\boldsymbol{J}_{\mathrm{c}}$ can be replaced by $\boldsymbol{M}$ and a surface current density $\boldsymbol{J}_{\mathrm{sc}}$, as shown in Eqs. (4.6) and (4.7). The current density $\boldsymbol{J}_{\mathrm{sc}}$ exists on all the surfaces where the tangential component of $\boldsymbol{M}$ is discontinuous. Thus, the magnetic field due to $\boldsymbol{J}_{\mathrm{c}}$ in free space can be expressed as

$$\boldsymbol{H}_{\mathrm{s}} = \boldsymbol{M} + \boldsymbol{H}_M + \boldsymbol{H}_{J\mathrm{sc}} \tag{4.8}$$

where $\boldsymbol{H}_M$ and $\boldsymbol{H}_{J\mathrm{sc}}$ are the magnetic fields due to $\boldsymbol{M}$ and $\boldsymbol{J}_{\mathrm{sc}}$, respectively. On the other hand, $\boldsymbol{M}$ can be replaced by equivalent volume and surface charge densities, as shown in Eqs. (4.4) and (4.5). The surface charge density ρ_{sc} exists on all the surfaces where the normal component of $\boldsymbol{M}$ is discontinuous. Thus, $\boldsymbol{H}_M$ can be expressed as

$$\boldsymbol{H}_M = \boldsymbol{H}_{\rho\mathrm{c}} + \boldsymbol{H}_{\rho\mathrm{sc}} \tag{4.9}$$

where $\boldsymbol{H}_{\rho\mathrm{c}}$ and $\boldsymbol{H}_{\rho\mathrm{sc}}$ are the magnetic fields due to ρ_{c} and ρ_{sc}, respectively.

In other words, in a region of permeability μ_0, the field $\boldsymbol{H}_{\mathrm{s}}$, due to a distribution of volume current density $\boldsymbol{J}_{\mathrm{c}}$, can be obtained by the superposition of the magnetization vector $\boldsymbol{M}$ and the magnetic fields due to the volume charge distribution, the surface charge distribution and the surface current distribution, i.e.,

$$\boldsymbol{H}_{\mathrm{s}}(\boldsymbol{r}) = \boldsymbol{M}(\boldsymbol{r}) + \frac{1}{4\pi\mu_0}\left(\int_{V'} \frac{\rho_{\mathrm{c}}\,(\boldsymbol{r}'-\boldsymbol{r})\boldsymbol{R}}{R^3}\,\mathrm{d}V' + \int_{S'} \frac{\rho_{\mathrm{sc}}\,(\boldsymbol{r}'-\boldsymbol{r})\boldsymbol{R}}{R^3}\,\mathrm{d}S' \right) + \frac{1}{4\pi}\int_{S'} \frac{\boldsymbol{J}_{\mathrm{sc}}(\boldsymbol{r}'-\boldsymbol{r})\times\boldsymbol{R}}{R^3}\,\mathrm{d}S' \tag{4.10}$$

where $\boldsymbol{R} = \boldsymbol{r} - \boldsymbol{r}'$ and S' is the surface of discontinuity of $\boldsymbol{M}$ over which the surface integrals are calculated.

The fictitious magnetization $\boldsymbol{M}$ is not uniquely determined by Eq. (4.6) alone. More than one model for $\boldsymbol{M}$ can be easily constructed for a given current distribution, since we do not impose any condition for its divergence [97]. Thus, the price paid for applying the surface-source modeling method is the construction of an appropriate distribution of $\boldsymbol{M}$ for a given problem.

A few special cases are particularly important for the computation of $\boldsymbol{H}_{\mathrm{s}}$. If $\boldsymbol{M}$ is chosen so that ρ_{c} in Eq. (4.4) is zero everywhere, the volume current distribution is modeled in terms of $\boldsymbol{M}$ and only surface distributions of charges and currents. Consequently, the field in Eq. (4.10) will be expressed in terms of surface integrals requiring a reduced amount of computation in comparison with the volume integral in Biot-Savart's formula. Moreover, when $\boldsymbol{M}$ is chosen to be zero outside regions with $\boldsymbol{J}_{\mathrm{c}} \neq \boldsymbol{0}$, these surface integrals are taken only over the boundary of those regions.

4.3.3 Computation of the Free-space Field $\boldsymbol{H}_{\mathrm{s}}$ Due to a Coil

In general, a coil can approximately be decomposed into straight segments of the same cross-sectional area as that of the coil. The sides of these straight segments are of a trapezoidal shape along the current direction, as shown in Fig. 4.5. From the point of view of the magnetic field produced, any volume distribution of current density $\boldsymbol{J}_{\mathrm{c}}$ can be replaced by equivalent distributions of fictitious magnetization $\boldsymbol{M}$, surface current density $\boldsymbol{J}_{\mathrm{sc}}$ and negative and positive surface charge densities ρ_{sc}. No volume charge distribution is present if $\boldsymbol{M}$ is chosen so that its divergence is zero everywhere.

For the sake of clarity concerning the choice of $\boldsymbol{M}$ and the determination of $\boldsymbol{J}_{sc}$ and ρ_{sc}, a coil of a rectangular cross-section is considered. The coil is decomposed into straight segments. Figure 4.6 illustrates one such straight segment. The six sides of every straight segment are denoted in the same manner with respect to the current direction, for instance, g = 0, 1, 2, 3, 4, 5 so that two sides with the same g from adjacent segments have a common edge. The Cartesian x, y, z coordinate system shown in Fig. 4.6 is the global coordinate system of the entire coil. The Cartesian x_1, y_1, z_1 coordinate system is a local coordinate system corresponding to each straight segment in such a way that the x_1-axis and the z_1-axis are in the same direction as that of $\boldsymbol{J}_c$ and $\boldsymbol{M}$, respectively. This choice of x_1, y_1, z_1 coordinate system simplifies the determination of $\boldsymbol{M}$.

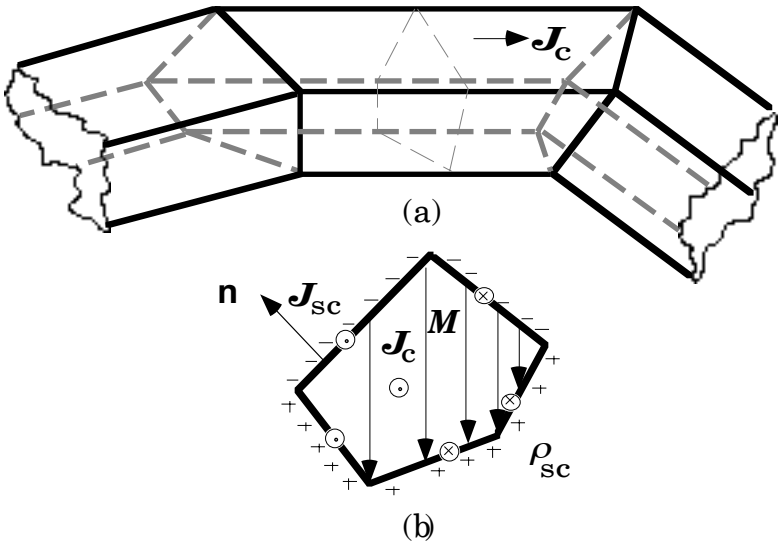

Figure 4.5 Model construction of a coil of polygonal cross-section. (a) Straight segment. (b) Cross-section with fictitious magnetization and surface current and charge.

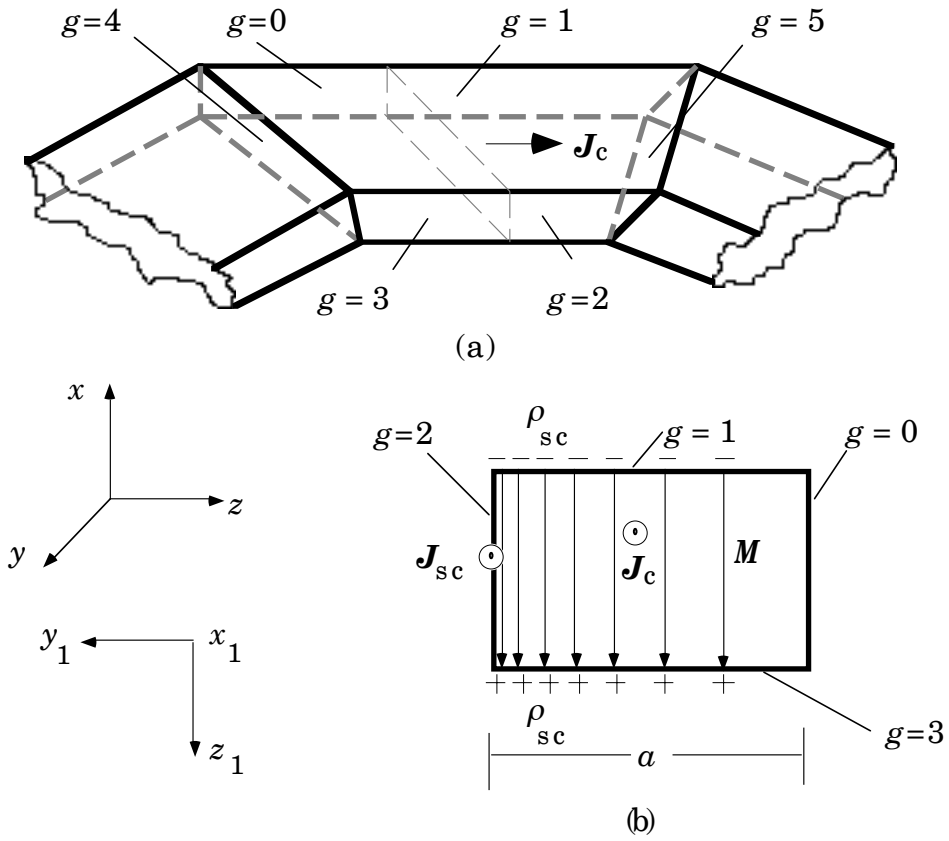

Figure 4.6 Model construction of a coil of rectangular cross-section. (a) Six sides g of a straight segment. (b) Cross-section with fictitious magnetization and surface current and charge.

For a homogeneous medium of permeability μ_0 and in the local Cartesian x_1, y_1, z_1 coordinate system, the choice of $\boldsymbol{M}$ and the determination of $\boldsymbol{J}_{\mathrm{sc}}$ and ρ_{sc} are as follows:

Choice of Fictitious Magnetization $\boldsymbol{M}$

The fictitious magnetization $\boldsymbol{M}$ can be chosen to be zero outside the current-carrying region [99]. According to Eq. (4.6), the direction of $\boldsymbol{M}$ is perpendicular to that of $\boldsymbol{J}_{\mathrm{c}}$ in the considered segment. For a uniformly distributed current, the magnitude of $\boldsymbol{M}$ increases linearly with the distance in the direction of $\boldsymbol{M} \times \boldsymbol{J}_{\mathrm{c}}$. Moreover, in the local coordinate system, $\boldsymbol{M}$ has only one component in the z_1-direction, and $\boldsymbol{J}_{\mathrm{c}}$ has only one component in the x_1-direction. Thus, Eq. (4.6) yields

$$\frac{\partial M}{\partial y_1} = J_{\mathrm{c}} \tag{4.11}$$

Integrating Eq. (4.11), we get

$$M = \int_{y_{10}}^{y_1} J_c \, dy_1 \tag{4.12}$$

where y_{10} is the reference point of $\boldsymbol{M}$ in the local coordinate system, i.e., $M = 0$ at y_{10}. As $\boldsymbol{J}_c$ is assumed to be constant within each straight segment and over the corresponding cross-section, Eq. (4.12) gives

$$M = J_c \left(y_1 - y_{10} \right) + C \tag{4.13}$$

where C is a constant of integration. Thus, $\boldsymbol{M}$ depends linearly on the distance from side 0 with $M = 0$ to side 2 with $M = J_c \, a$, where a is the width of the coil as described in Fig. 4.6 (b).

Since $\boldsymbol{M}$ only depends on y_1, as given in Eq. (4.13), the divergence of $\boldsymbol{M}$ is

$$\nabla \cdot \boldsymbol{M} = 0 \tag{4.14}$$

Equations (4.4) and (4.14) yield that no volume charge density ρ_c is present. Thus, Eq. (4.10) contains only surface integrals.

Determination of the Surface Current Density $\boldsymbol{J}_{sc}$

According to Eq. (4.7) and the assumption of zero magnetization outside the current-carrying region, a uniform surface current density $\boldsymbol{J}_{sc}$ exists on all the surfaces where the tangential component of $\boldsymbol{M}$ is discontinuous. Consequently, $\boldsymbol{J}_{sc}$ flows over side 2 in the direction of $\boldsymbol{J}_c$ and is given by

$$\boldsymbol{J}_{sc} = \boldsymbol{J}_c \, a \tag{4.15}$$

On sides 4 and 5, the total surface current densities given by Eq. (4.7) and obtained by the superposition of the contributions from adjacent segments are equal to zero [99].

Determination of the Surface Charge Density ρ_{sc}

According to Eq. (4.5), negative and positive surface charge densities ρ_{sc} exist on all the surfaces where the normal component of $\boldsymbol{M}$ is discontinuous. Consequently, ρ_{sc} are present on sides 1 and 3, respectively. In the same way as for $\boldsymbol{M}$, ρ_{sc}

increases linearly with the distance in the direction of $\boldsymbol{M} \times \boldsymbol{J}_c$ from side 0 where $\rho_{sc} = 0$ to side 2 where

$$|\rho_{sc}| = \rho_d = \mu_0 J_c a \tag{4.16}$$

On sides 4 and 5, there are positive or negative charges varying linearly from side 0 where $\rho_{sc} = 0$ to side 2 where ρ_{sc} is given by Eq. (4.5).

Evaluation of the Field $\boldsymbol{H}_s$

Ciric [99, 100] has derived the expressions for the contribution of a straight segment to the resultant free-space field $\boldsymbol{H}_s$. The expressions obtained due to a trapezoidal side are of a simple algebraic structure. They are expressed in terms of the distances from the field point to the vertices of the trapezoidal side, the angle under which the trapezoidal side is seen from the field point, as well as elementary functions. However, the expressions obtained by Ciric become indeterminate for field points lying on the edges of the trapezoidal side. This indeterminacy is treated in the Appendix.

The resultant free-space field at a field point is obtained by adding the contributions of all the straight segments composing the coil. The accuracy of the field $\boldsymbol{H}_s$ increases by increasing the number of segments in the curved parts of the coil.

4.4 Computation of the Free-space Field $\boldsymbol{H}_s$ Due to the Windings of an Electrical Machine

The free-space field $\boldsymbol{H}_s$ due to each coil of the stator and field windings is computed by the surface-source modeling method. The resultant field $\boldsymbol{H}_s$ is, then, evaluated by vectorially adding up the contributions from all the coils.

In steady state, the space vectors are constant in the rotor reference frame. The space vectors of the stator voltage and current are given by

$$\boldsymbol{u}_s^r = u_d + \mathrm{j} u_q \tag{4.17}$$

$$\boldsymbol{i}_s^r = i_d + \mathrm{j} i_q \tag{4.18}$$

where the subscripts d and q represent the direct- and quadrature-axis components of the quantity in question [102]. The steady-state equations of a synchronous machine are

$$\begin{aligned} u_d &= R_s\, i_d - \omega\, \psi_q \\ u_q &= R_s\, i_q + \omega\, \psi_d \\ u_f &= R_f\, i_f \\ \psi_d &= L_d\, i_d + L_{md}\, i_f \\ \psi_q &= L_q\, i_q \\ \psi_f &= L_{md}\, i_d + L_f\, i_f \end{aligned} \tag{4.19}$$

where L_d is the direct-axis synchronous inductance, L_q is the quadrature-axis synchronous inductance, L_{md} is the direct-axis magnetizing inductance, L_f is the inductance of the field winding, ψ_d and ψ_q are the d- and q-components of the stator flux linkage, respectively, ψ_f is the field flux linkage, u_f is the field voltage, ω is the angular frequency and R_s and R_f are the resistances of the stator and field windings, respectively. The field current i_f is referred to the stator winding and produces the same fundamental flux density as the actual field current i_F. The relation between i_f and i_F is

$$i_f = \frac{2}{3}\,\frac{k_{wr}}{k_{ws}}\,\frac{N_r}{N_s}\, i_F \tag{4.20}$$

where N_r and N_s are the numbers of turns in series of field and stator windings, respectively, and k_{wr} and k_{ws} are the field and stator windingfactors, respectively [103].

The space vector diagram shown in Fig. 4.7 corresponds to an overexcited synchronous generator in steady state. The motor convention is chosen as a base.

The d-q components of the stator voltage and current are given by

$$\begin{aligned} u_d &= \hat{u}_s \sin\delta \\ u_q &= \hat{u}_s \cos\delta \\ i_d &= \hat{i}_s \sin(\delta + \varphi) \\ i_q &= \hat{i}_s \cos(\delta + \varphi) \end{aligned} \tag{4.21}$$

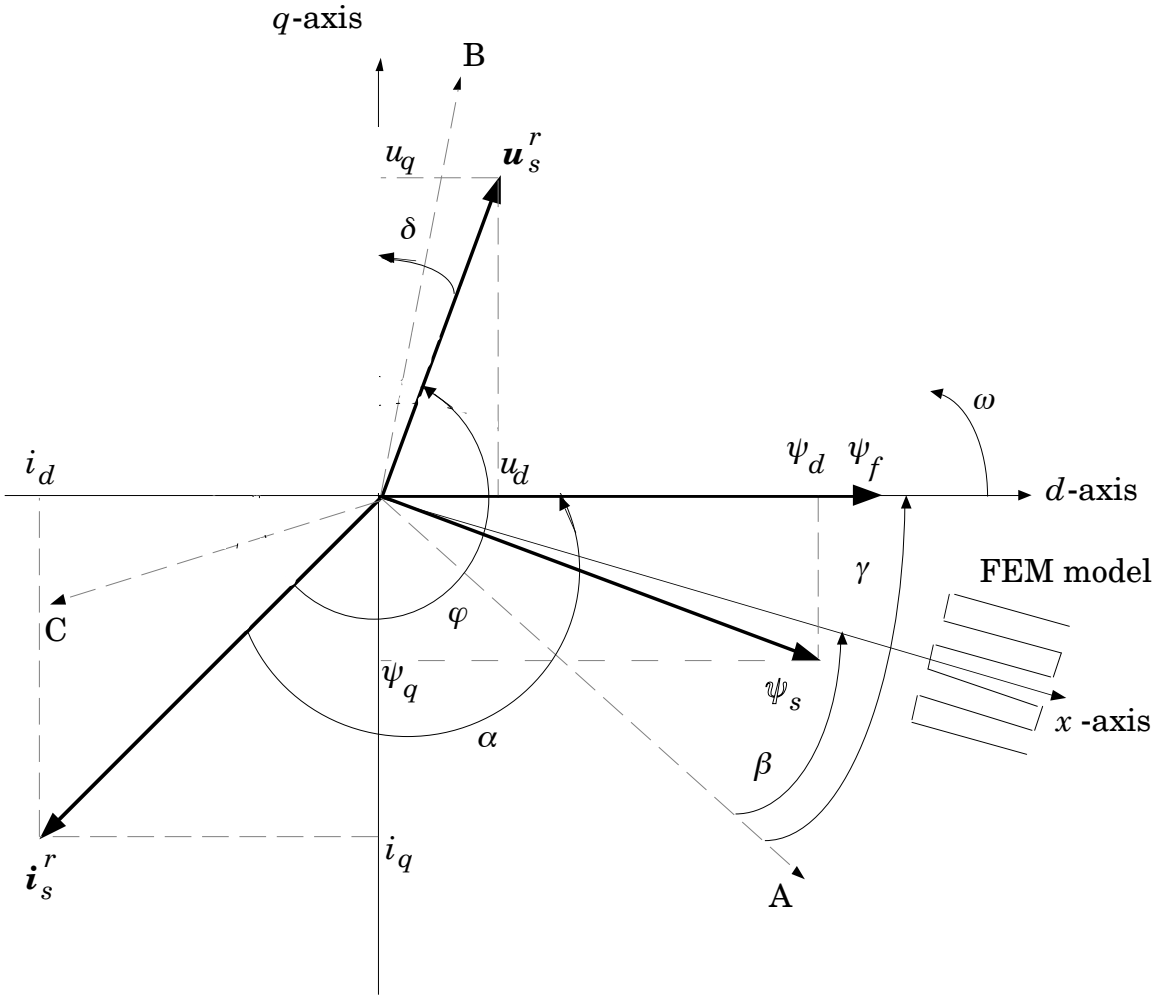

Figure 4.7 Space vector diagram of an overexcited synchronous generator in steady state.

where $\hat{u}_s$ is the stator phase voltage amplitude, $\hat{i}_s$ is the stator current amplitude, φ is the angle of the stator voltage vector with respect to the stator current vector, and δ is the load angle, which can be solved by

$$\tan(\delta) = \frac{-\omega L_q \hat{i}_s \cos(\varphi)}{\hat{u}_s - \omega L_q \hat{i}_s \sin(\varphi)} \tag{4.22}$$

neglecting the stator resistance. The space vector of the stator flux linkage is given by

$$\underline{\psi}_s = (L_d i_d + L_{md} i_f) + \mathrm{j} L_q i_q \tag{4.23}$$

based on Eq. (4.19). It is preferable to express $\underline{\psi}_s$ in terms of L_d and L_q. Therefore, a current i'_f is defined such that [104]

$$i_f' = \frac{L_{md}}{L_d}\, i_f \tag{4.24}$$

The space vector of ψ_s can then be expressed as

$$\psi_s = L_d \left(i_d + i_f' \right) + \mathrm{j}\, L_q\, i_q \tag{4.25}$$

The current i'_f can be derived from the expression of the stator voltage space vector. If the stator resistance R_s is neglected, the stator voltage space vector is given by

$$\begin{aligned} \boldsymbol{u}_s^r &= u_d + \mathrm{j} u_q \\ &= -\omega\, L_q\, i_q + \mathrm{j}\, \omega\, L_d\, i_d + \mathrm{j}\, \omega\, L_d\, i_f' \end{aligned} \tag{4.26}$$

based on Eq. (4.17), (4.19) and (4.24). The current i'_f is then given by

$$i_f' = \frac{\boldsymbol{u}_s^r + \omega\, L_q\, i_q - \mathrm{j}\, \omega\, L_d\, i_d}{\mathrm{j}\, \omega\, L_d} \tag{4.27}$$

The model discretized by the finite element method, where the eddy-current losses are to be calculated is denoted by the "FEM model" in Fig. 4.7. The x-axis shown is the axis on which the FEM model lies.

In a balanced three-phase system, the instantaneous values of the stator currents are given by

$$\begin{aligned} i_a &= \hat{\imath}_s \cos(\gamma - \alpha) \\ i_b &= \hat{\imath}_s \cos\left(\gamma - \alpha - \frac{2\pi}{3} \right) \\ i_c &= \hat{\imath}_s \cos\left(\gamma - \alpha + \frac{2\pi}{3} \right) \end{aligned} \tag{4.28}$$

where γ is defined as

$$\gamma = \omega\, t + \gamma_0 \tag{4.29}$$

the angle between the magnetic axis of phase A and the d-axis, as illustrated in Fig. 4.7, with γ_0 being the angle γ at $t = 0$. The angle α is between the stator current space vector and the d-axis and is given by

$$\alpha = \varphi + \delta - 90° \tag{4.30}$$

If the FEM model includes a slot pitch, a phase belt or a pole pitch, the air-gap magnetic field is assumed to be a rotating field. On the other hand, if the FEM model includes only half a slot pitch, the air-gap magnetic field is assumed to be an alternating field. In this latter case, a certain instant of time at which ψ_s is maximum at the FEM model is to be chosen in order to determine the currents to be used in the alternating-field solution. This instant of time corresponds to a rotor position where the part of ψ_s lying in the direction normal to the x-axis is zero, and Eq. (4.25) yields

$$L_d \left(i_d + i_f^{\copyright}\right) \sin\left(\gamma - \beta\right) + L_q \; i_q \cos\left(\gamma - \beta\right) = 0 \tag{4.31}$$

where β is the angle between the magnetic axis of phase A and the x-axis. Equation (4.31) gives the angle $\gamma - \beta$ as

$$\tan\left(\gamma - \beta\right) = \frac{- L_q \; i_q}{L_d \left(i_d + i_f^{\copyright}\right)} \tag{4.32}$$

Under no-load conditions, $\gamma - \beta$ is equal to zero and the d-axis coincides with the x-axis.

Using Eqs. (4.30) and (4.32), the instantaneous values of the stator currents given by Eq. (4.28) can be determined. These currents are the amplitudes of the stator currents used in the alternating-field solution. The field and stator currents, used in the finite element solution, then vary sinusoidally with respect to time without phase shifts and are given by

$$\begin{aligned} i_F^{\copyright}\left(t\right) &= i_F \cos\left(\omega \, t\right) \\ i_a^{\copyright}\left(t\right) &= i_a \cos\left(\omega \, t\right) \\ i_b^{\copyright}\left(t\right) &= i_b \cos\left(\omega \, t\right) \\ i_c^{\copyright}\left(t\right) &= i_c \cos\left(\omega \, t\right) \end{aligned} \tag{4.33}$$

5 Sample Calculations

Many investigations into various formulations and finite elements have been carried out. It is, however, important to compare different techniques and to apply them to problems in electrical machinery. A comparison of the formulations should be made in conjunction with a comparison of the finite elements. In this chapter, the $\boldsymbol{T}-\Psi,\Psi$, the $\boldsymbol{T}-\Omega,\Omega$, the $\boldsymbol{A}-V,\Psi$ and the $\boldsymbol{A},\Psi$ formulations, where the vector potentials are approximated by nodal or edge basis functions, are applied to five eddy-current problems. Two of the problems are benchmark problems from International Eddy Current Workshops, whereas three problems deal with electrical machinery. The latter problems illustrate, among others, the applicability of the surface-source modeling method to the windings of electrical machines.

Two of the problems studied, the Bath Cube and the Asymmetrical Conductor with a Hole, are benchmark problems 5 and 7, respectively [105]. The $\boldsymbol{T}-\Psi,\Psi$, the $\boldsymbol{A}-V,\Psi$ and the $\boldsymbol{A},\Psi$ formulations in association with hexahedral and tetrahedral, nodal and edge elements are applied and compared. In addition, the rate of convergence of the different formulations is investigated. The results obtained are compared with the results of the measurements carried out at the Bath University (the Bath Cube problem) and at the Okayama University (the Asymmetrical Conductor with a Hole problem).

The third problem is a 120 MVA hydrogenerator running at no load. The surface-source modeling method is investigated. The $\boldsymbol{T}-\Psi,\Psi$, the $\boldsymbol{T}-\Omega,\Omega$ and the $\boldsymbol{A}-V,\Psi$ formulations in association with hexahedral nodal and edge elements are applied and compared. The results are also compared with those obtained by Sande [44].

The fourth problem is a 635 MVA turbogenerator running at no-load and at load. The $\boldsymbol{T}-\Psi,\Psi$ formulation in association with hexahedral edge elements, as well as the $\boldsymbol{A},\Psi$ formulation in association with hexahedral nodal elements, are applied and compared.

The fifth problem is a 13 MVA synchronous motor with solid pole shoes during starting. The $\boldsymbol{A}-V,\Psi$ formulation in association with hexahedral nodal elements is applied. Measurements of the temperature and the magnetic flux density are presented. Some calculated and measured results are illustrated.

In the cases where CPU-times are compared, the models were run on an HP 9000/780/C160 workstation with a clock frequency of 160 MHz and 512.5 MB RAM. In these cases, no other major processes were running simultaneously, and a CPU-utilization of more than 99 % was achieved. The measured time is the actual time used and is very close to the actual CPU-time because of the high CPU-utilization.

5.1 Program Package

The implementation of the different techniques used in this research project has resulted in a program package called 3FEMEC for the numerical solution of three-dimensional eddy-current problems by the finite element method. The program 3FEMEC is based on a finite element software developed by Keskinen [72] and allowing various formulations in combination with nodal finite elements to be used. Keskinen 's program was further developed implementing three major tasks. First, the hexahedral and tetrahedral low-order edge elements were implemented in association with the $\boldsymbol{T}-\Psi,\Psi$, the $\boldsymbol{A}-V,\Psi$ and the $\boldsymbol{A},\Psi$ formulations. Second, the windings of electrical machines were parameterized and the surface-source modeling method was implemented enabling the evaluation of the free-space field $\boldsymbol{H}_{\mathrm{s}}$ due to a given source current distribution. Third, the anisotropic conductivity and permeability of laminated regions were treated. The computations were performed by double precision arithmetic.

The commercial program MSC/PATRAN was used as a pre- and post-processor [106]. An interface program between MSC/PATRAN and 3FEMEC was developed. MSC/PATRAN as a preprocessor is used to create the finite element mesh as well as to set material properties and boundary conditions. On the other hand, MSC/PATRAN as a post-processor is used to visualize field quantities, such as the magnetic flux density, the eddy-current density, the field $\boldsymbol{H}_{\mathrm{s}}$, as well as various potentials.

Since MSC/PATRAN does not generate data for the edges of the model studied, an interface program was developed to generate the model edges, as well as to split the graph into a tree and a co-tree, according to the algorithm proposed by Kettunen [107].

A brief description of the main steps of 3FEMEC follows here. The field $\boldsymbol{H}_{\mathrm{s}}$ is first evaluated. Then, the Dirichlet boundary condition of the magnetic scalar potential,

Eq. (3.39) is calculated. The calculated values of the field $\boldsymbol{H}_s$ are used to create the right-hand side of the matrix equation (3.68). This right-hand side must be adjusted due to Dirichlet boundary conditions. The remaining part of the field is then solved by the finite element method. Finally, the potentials and the field $\boldsymbol{H}_s$ are used to calculate field quantities, such as the magnetic flux density as vector values per element or component values along a given line. The eddy-current density and losses are also calculated.

5.2 Bath Cube Problem

The Bath Cube problem [105] is illustrated in Fig. 5.1. Four conducting cubes are located symmetrically under a pole. The field is produced by a sinusoidal magnetomotive force of 1000 A varying at a frequency of 50 Hz between the pole and the box. The permeability of the pole and the surrounding box is supposed to be infinite. The surfaces of the pole and the box are, therefore, equipotential surfaces of the magnetic scalar potential with 1000 $\angle 0°$ A and 0 $\angle 0°$, respectively. The conductivity of the cubes is $2.703 \cdot 10^7$ Sm^{-1}.

Because of the symmetry, only the quarter where $x, y, z \geq 0$ is considered. Two finite element meshes are used in association with the Bath Cube problem. These meshes apply hexahedral and tetrahedral finite elements and are denoted by BATH and BATHTET, respectively. Both the first-order nodal and low-order edge finite elements are used. The meshes are described in Table 5.1.

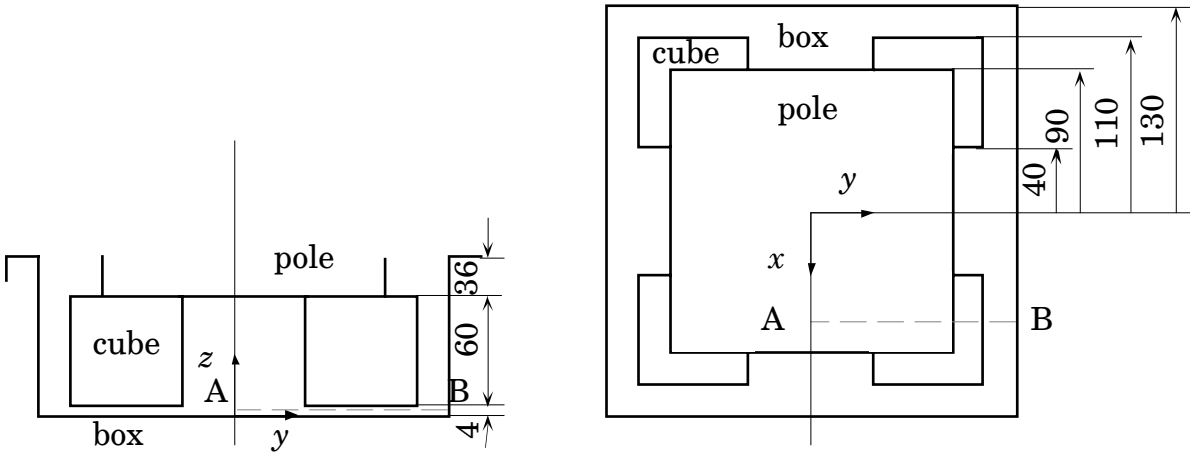

Figure 5.1 Geometry of the Bath Cube problem: a) front view, b) plan view. The dimensions are in millimeters.

Table 5.1 Finite element meshes BATH and BATHTET used in the Bath Cube problem.

	BATH	BATHTET
Number of nodes in the model	2 258	4 018
Number of nodes in the conducting region	448	720
Number of edges in the model	6 186	21 577
Number of edges in the conducting region	1 168	3 557
Number of finite elements	1 711	16 040

Since the conductivity of the cubes is homogeneous, there is no need to introduce the electric scalar potential in the conducting region and the $\boldsymbol{A}, \Psi$ formulation is used. The discussion of the accuracy of the field solution is limited to the $\boldsymbol{T} - \Psi, \Psi$ and the $\boldsymbol{A}, \Psi$ formulations. Nodal basis functions are used to approximate the scalar potential Ψ, and both nodal and edge basis functions are used to approximate the vector potentials $\boldsymbol{T}$ and $\boldsymbol{A}$.

When the $\boldsymbol{T} - \Psi, \Psi$ formulation is used, the boundary conditions (3.26) and (3.39) must be fulfilled.Equation (3.26) yields that the tangential components of $\boldsymbol{T}$ are set to zero on the cube faces. Equation (3.39) gives a Dirichlet boundary condition for Ψ at the pole faces ($\Psi = 1000$ A) and the box faces ($\Psi = 0$).

When the $\boldsymbol{A}, \Psi$ formulation is used, the boundary condition (3.39) must be fulfilled. In addition, when nodal basis functions are used to approximate $\boldsymbol{A}$, Eq. (3.29) must be satisfied, thus, yieldingthat the normal component of $\boldsymbol{A}$ is set to zero on the cube faces.

Furthermore, no flux is assumed to cross the symmetry planes and the surface connecting the pole and the box on top of the model. Thus, on these surfaces, a homogeneous Neumann boundary condition for Ψ is applied.

5.2.1 Accuracy of the Field Solution

The measured [108] and calculated modulus and argument of the z-component of the magnetic flux density along line A-B are shown in Figs. 5.2 to 5.5. Line A-B is defined as $x = 70$ mm, y from 0 to 130 mm and $z = 2$ mm.

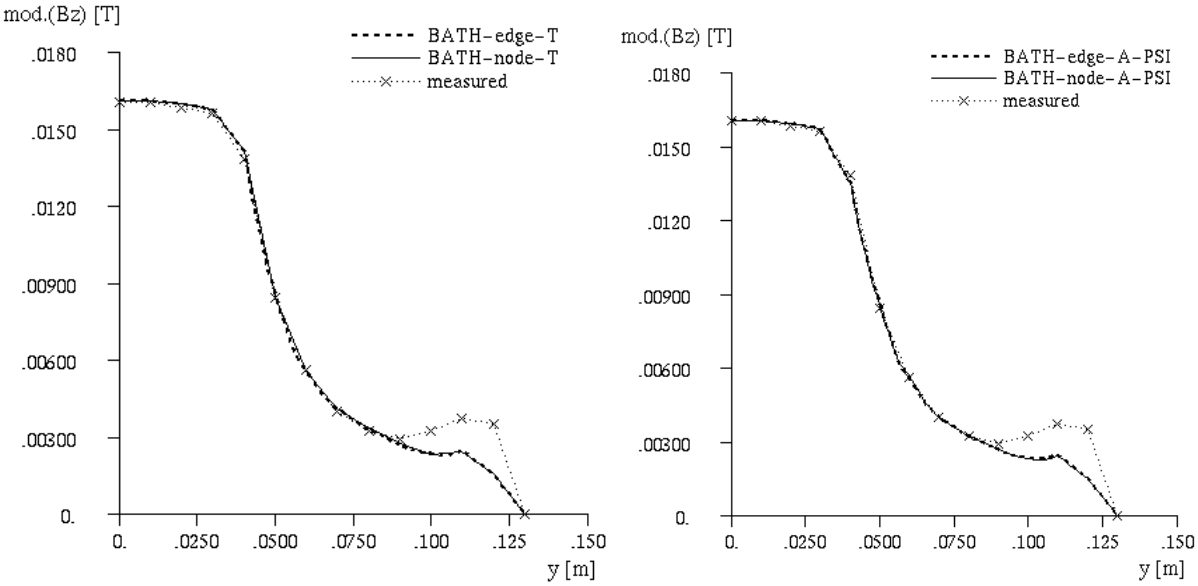

Figure 5.2 Measured and calculated modulus of the z-component of the flux density along line A-B in the Bath Cube problem obtained by means of the hexahedral finite elements and a) the $\boldsymbol{T}-\Psi,\Psi$ formulation and b) the $\boldsymbol{A},\Psi$ formulation.

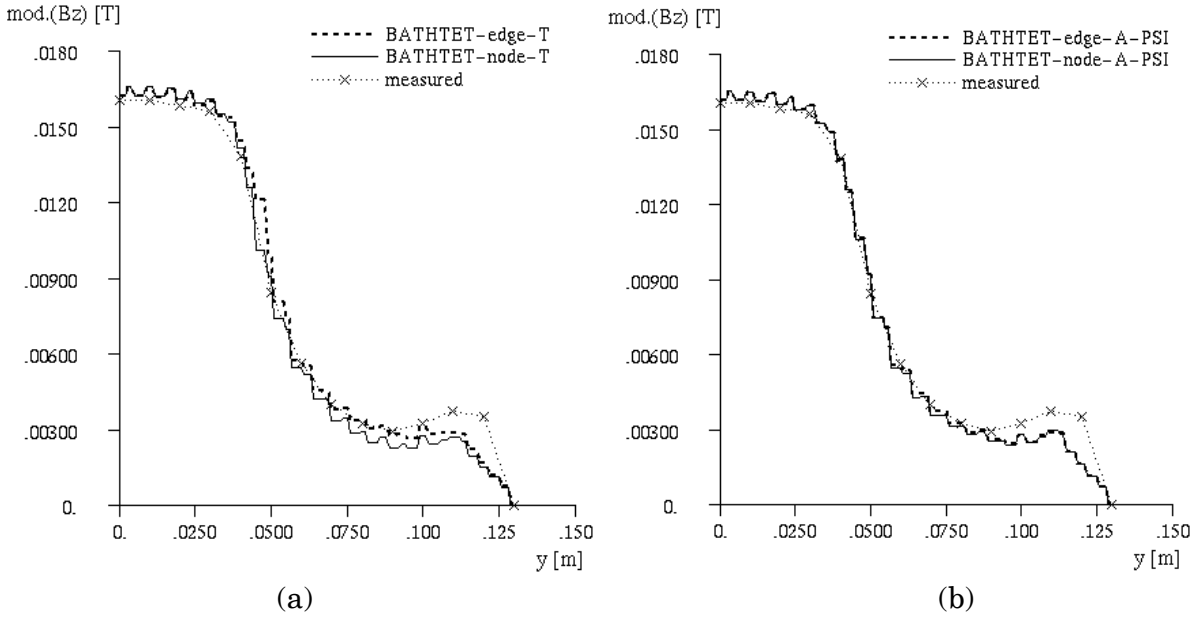

Figure 5.3 Measured and calculated modulus of the z-component of the flux density along line A-B in the Bath Cube problem obtained by means of the tetrahedral finite elements and a) the $\boldsymbol{T}-\Psi,\Psi$ formulation and b) the $\boldsymbol{A},\Psi$ formulation.

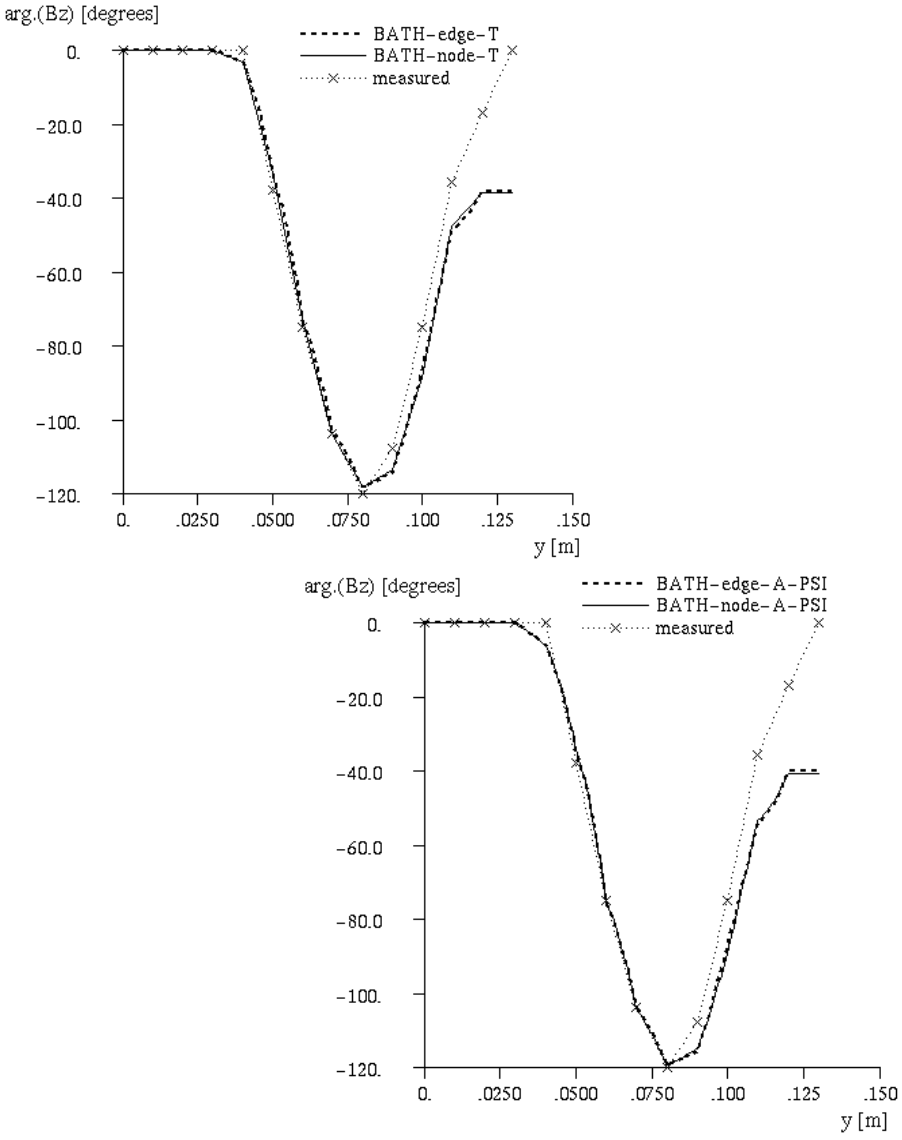

Figure 5.4 Measured and calculated argument of the z-component of the flux density along line A-B in the Bath Cube problem obtained by means of the hexahedral finite elements and a) the $\boldsymbol{T} - \Psi, \Psi$ formulation and b) the $\boldsymbol{A}, \Psi$ formulation.

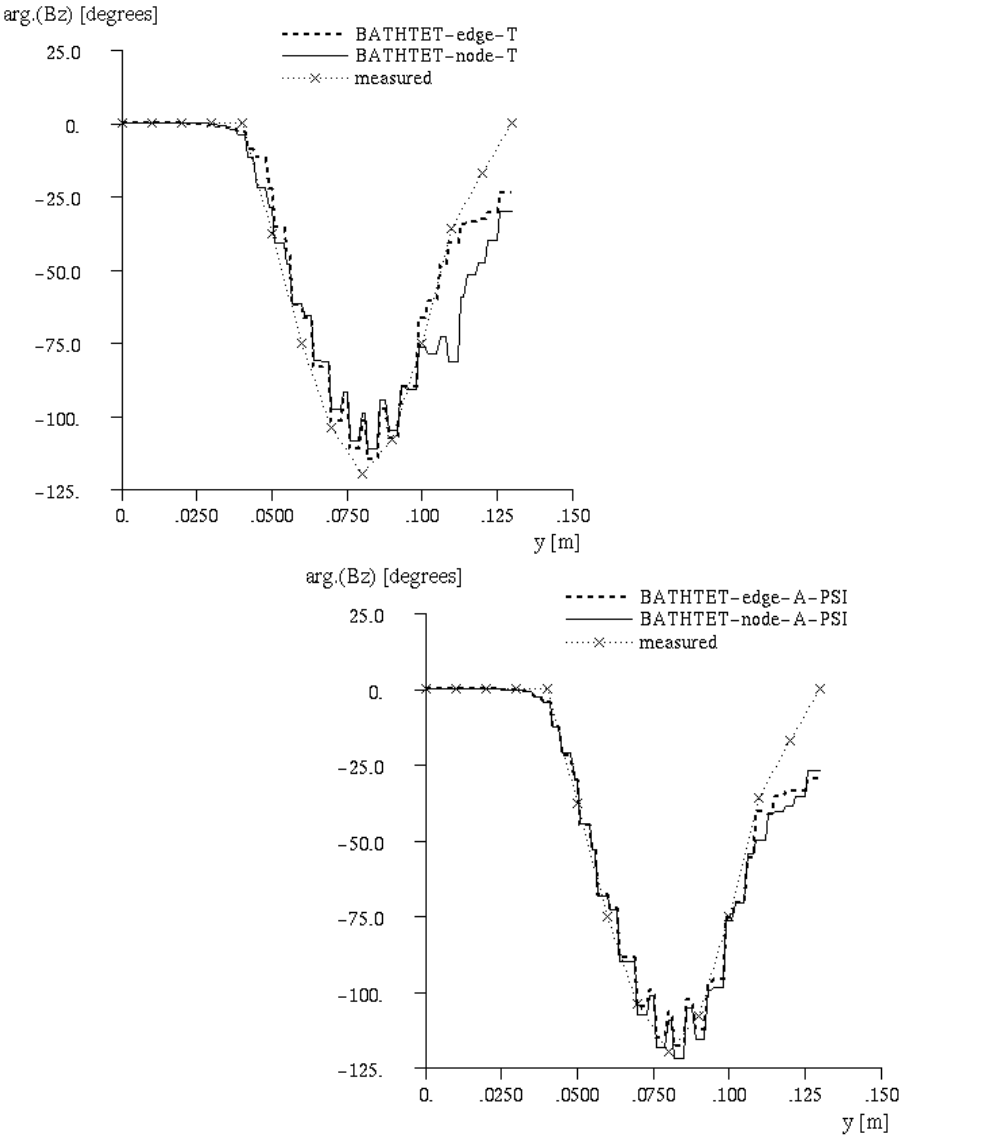

(a) (b)

Figure 5.5 Measured and calculated argument of the z-component of the flux density along line A-B in the Bath Cube problem obtained by means of the tetrahedral finite elements and a) the $\boldsymbol{T}-\Psi,\Psi$ formulation and b) the $\boldsymbol{A},\Psi$ formulation.

The flux density distributions obtained by the $\boldsymbol{T}-\Psi,\Psi$ and the $\boldsymbol{A},\Psi$ formulations in association with the hexahedral nodal and edge finite elements are in good agreement with each other. As far as the accuracy of the solution is concerned, both the $\boldsymbol{T}-\Psi,\Psi$ and the $\boldsymbol{A},\Psi$ formulations are considered to be suitable for the Bath Cube problem with the applied finite element mesh. Comparing the calculated results with the measurements, it is noticed that the agreement of the argument is not as good as the agreement of the modulus. Such behaviour is common in the results obtained in other publications, such as [105] and correspondence with these results is good. Table 5.2 presents the maximum error

between the measured and calculated results. The accuracy obtained by the $\boldsymbol{T}-\Psi, \Psi$ and the $\boldsymbol{A}, \Psi$ formulations is roughly the same.

Despite the figures of the maximum error presented in Table 5.2, the solution obtained by means of the tetrahedral elements is not as accurate as that obtained by means of the hexahedral elements for the major parts of the curves in Figs. 5.2 to 5.5, in spite of a larger number of unknowns for tetrahedra than for hexahedra. The calculated modulus and argument of the z-component of the flux density in Figs. 5.3 and 5.5 are discontinuous at the finite element boundaries. The loss of accuracy is due to the tetrahedral first-order nodal and low-order edge shape functions. The accuracy gain obtained from the increase in the number of unknowns is not sufficient to compensate for the poor quality of the tetrahedral shape functions.

Table 5.2 Maximum error between the measured and calculated results.

Formulations, finite elements	Modulus of the flux density [T]		Argument of the flux density [degrees]	
	Hexahedra	Tetrahedra	Hexahedra	Tetrahedra
$\boldsymbol{T}-\Psi, \Psi$, nodal elements	$1{\cdot}96\ 10^{-3}$	$2.02\ 10^{-3}$	38.71	45.58
$\boldsymbol{T}-\Psi, \Psi$, edge elements	$1{\cdot}96\ 10^{-3}$	$1{\cdot}84\ 10^{-3}$	38.24	23.93
$\boldsymbol{A}, \Psi$, nodal elements	$2{\cdot}10^{-3}$	$1.91{\cdot}10^{-3}$	40.72	27.03
$\boldsymbol{A}, \Psi$, edge elements	$2{\cdot}10^{-3}$	$1.93{\cdot}10^{-3}$	40.25	29.91

5.2.2 Use of the Computational Resources

The cost of the computations is determined by the required memory and the solution time. Tables 5.3 and 5.4 list some results of the solution of the problem obtained by means of the hexahedral and tetrahedral finite elements, respectively. The number of unknowns and the number of non-zero matrix elements are denoted by NEQNS and NZA, respectively. The $\boldsymbol{T}-\Psi, \Psi$ formulation yields less unknowns than the $\boldsymbol{A}, \Psi$ formulation.

It appears that, for a given mesh with hexahedral finite elements, the edge elements yield sparser matrices than nodal elements. In addition,the CPU time is considerably shorter for the edge elements.

Moreover, for a given mesh with tetrahedral finite elements, the edge finite elements are not favourable from the viewpoint of CPU time, number of unknowns, non-zeroes and iterations in comparison with nodal finite elements,

especially in combination with the $\boldsymbol{A}, \Psi$ formulation. This conclusion has also been reported by Nakata et al. [50].

Table 5.3 Some results of the solution of the problem obtained by means of the hexahedral finite elements.

Formulations, finite elements	NEQNS	NZA	Iterations	CPU-time [s]
$\boldsymbol{T}-\Psi, \Psi$, nodal elements	4 610	242 774	34	728
$\boldsymbol{T}-\Psi, \Psi$, edge elements	3 906	125 778	14	370
$\boldsymbol{A}, \Psi$, nodal elements	4 786	224 070	18	640
$\boldsymbol{A}, \Psi$, edge elements	4 970	185 340	15	477

Table 5.4 Some results of the solution of the problem obtained by means of the tetrahedral finite elements.

Formulations, finite elements	NEQNS	NZA	Iterations	CPU-time [s]
$\boldsymbol{T}-\Psi, \Psi$, nodal elements	8 490	180 922	25	965
$\boldsymbol{T}-\Psi, \Psi$, edge elements	9 764	204 540	144	1 406
$\boldsymbol{A}, \Psi$, nodal elements	8 730	174 054	20	890
$\boldsymbol{A}, \Psi$, edge elements	10 926	246 228	6 099	3 888

5.3 Asymmetrical Conductor with a Hole Problem

The Asymmetrical Conductor with a Hole problem [105] is illustrated in Fig. 5.6. A conducting plate with a conductivity of $3.526 \cdot 10^7$ Sm^{-1} is placed asymmetrically under a racetrack-shaped coil carrying a sinusoidal total current of 2742 A. The current density is constant over the cross-section of the coil. The frequency of the current is either 50 Hz or 200 Hz. The conducting plate has a square hole in one corner. A filling technique is used to make this multiply connected problem simply connected; the hole is filled with a material having a conductivity of 1/1000 that of the plate.

The Asymmetrical Conductor with a Hole problem is not symmetrical and the whole problem region is, therefore, discretized. In order to further investigate various formulations and finite element types, the problem is solved using two fine meshes. These meshes apply hexahedral and tetrahedral finite elements and are denoted by ASYM3 and ASYMTET, respectively. In addition, the Asymmetrical Conductor with a Hole problem is used to examine the rate of convergence of vector potential formulations in association with hexahedral nodal and edge elements. Therefore, two other finite element meshes, denoted by ASYM1 and

ASYM2, are used to solve the model. These meshes are less dense than ASYM3. Both the first-order nodal and low-order edge finite elements are used. The meshes are described in Table 5.5.

Since the conductivities of the conducting plate and the hole are different, the electric scalar potential is introduced in the conducting region, and the $\boldsymbol{A} - V, \Psi$ formulation is used. The discussion of the accuracy of the field solution is limited to the $\boldsymbol{T} - \Psi, \Psi$ and the $\boldsymbol{A} - V, \Psi$ formulations. Nodal basis functions are used to approximate the scalar potentials Ψ and V, whereas both nodal and edge basis functions are used to approximate the vector potentials $\boldsymbol{T}$ and $\boldsymbol{A}$.

When the $\boldsymbol{T} - \Psi, \Psi$ formulation is used, the boundary conditions (3.26) and (3.39) must be fulfilled.Equation (3.26) yields that the tangential components of $\boldsymbol{T}$ are set to zero on the boundaries of the conducting region. Equation (3.39) gives a Dirichlet boundary condition for Ψ on the top surface of the model.

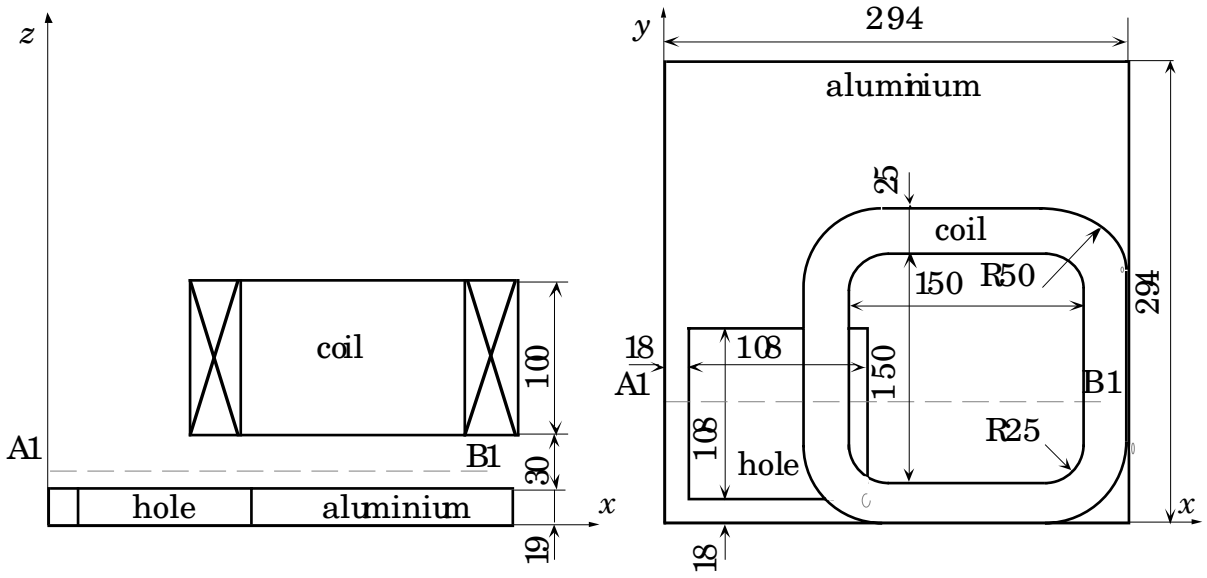

Figure 5.6 Geometry of the Asymmetrical Conductor with a Hole problem: a) front view, b) plan view. The dimensions are in millimeters.

Table 5.5 Finite element meshes used in the Asymmetrical Conductor with a Hole problem.

	ASYM1	ASYM2	ASYM3	ASYMTET
Number of nodes in the model	1 872	5 733	15 925	10 878
Number of nodes in the conducting region	192	867	2 883	1 683
Number of edges in the model	5 160	16 212	45 640	60 573
Number of edges in the conducting region	464	2 210	7 502	8 018

Number of finite elements	1 452	4 800	13 872	46 800

When the $\boldsymbol{A} - V, \Psi$ formulation is used, the boundary condition (3.39) must be fulfilled. In addition, when nodal basis functions are used to approximate $\boldsymbol{A}$, Eq. (3.29) must be satisfied yielding that the normal component of $\boldsymbol{A}$ is set to zero on the boundaries of the conducting region.

Furthermore, except for the top surface of the model, no flux is assumed to cross the model boundaries where a homogeneous Neumann boundary condition for Ψ is then applied.

The field $\boldsymbol{H}_{\mathrm{S}}$ is used to describe the magnetic field due to the coil in free space and is computed by the surface-source modeling method described in Chapter 4. In nodal elements, $\boldsymbol{H}_{\mathrm{S}}$ is computed at the nodes of the finite element mesh and approximated by means of the nodal basis functions. In edge elements, the line integrals of $\boldsymbol{H}_{\mathrm{S}}$ are computed along the edges of the finite element mesh and approximated by means of the edge basis functions.

5.3.1 Accuracy of the Field Solution

The Asymmetrical Conductor with a Hole problem is solved using ASYM3 and ASYMTET in order to investigate the vector potential formulations in association with hexahedral and tetrahedral, nodal and edge finite elements. The measured [109] and calculated z-component of the magnetic flux density along line A1-B1 (x from 0 to 288 mm, y = 72 mm, z = 34 mm) at 200 Hz are shown in Figs. 5.7 and 5.8.

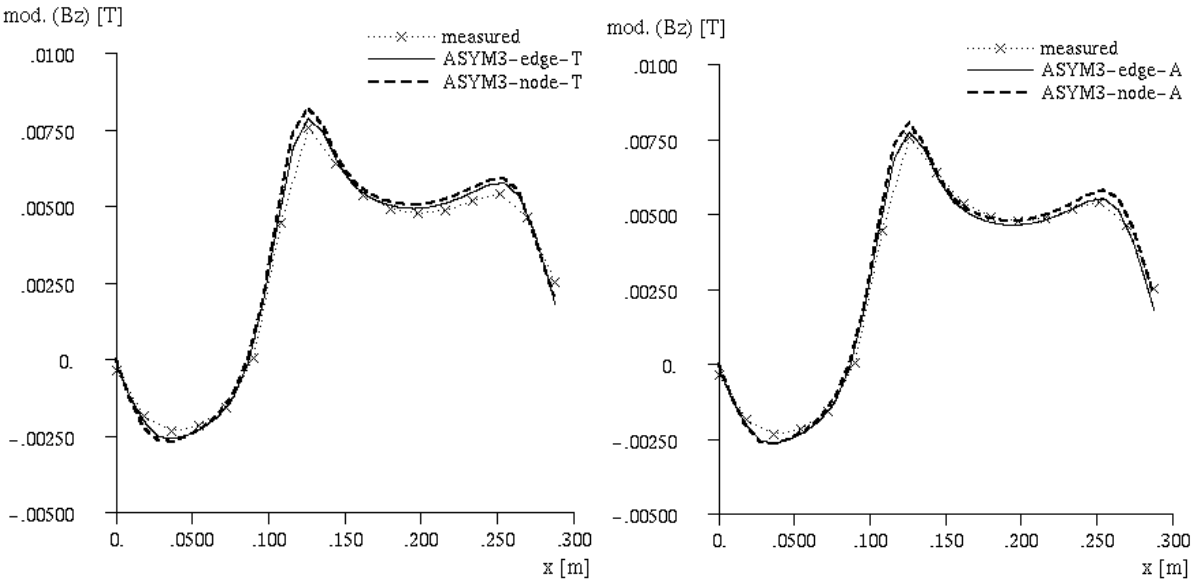

Figure 5.7 Measured and calculated z-component of the flux density along line A1-B1 in the Asymmetrical Conductor with a Hole problem obtained by means of the hexahedral finite elements and a) the $\boldsymbol{T}-\Psi,\Psi$ formulation and b) the $\boldsymbol{A}-V,\Psi$ formulation at 200 Hz.

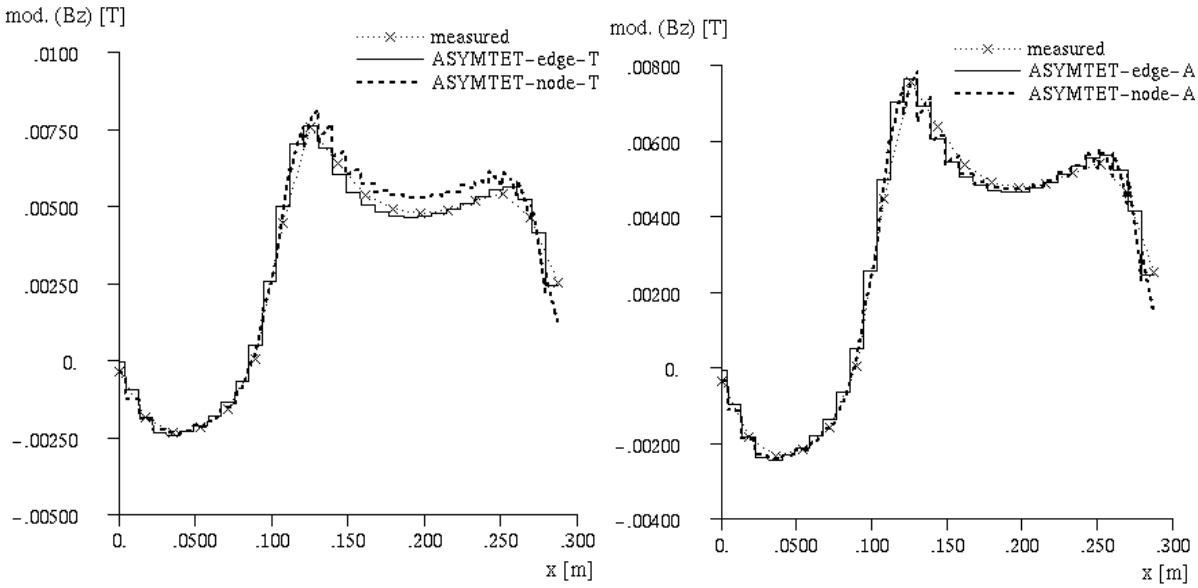

Figure 5.8 Measured and calculated z-component of the flux density along line A1-B1 in the Asymmetrical Conductor with a Hole problem obtained by means of the tetrahedral finite elements and a) the $\boldsymbol{T}-\Psi,\Psi$ formulation and b) the $\boldsymbol{A}-V,\Psi$ formulation at 200 Hz.

The flux density distributions obtained by the $\boldsymbol{T}-\Psi,\Psi$ and the $\boldsymbol{A}-V,\Psi$ formulations in association with the hexahedral nodal and edge finite elements are

in good agreement with each other. As far as the accuracy of the solution is concerned, both the $\boldsymbol{T} - \Psi, \Psi$ and the $\boldsymbol{A} - V, \Psi$ formulations are considered to be suitable for the Asymmetrical Conductor with a Hole problem with the applied finite element mesh. Comparing the calculated results with the measurements, it is noticed that the agreement of the magnetic flux density is good. The difference between the calculated and measured flux densities along line A1-B1 remains below $8.57 \cdot 10^{-4}$ T. As in the Bath Cube problem, the solution obtained by means of the tetrahedral elements is not as accurate as that obtained by means of the hexahedralelements.

The Asymmetrical Conductor with a Hole problem is solved using ASYM1 and ASYM2 in order to examine the rate of convergence of the vector potential formulations in association with hexahedral nodal and edge elements. The measured and calculated z-component of the magnetic flux density along line A1-B1 at both frequencies are shown in Figs. 5.9 to 5.12. Table 5.6 presents the maximum error between the measured and calculated results. The solution improves going from ASYM1 to ASYM2 and ASYM3. The maximum error in the magnetic flux density remains below $2.29 \cdot 10^{-3}$ T at both frequencies. Therefore, even if there is a certain error, the solution behaves the same way regardless of the frequency.

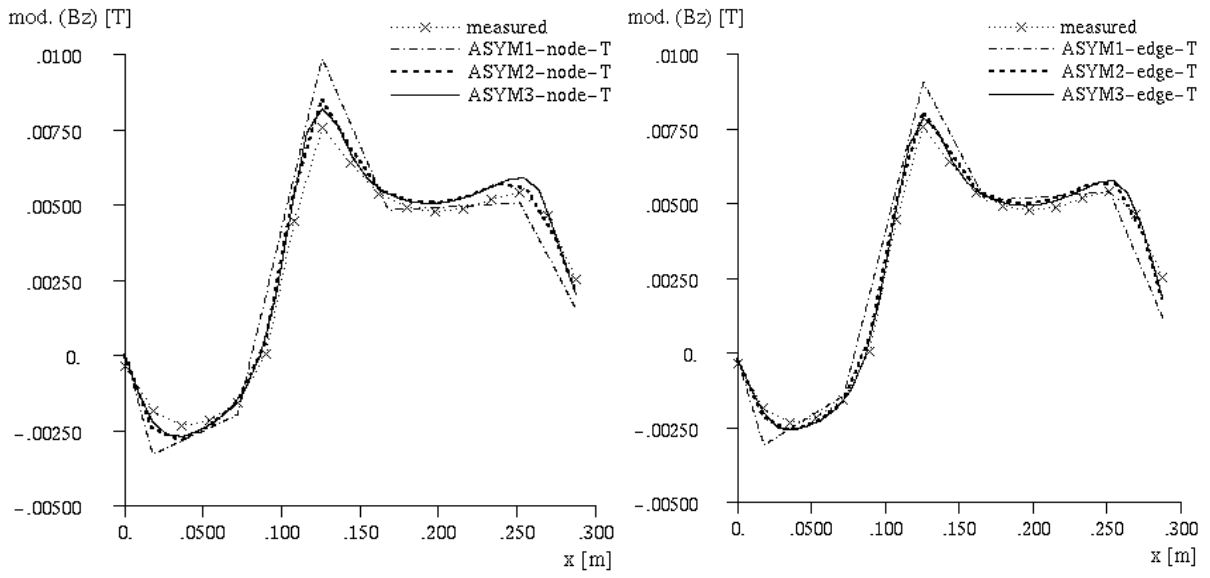

Figure 5.9 Measured and calculated z-component of the flux density along line A1-B1 in the Asymmetrical Conductor with a Hole problem obtained by the $\boldsymbol{T} - \Psi, \Psi$ formulation and hexahedral a) nodal elements and b) edge elements at 200 Hz.

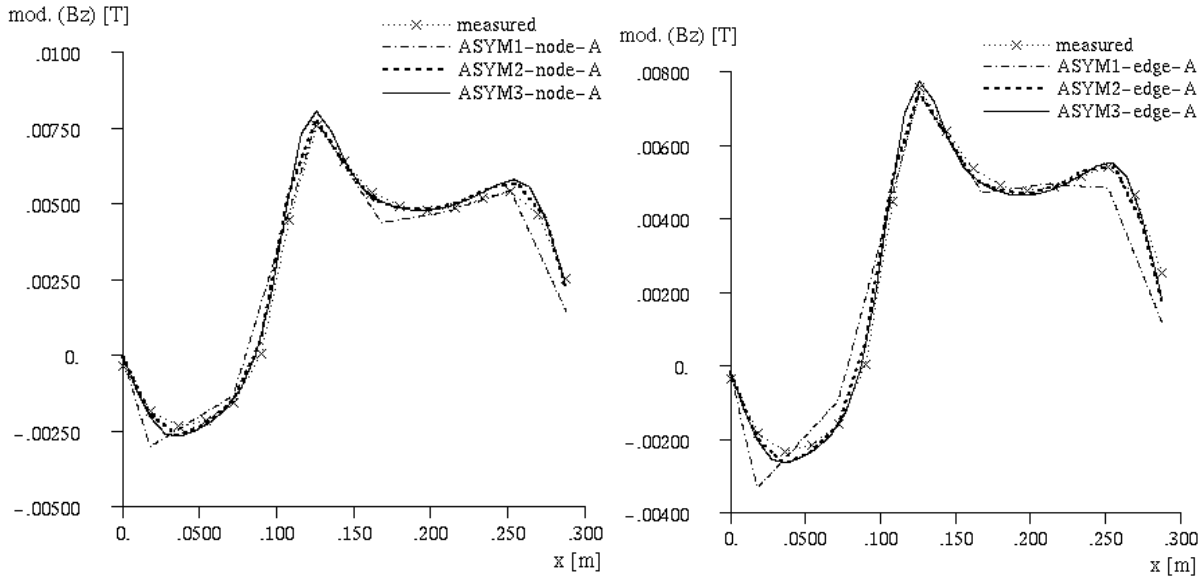

Figure 5.10 Measured and calculated z-component of the flux density along line A1-B1 in the Asymmetrical Conductor with a Hole problem obtained by the $\boldsymbol{A} - V, \Psi$ formulation and hexahedral a) nodal elements and b) edge elements at 200 Hz.

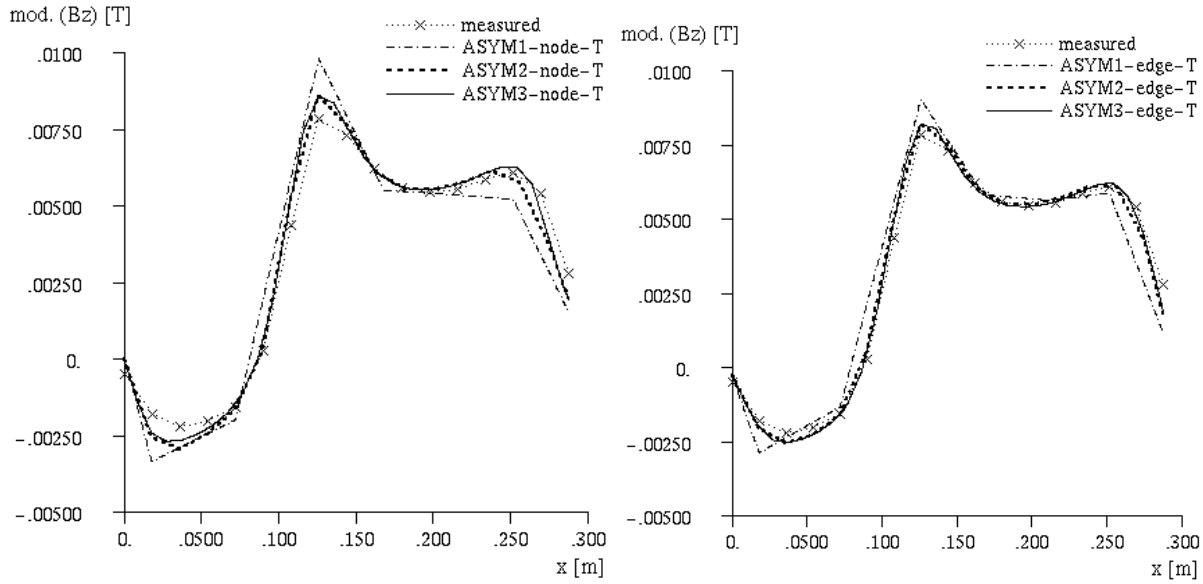

Figure 5.11 Measured and calculated z-component of the flux density along line A1-B1 in the Asymmetrical Conductor with a Hole problem obtained by the $\boldsymbol{T} - \Psi, \Psi$ formulation and hexahedral a) nodal elements and b) edge elements at 50 Hz.

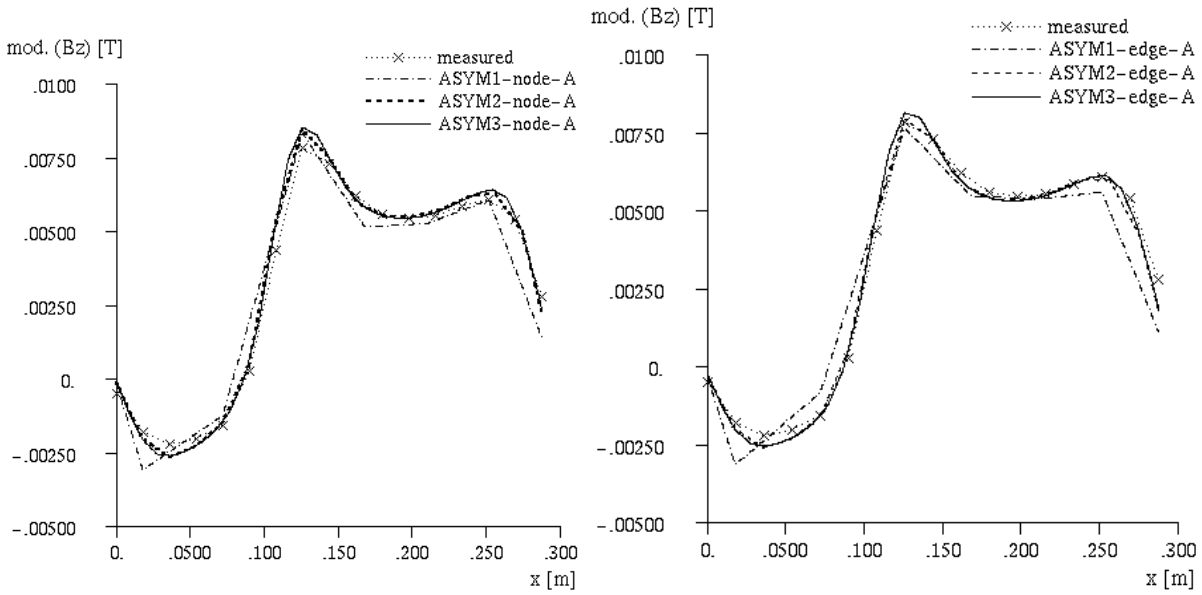

Figure 5.12 Measured and calculated z-component of the flux density along line A1-B1 in the Asymmetrical Conductor with a Hole problem obtained by the $\boldsymbol{A} - V, \Psi$ formulation and hexahedral a) nodal elements and b) edge elements at 50 Hz.

Table 5.6 Maximum error between the measured and calculated results obtained when the hexahedral finite elements are used.

Formulations, finite elements	Mesh	50 Hz	200 Hz
		Flux density [T]	Flux density [T]
$\boldsymbol{T} - \Psi, \Psi$, nodal elements	ASYM1	$2.03 \cdot 10^{-3}$	$2.29 \cdot 10^{-3}$
	ASYM2	$1.09 \cdot 10^{-3}$	$9.35 \cdot 10^{-4}$
	ASYM3	$8.48 \cdot 10^{-4}$	$7.82 \cdot 10^{-4}$
$\boldsymbol{T} - \Psi, \Psi$, edge elements	ASYM1	$1.89 \cdot 10^{-3}$	$2 \cdot 10^{-3}$
	ASYM2	$5.86 \cdot 10^{-4}$	$5.73 \cdot 10^{-4}$
	ASYM3	$5.06 \cdot 10^{-4}$	$4.93 \cdot 10^{-4}$
$\boldsymbol{A} - V, \Psi$, nodal elements	ASYM1	$1.7 \cdot 10^{-3}$	$1.62 \cdot 10^{-3}$
	ASYM2	$9.38 \cdot 10^{-4}$	$8.31 \cdot 10^{-4}$
	ASYM3	$8.57 \cdot 10^{-4}$	$7.69 \cdot 10^{-4}$
$\boldsymbol{A} - V, \Psi$, edge elements	ASYM1	$2.04 \cdot 10^{-3}$	$1.78 \cdot 10^{-3}$
	ASYM2	$6.46 \cdot 10^{-4}$	$5.56 \cdot 10^{-4}$
	ASYM3	$5.05 \cdot 10^{-4}$	$4.96 \cdot 10^{-4}$

5.3.2 Use of the Computational Resources

Tables 5.7 and 5.8 list some results of the solution of the problem obtained by means of the hexahedral and tetrahedral finite elements, respectively. The $\boldsymbol{T} - \Psi, \Psi$ formulation leads to a shorter CPU time as well as a smaller number of unknowns, non-zeroes and iterations than the $\boldsymbol{A} - V, \Psi$ formulation. It appears that, for a given mesh with hexahedral finite elements, the edge elements yield less unknowns and sparser matrices than nodal elements. As in the Bath Cube problem, the tetrahedral edge elements are not favourable from the viewpoint of CPU time, number of unknowns, non-zeroes and iterations in comparison with nodal finite elements, especially in combination with the $\boldsymbol{A} - V, \Psi$ formulation.

When the hexahedral finite elements are used, Figs. 5.13 to 5.16 present the maximum error in the flux density versus the storage required by the non-zeroes in the system matrix and versus the CPU-time at 200 Hz and 50 Hz. The maximum error in the flux density is calculated as

$$\frac{\max\left(B_{\text{calc}} - B_{\text{meas}}\right)}{\max\left(B_{\text{meas}}\right)} \tag{5.1}$$

where B_{calc} and B_{meas} are the calculated and measured magnetic flux densities, respectively. According to these curves, the hexahedral edge elements give more accurate results for a given discretization than nodal elements and allow for a reduction of the computer storage and the CPU time for a given accuracy. The differences between the $\boldsymbol{T} - \Psi, \Psi$ and the $\boldsymbol{A} - V, \Psi$ formulations are minor.

Table 5.7 Some results of the solution of the problem obtained by means of the hexahedral finite elements.

Formulations finite elements	Mesh	NEQNS	NZA	Iterations		CPU-time [s]	
				50 Hz	200 Hz	50 Hz	200 Hz
$\boldsymbol{T}-\Psi,\Psi$, nodal elem.	ASYM1	3 984	122 560	65	105	270	270
	ASYM2	13 218	501 748	113	113	3 218	3 361
	ASYM3	38 530	1 624 834	229	195	29 193	29 188
$\boldsymbol{T}-\Psi,\Psi$, edge elem.	ASYM1	3 768	100 080	21	28	388	388
	ASYM2	12 444	388 764	46	49	2 906	3 244
	ASYM3	36 244	1 230 668	85	81	22 463	22 308
$\boldsymbol{A}-V,\Psi$, nodal elem.	ASYM1	4 606	168 154	93	191	368	557
	ASYM2	15 784	709 066	533	154	5 235	4 937
	ASYM3	46 696	2 314 274	2 006	2 102	50 146	50 149
$\boldsymbol{A}-V,\Psi$, edge elem.	ASYM1	4 312	115 810	177	645	571	519
	ASYM2	14 554	444 254	537	781	3 601	3 812
	ASYM3	42 722	1 385 934	1 133	901	28 513	28 004

Table 5.8 Some results of the solution of the problem at 200 Hz obtained by means of the tetrahedral finite elements.

Formulations, finite elements	NEQNS	NZA	Iterations	CPU-time [s]
$\boldsymbol{T}-\Psi,\Psi$, nodal elements	25 428	461 782	140	6 051
$\boldsymbol{T}-\Psi,\Psi$, edge elements	27 836	508 282	470	8 387
$\boldsymbol{A}-V,\Psi$, nodal elements	30 298	659 576	1 850	10 863
$\boldsymbol{A}-V,\Psi$, edge elements	35 308	701 852	10 850	23 882

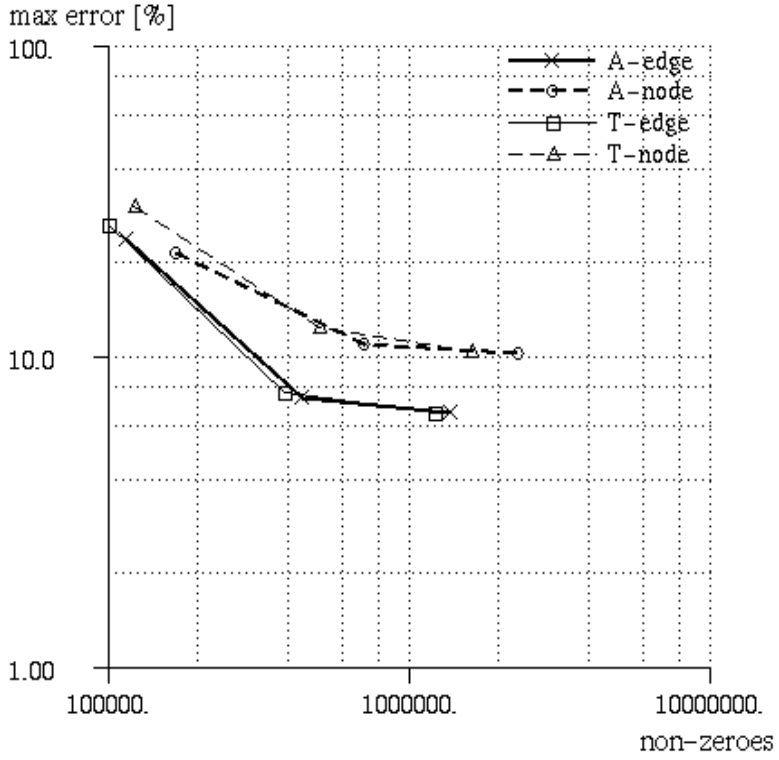

Figure 5.13 Maximum error in the flux density versus the number of non-zeroes in the system matrix at 200 Hz when the hexahedral finite elements are used.

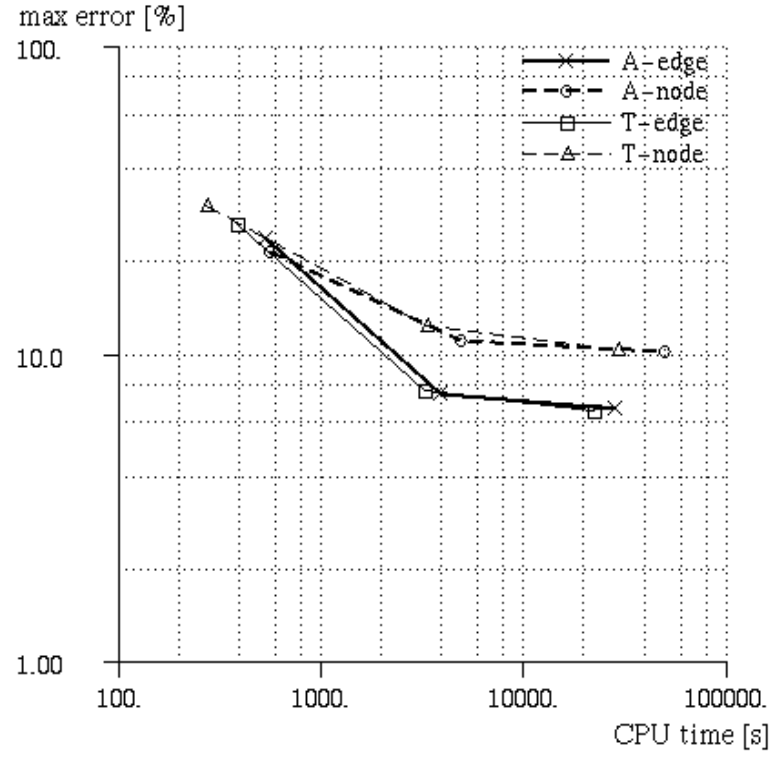

Figure 5.14 Maximum error in the flux density versus the CPU time at 200 Hz when the hexahedral finite elements are used.

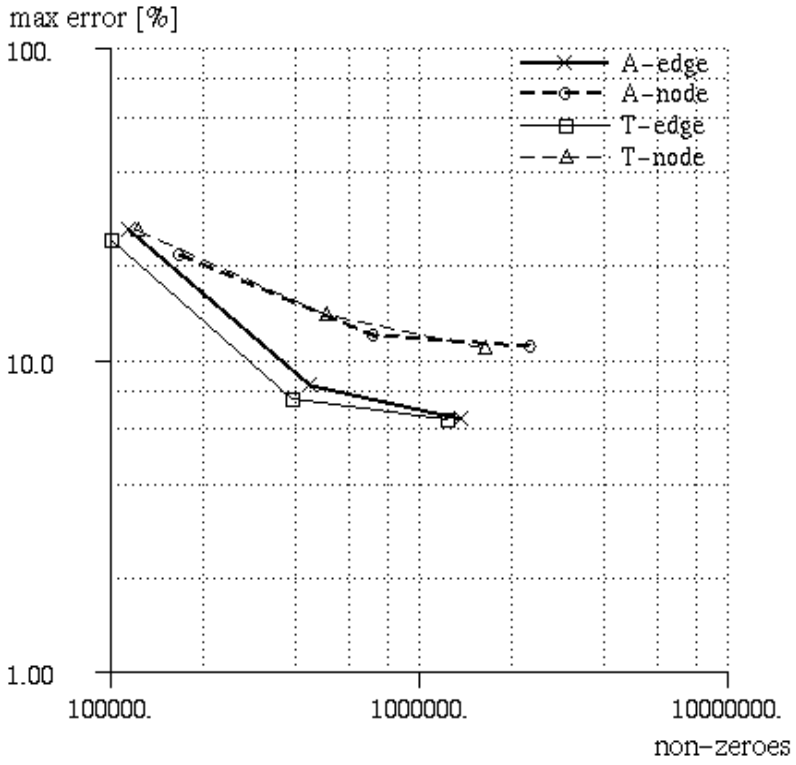

Figure 5.15 Maximum error in the flux density versus the number of non-zeroes in the system matrix at 50 Hz when the hexahedral finite elements are used.

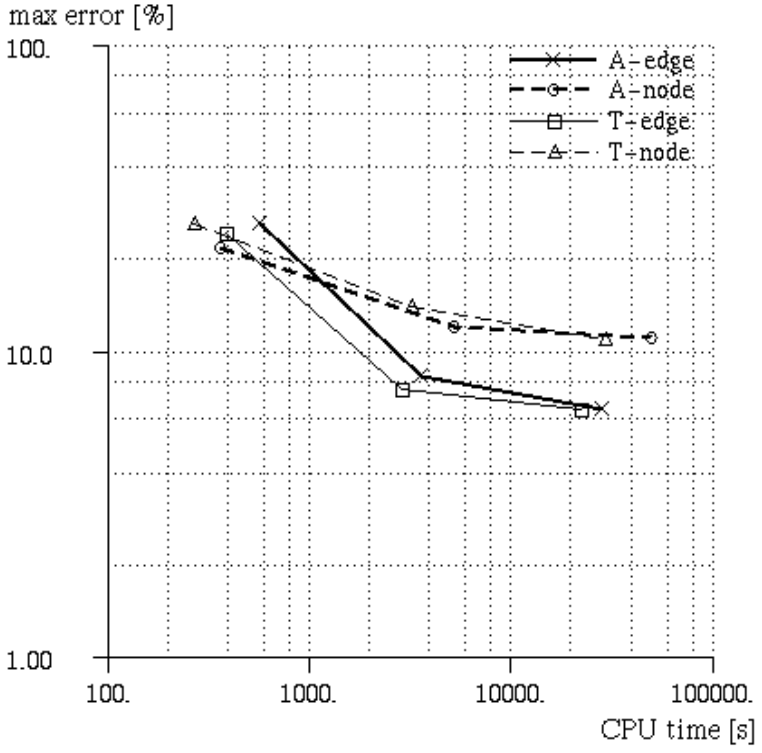

Figure 5.16 Maximum error in the flux density versus the CPU time at 50 Hz when the hexahedral finite elements are used.

5.4 Eddy-current Losses in Hydrogenerator End Region

5.4.1 Model of the Hydrogenerator

The 120 MVA hydrogenerator model studied is shown in Fig. 5.17; its dimensions are given in detail by Sande [44]. The stator model consists of a laminated iron core comprising four stacks, a tooth support finger, a clamping plate and three cooling ducts. The stacks of laminations are numbered from the end and into the stator so that stack No. 1 is the outermost stack. The rotor consists of a laminated pole with a solid-iron end part and a field winding. In the circumferential direction, the sector includes a slot and half a tooth. The machine is assumed to run at no load and, thus, only the field winding carries any current. The current density is assumed to be uniformly distributed over the cross-section of the field coils. The model of the field winding is located in such a way that the plane $z = 0$ and the plane $y = 0$ are symmetry planes.

Hexahedral first-order nodal and low-order edge finite elements are used for the solution. The finite element mesh is described in Table 5.9.

The field was solved by the $\boldsymbol{T} - \Psi, \Psi$, the $\boldsymbol{T} - \Omega, \Omega$ and the $\boldsymbol{A} - V, \Psi$ formulations. In the $\boldsymbol{T} - \Psi, \Psi$ and the $\boldsymbol{A} - V, \Psi$ formulations, the vector potentials are approximated by nodal or edge basis functions. On the other hand, in the $\boldsymbol{T} - \Omega, \Omega$ formulation, $\boldsymbol{T}$ is approximated only by nodal basis functions.

Material Properties

A laminated core in a synchronous machine implies that the permeability and the conductivity of the core are dependent on the direction of the field. Hence, the laminated core is anisotropic. The eddy currents induced in the core will only flow in a plane parallel to the laminations. In the hydrogenerator model, the laminations are parallel to the xy-plane, as are the eddy currents.

The anisotropy in the permeability of the laminated parts is modeled by a tensor, Eq. (3.46): the permeability has a low value in the z-direction. When the $\boldsymbol{T} - \Psi, \Psi$ or the $\boldsymbol{T} - \Omega, \Omega$ formulations are used, the anisotropy in the conductivity of the laminated core is modeled by setting the components of $\boldsymbol{T}$ tangential to the laminated sheets to zero for both finite element types, Eq. (3.45). When the $\boldsymbol{A} - V, \Psi$ formulation is used, the conductivity is represented by a tensor, Eq. (3.54): the conductivity is set to zero in the z-direction.

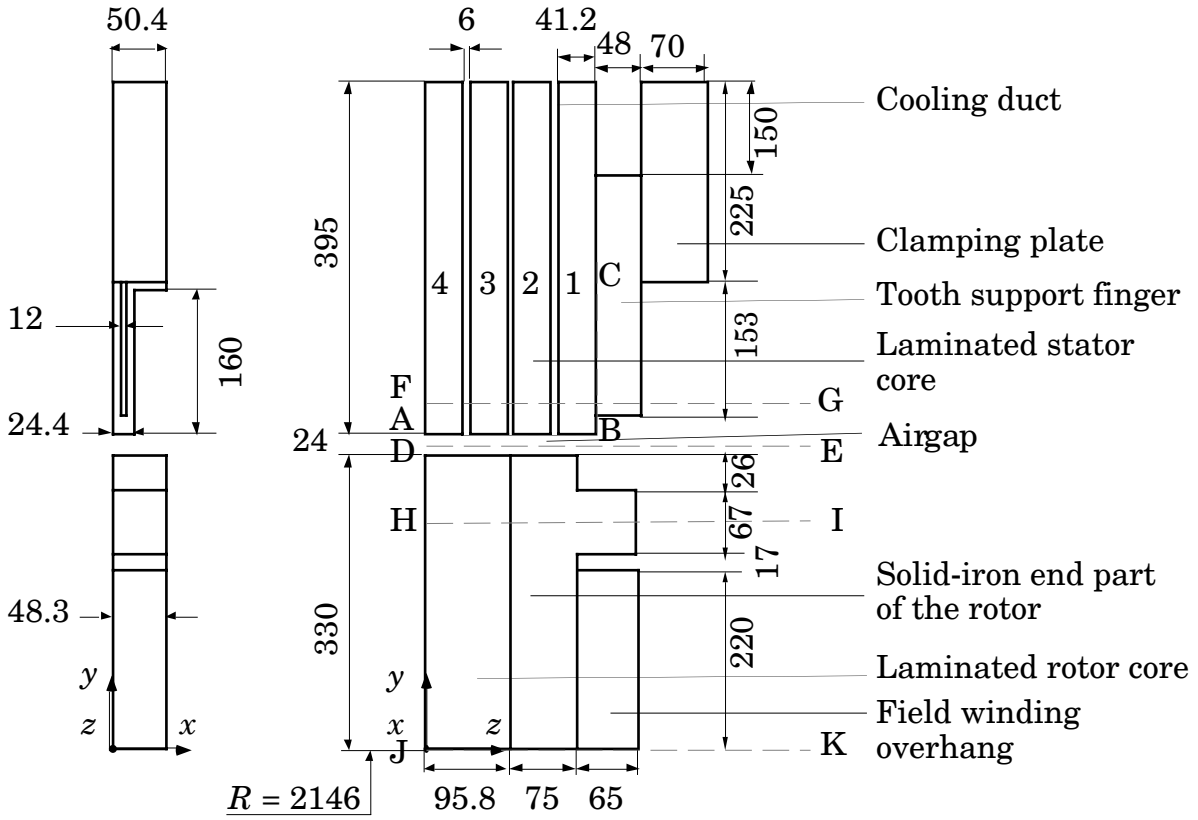

Figure 5.17 Geometry of the hydrogenerator model. The dimensions are in millimeters.

Table 5.9 Finite element mesh used in the hydrogenerator model.

Number of nodes in the model	30 550
Number of nodes in the conducting region	9 120
Number of nodes in the conducting region when the $\boldsymbol{T} - \Omega, \Omega$ formulation is used	17 110
Number of edges in the model	84 745
Number of edges in the conducting region	24 008
Number of finite elements	23 808

Since the rotor in a synchronous machine rotates with the same angular velocity as the air-gap field, no currents are induced in the rotor. The rotor is, therefore, included in the non-conducting region. The permeability and conductivity of the materials used in the model are given in Table 5.10 where μ_{rx}, μ_{ry} and μ_{rz} are the

relative permeabilities in the x-, y- and z-directions, respectively, and σ_x, σ_y and σ_z are the conductivities in the x-, y- and z-directions, respectively.

Table 5.10 Conductivities and relative permeabilities.

	μ_{rx}	μ_{ry}	μ_{rz}	σ_x [S/m]	σ_y [S/m]	σ_z [S/m]
Laminated stator core	465	465	13.9	$2.02\ 10^6$	$2.02\ 10^6$	0
Tooth support finger	3	3	3	$1.0\ 10^7$	$1.0\ 10^7$	$1.0\ 10^7$
Clamping plate	600	600	600	0	0	0
Solid end part of the rotor	600	600	600	0	0	0
Laminated rotor core	3 255	3 255	14.1	0	0	0

Boundary Conditions Using the $\boldsymbol{T-\Psi,\Psi}$ or the $\boldsymbol{T-\Omega,\Omega}$ Formulations

When the $\boldsymbol{T}-\Psi,\Psi$ or the $\boldsymbol{T}-\Omega,\Omega$ formulations are used, the boundary conditions (3.26) and (3.39) must be fulfilled. Equation (3.26) yields that the tangential components of $\boldsymbol{T}$ are set to zero on the boundaries of the conducting region to which the field is perpendicular and at the interface between conducting and non-conducting regions. Equation (3.39) gives a Dirichlet boundary condition for Ψ at the boundaries to which the field is perpendicular. On the boundaries to which the field is parallel, a homogeneous Neumann boundary condition for Ψ is applied, and T_n, the normal component of $\boldsymbol{T}$, is forced to zero in the case of approximating $\boldsymbol{T}$ by nodal basis functions. Figure 5.18 shows these boundary conditions.

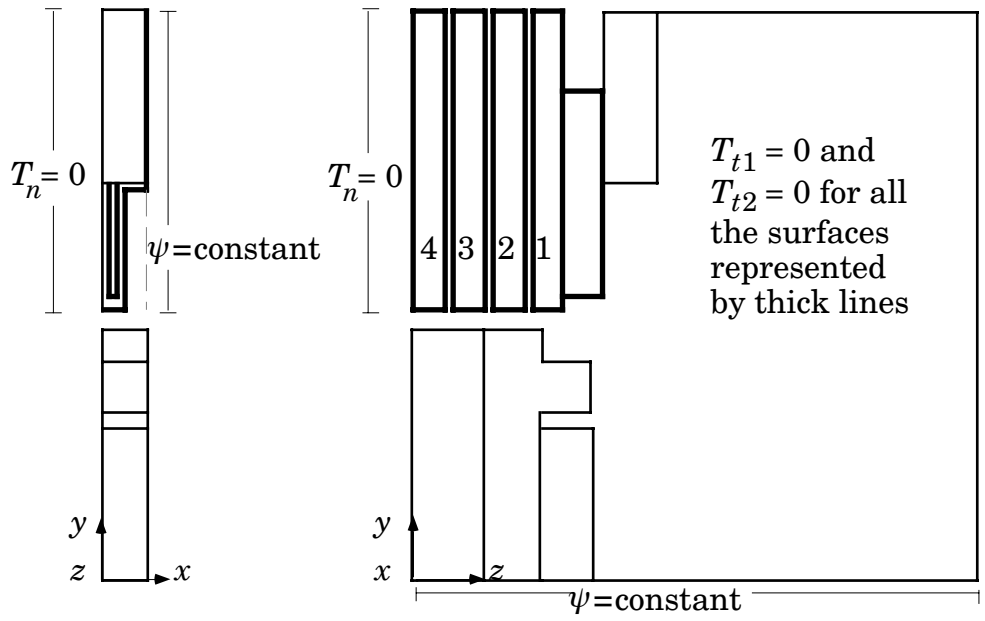

Figure 5.18 Boundary conditions of the hydrogenerator model when the $\boldsymbol{T}-\Psi,\Psi$ or the $T-\Omega,\Omega$ formulations are used.

Boundary Conditions Using the $\boldsymbol{A} - V, \Psi$ Formulation

When the $\boldsymbol{A} - V, \Psi$ formulation is used, the boundary conditions (3.27) and (3.39) must be fulfilled.Equation (3.27) yields that the tangential components of $\boldsymbol{A}$ are set to zero on the boundaries to which the field is parallel. In addition, when nodal basis functions are used to approximate $\boldsymbol{A}$, Eq. (3.29) must be satisfied yielding that the normal component of $\boldsymbol{A}$ is set to zero on the boundaries of the conducting region to which the field is perpendicular and at the interface between conducting and non-conducting regions. On the boundaries to which the field is parallel, a homogeneous Neumann boundary condition for Ψ is applied. Figure 5.19 shows these boundary conditions where A_{t1}, A_{t2} and A_n are the tangential and the normal components of $\boldsymbol{A}$, respectively.

Furthermore, V is fixed in at least one node of the conducting region assuring the uniqueness of V as mentioned in Section 3.4.

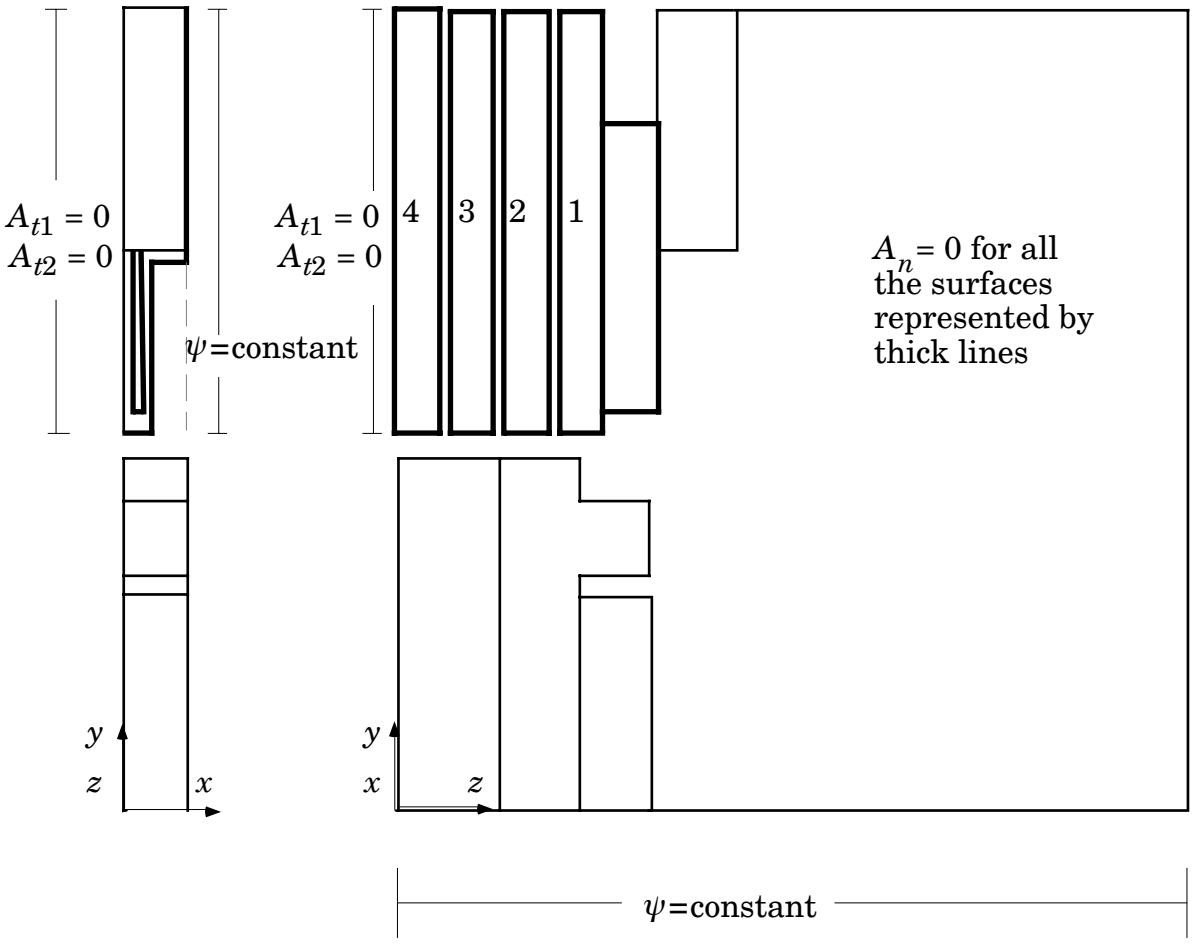

Figure 5.19 Boundary conditions of the hydrogenerator model when the $\boldsymbol{A} - V, \Psi$ formulation is used.

Modeling the Source Current

When the $\boldsymbol{T}-\Omega,\Omega$ formulation is used, the current density in the field winding is enforced by assuming that a low-conducting material is placed between the coil sides [34]. According to Eq. (3.12), $\boldsymbol{T}$ is then distributed uniformly in the low-conducting material and linearly in the current sources. The applied current density is $1.32\cdot10^6$ A/m^2, and the y-component of $\boldsymbol{T}$ varies from 0 to 85 682 A/m in the field winding

When the $\boxed{\boldsymbol{T}-\Psi,\Psi}$ or the $\boxed{\boldsymbol{A}-V,\Psi}$ formulations are used, the use of the reduced magnetic scalar potential Ψ in the non-conducting region comprising the current sources allows for the exclusion of these sources from the discretization by evaluating the free-space field $\boldsymbol{H}_\mathrm{s}$.

5.4.2 Results and Discussion

Comparing Two Ways of Modeling the Currents

Since the machine runs at no load and the field winding is of a simple shape, the calculation method based on decomposing a coil into finite volumes, such as straight segments and circular arcs, whose contributions to the field $\boldsymbol{H}_\mathrm{s}$ can be computed, is used and denoted here by UKM. The contribution from a circular arc segment with a rectangular cross-section and carrying azimuthal current density is evaluated in the same manner as presented by Urankar [91]. The integrals of the contribution from a straight segment are evaluated in the same way as proposed by Collie [90]. The UKM method, implemented by Keskinen [72], is compared with the surface-source modeling method denoted here by SSMM.

Figures 5.20 to 5.22 illustrate the Cartesian components of the field $\boldsymbol{H}_\mathrm{s}$ computed by UKM and SSMM along lines J-K and D-E defined in Fig. 5.17. The curves obtained coincide with each other. In addition, SSMM proves to be 43 % faster than UKM.

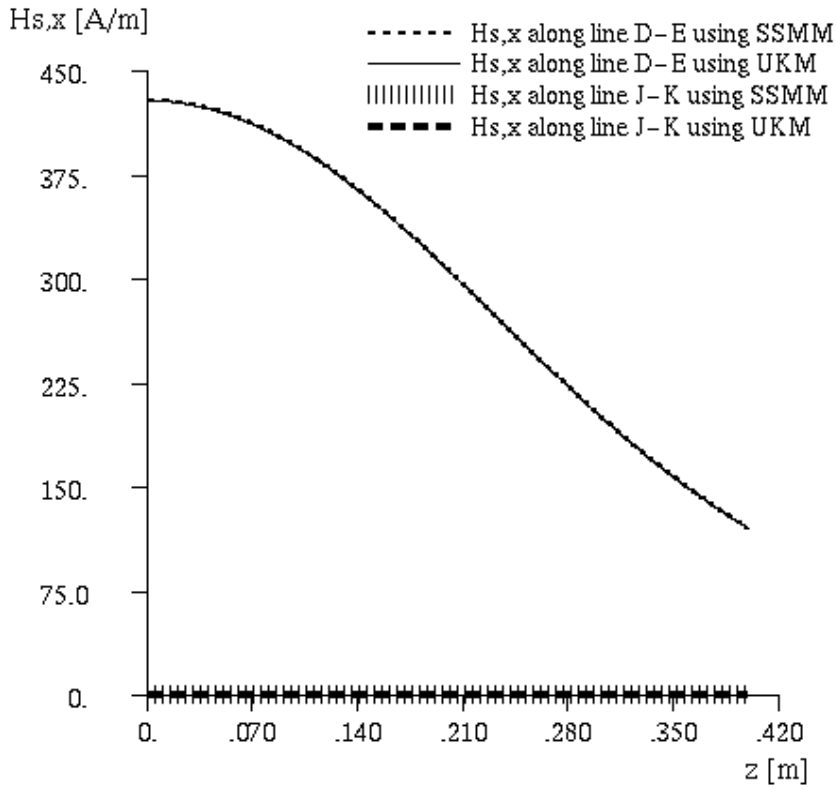

Figure 5.20 The x-component of the field $\boldsymbol{H}_{\mathrm{S}}$ along lines J-K and D-E obtained by UKM and SSMM.

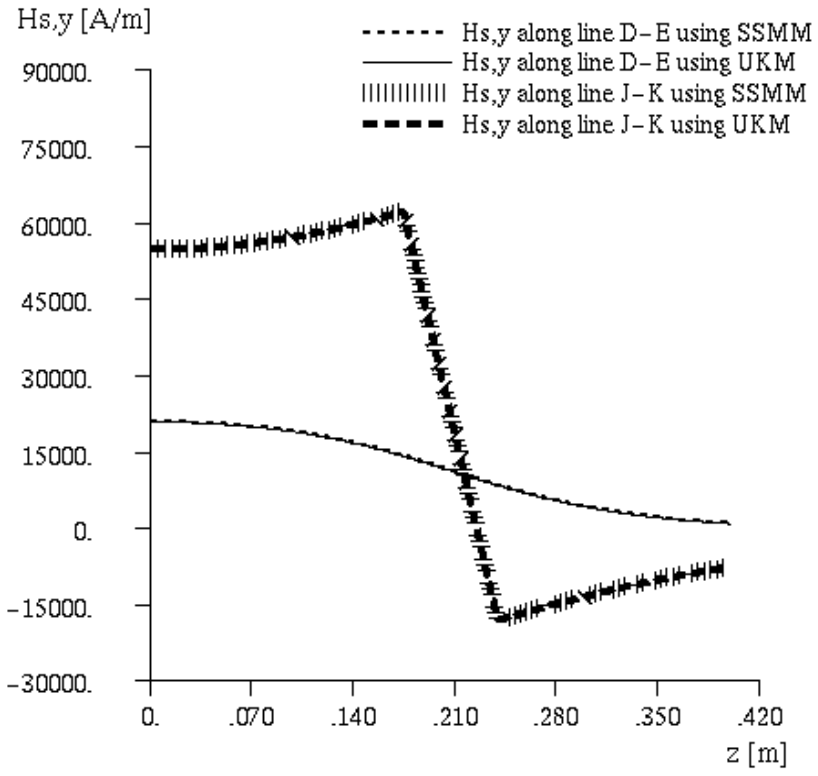

Figure 5.21 The y-component of the field $\boldsymbol{H}_{\mathrm{S}}$ along lines J-K and D-E obtained by UKM and SSMM.

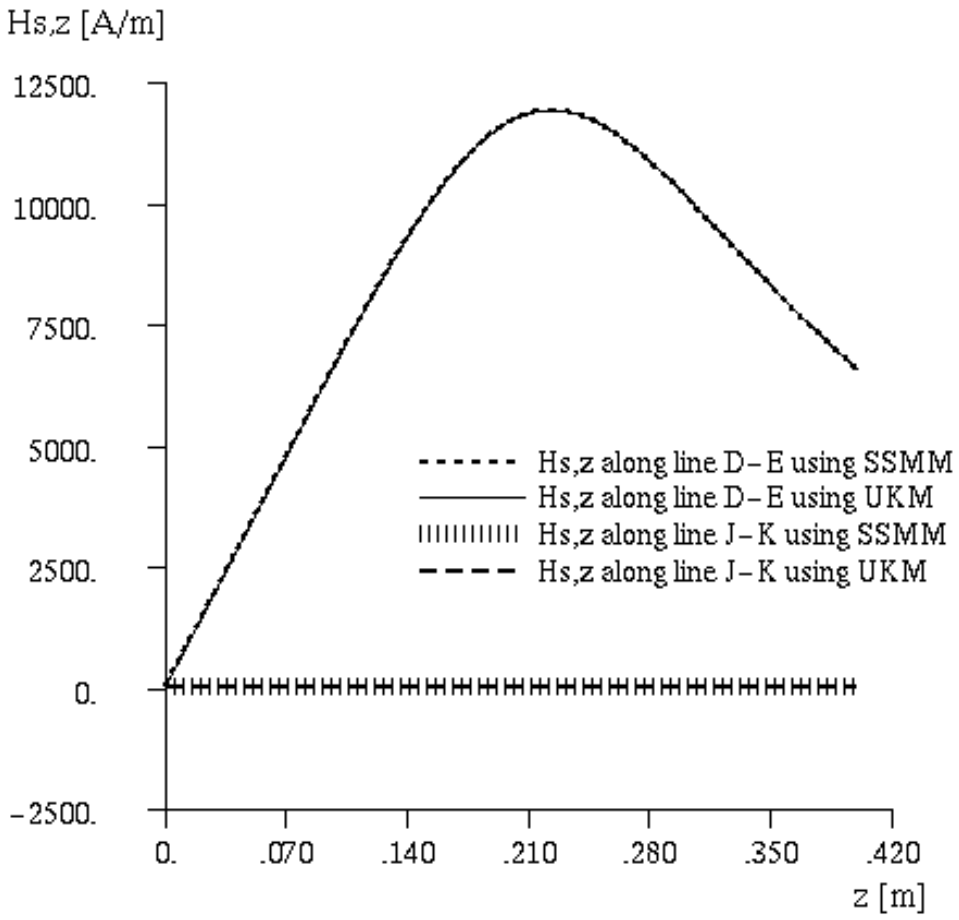

Figure 5.22 The z-component of the field $\boldsymbol{H}_S$ along lines J-K and D-E obtained by UKM and SSMM.

Use of the Computational Resources

Table 5.11 lists some results of the solution of the hydrogenerator model. For these computations, a SGI Origin 200 frontend computer with four 180 MHz MIPS R10000 CPUs with 1 GB RAM, to which many departments at the university are connected, was used. Because of the time sharing, it was not possible to compare the CPU times of different program runs.

Table 5.11 Some results of the solution of the hydrogenerator model.

Formulations, finite elements	NEQNS	NZA	Iterations
$\boldsymbol{T}-\Psi,\Psi$, nodal elements	69 998	2 397 296	332
$\boldsymbol{T}-\Psi,\Psi$, edge elements	82 542	2 221 412	224
$\boldsymbol{A}-V,\Psi$, nodal elements	97 004	4 946 170	2 921
$\boldsymbol{A}-V,\Psi$, edge elements	84 510	3 105 928	1 339
$\boldsymbol{T}-\Omega,\Omega$, nodal elements	69 998	1 630 161	765

Comparison with Published Results

The solution obtained by the $\boldsymbol{T}-\Omega,\Omega$ formulation is compared with that obtained by Sande [44]. This comparison is achieved by having the same formulation, geometry and material data as Sande, but not the same finite element mesh. Sande had, for instance, no nodes in the last two cooling ducts, which is not the case in this study. Figures 5.23 and 5.24 show the calculated magnetic flux density and the flux density obtained by Sande along lines A-B and B-C. The curves correspond well to each other. The discrepancies are mainly due to the different finite element meshes used.

Figure 5.23 Flux density along line A-B in the hydrogenerator model.

Figure 5.24 Flux density along line B-C in the hydrogenerator model.

Field Solution

The field solutions of the model obtained by the $\boldsymbol{T}-\Psi,\Psi$, the $\boldsymbol{T}-\Omega,\Omega$ and the $\boldsymbol{A}-V,\Psi$ formulations are illustrated in Figs. 5.25, 5.26 and 5.27. These figures show the y-component, i.e., the radial component, of the flux density along line F-G in the stator tooth, D-E in the air gap and H-I in the pole body, respectively. The results obtained by the different formulations and finite elements are in good agreement with each other. The flux density in the end region of the outermost stack is locally high since the magnetic saturation of iron is not taken into account. In addition, the $\boldsymbol{T}-\Omega,\Omega$ formulation gives slightly higher values for the air-gap flux density. In the case of the $\boldsymbol{T}-\Psi,\Psi$ formulation with nodal elements, cancellation problems in the rotor core have occurred, resulting in violent field variations as illustrated in Fig. 5.27. In high-permeability regions, a numerical error in the reduced magnetic scalar potential of 3 % has caused an error of 136.8 % in the magnetic flux density. As expected, the combination of the reduced magnetic scalar potential and the nodal element representation of $\boldsymbol{H}_{\mathrm{s}}$ cannot be recommended for regions with a high permeability.

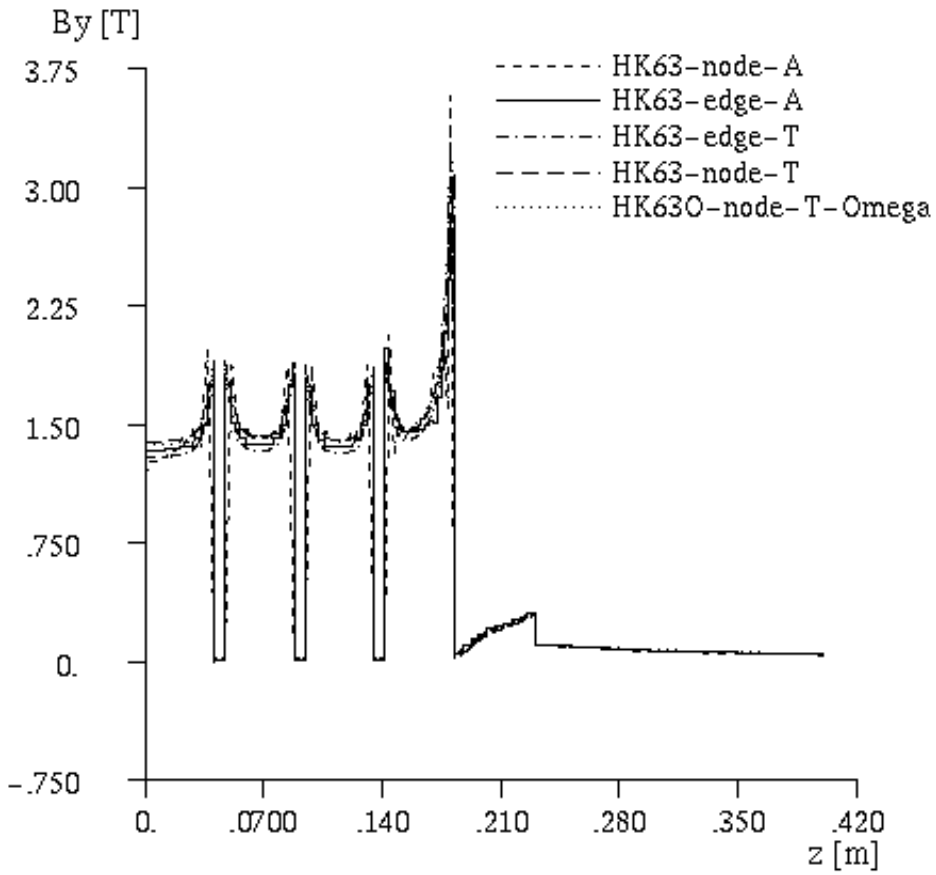

Figure 5.25 The y-component of the flux density along line F-G in the stator tooth of the hydrogenerator model.

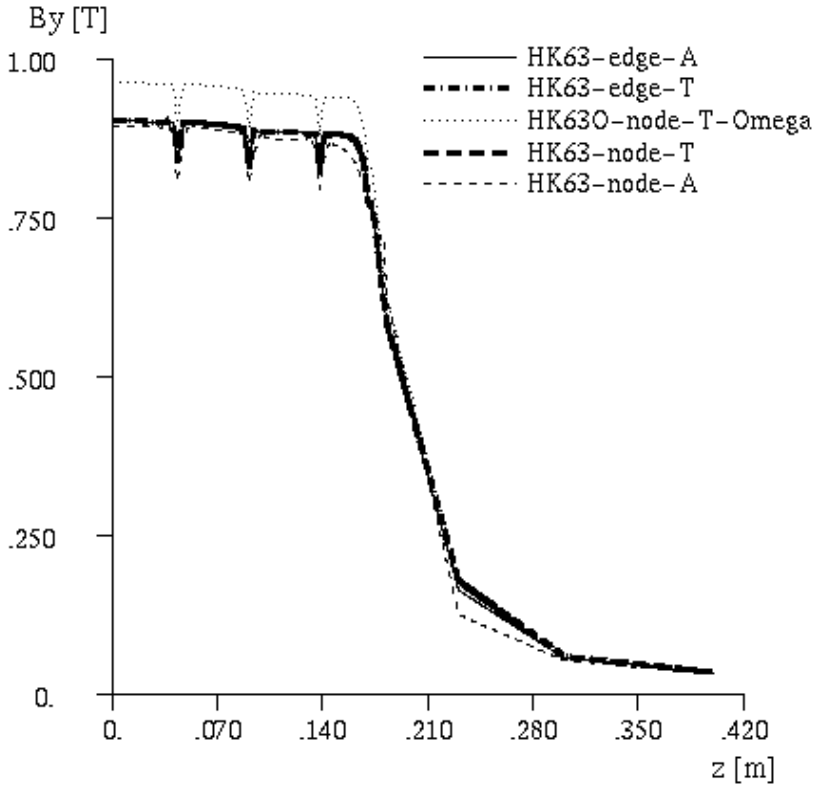

Figure 5.26 The *y*-component of the flux density along line D-E in the air gap of the hydrogenerator model.

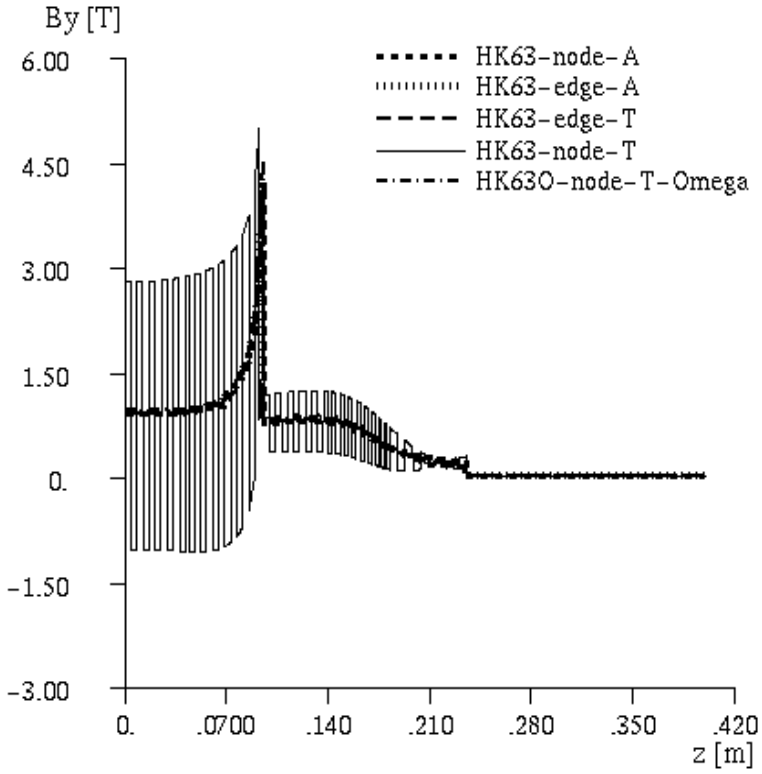

Figure 5.27 The y-component of the flux density along line H-I in the pole body of the hydrogenerator model.

Eddy-current Losses

The air-gap fringing effect and end-winding currents cause leakage fields in the end regions of electrical machines. The time variation of the end field induces eddy currents in the conducting parts of the supporting structure. Furthermore, eddy currents are induced in the laminated core as the magnetic field impinges on the core axially.

The eddy-current density distribution on the surface of the lamination stacks and the tooth support finger is shown as a filled contour plot in Fig. 5.28. The eddy-current density is, as expected, concentrated to the lower part of the tooth support finger and the outermost stack. The eddy-current losses in a conducting part with volume V' are given by

$$P = \int_{V'} \frac{1}{\sigma} |J|^2 \, dV' \tag{5.2}$$

where J is the rms value of the current density. Table 5.12 shows the eddy-current losses in the different parts of the model. The losses obtained by the different formulations agree well with each other.

Figure 5.28 Eddy-current density distribution on the surface of the lamination stacks and the tooth support finger of the hydrogenerator model.

Table 5.12 Eddy-current losses in the stator stacks and the tooth support finger.

Formulations, finite elements	Finger losses [W]	Stack 1 losses [W]	Stack 2 losses [W]	Stack 3 Losses [W]	Stack 4 losses [W]
$\boldsymbol{T}-\Psi,\Psi$, nodal elements	24.1	35.1	0.9	0.8	0.5
$\boldsymbol{T}-\Psi,\Psi$, edge elements	23.1	33.3	0.9	0.8	0.4
$\boldsymbol{A}-V,\Psi$, nodal elements	23.9	34.2	0.8	0.8	0.5
$\boldsymbol{A}-V,\Psi$, edge elements	23.0	32.8	0.8	0.7	0.3
$\boldsymbol{T}-\Omega,\Omega$, nodal elements	24.7	27.3	0.7	0.5	0.3

5.5 Eddy-current Losses in Turbogenerator End Region

5.5.1 Model of the Turbogenerator

The 635 MVA, 21.5 kV two-pole turbogenerator model studied is shown in Fig. 5.29. The stator model consists of cooling ducts and a laminated iron core comprising seventeen stacks. The stacks of laminations are numbered from the end and into the stator so that stack No. 1 is the outermost stack. The rotor consists of a solid-iron core and a field winding.In the circumferential direction, the sector includes half a slot pitch. The machine is studied under both no-load and load conditions. The machine shaft is not included in the model.

Hexahedral first-order nodal and low-order edge finite elements are used for the solution. Only one element layer is used in the cooling ducts. The finite element mesh is described in Table 5.13.

Cancellation problems occurred in the hydrogenerator model when the $\boldsymbol{T}-\Psi,\Psi$ formulation in conjunction with nodal elements was used. Therefore, the $\boldsymbol{T}-\Psi,\Psi$ formulation in association with edge elements was chosen to solve the field in the turbogenerator model. In addition, since the conductivity of the turbogenerator model is homogeneous, the $\boldsymbol{A},\Psi$ formulation has been used, instead of the $\boldsymbol{A}-V,\Psi$ formulation. The vector potential $\boldsymbol{A}$ is approximated by nodal basis functions.

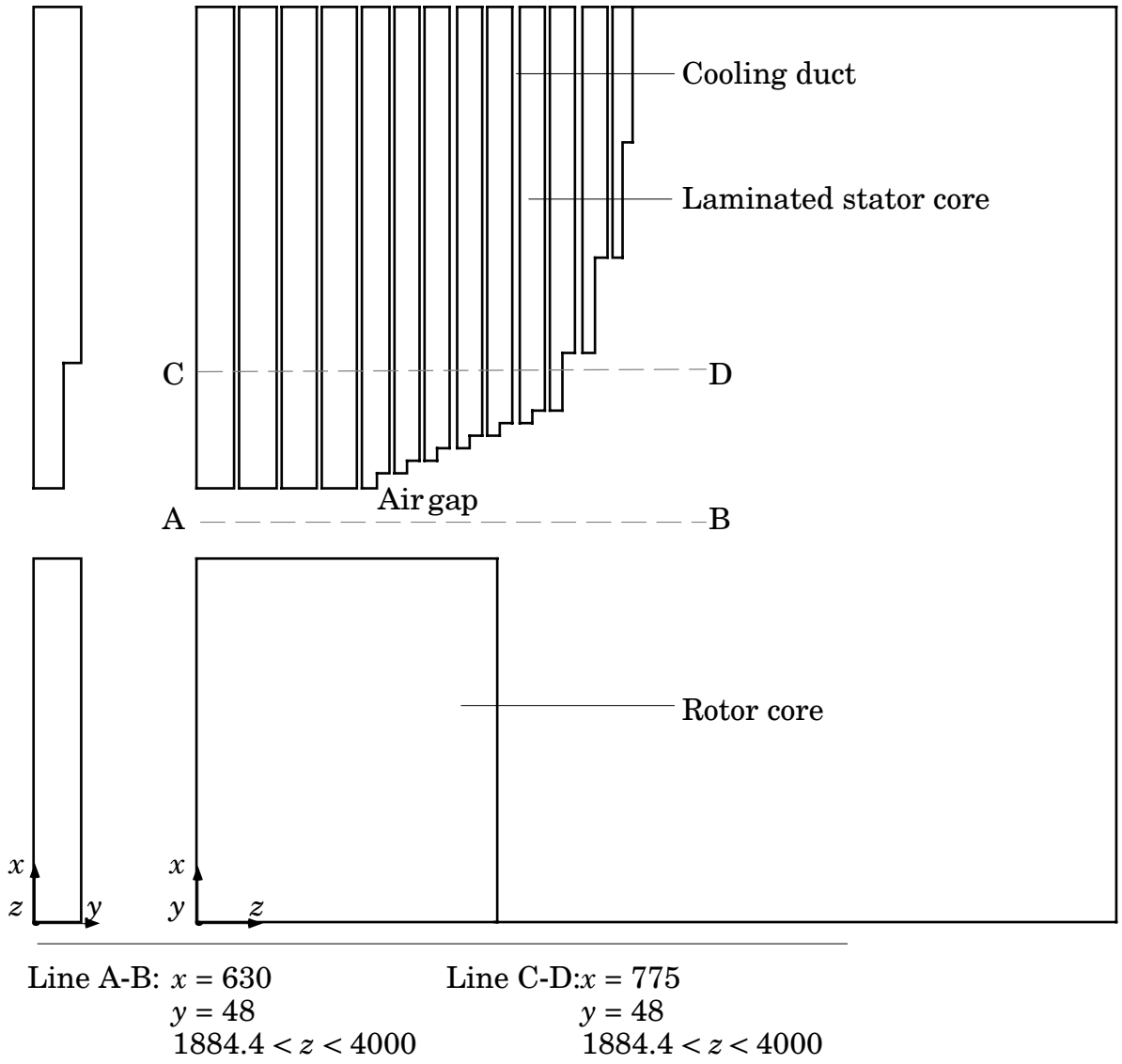

Figure 5.29 Geometry of the turbogenerator model. The dimensions are in millimeters.

Table 5.13 Finite element mesh used in the turbogenerator model.

Number of nodes in the model	43 776
Number of nodes in the conducting region	4 987
Number of edges in the model	119 444
Number of edges in the conducting region	12 358
Number of finite elements	32 130

Assuming that the air-gap magnetic field is an alternating field, the boundary conditions imposed on the model are artificial. The material properties, the modeling of the stator laminations and the boundary conditions are equal to those applied in the hydrogenerator model presented in Section 5.4.1.

Modeling the Source Current

The geometry of the machine windings is described in detail in Section 4.1. The current densities are assumed to be uniformly distributed over the cross-sections of the coils. The free-space field $\boldsymbol{H}_s$, due to each coil of the stator and field windings, is computed by the surface-source modeling method. The resultant field $\boldsymbol{H}_s$ is, then, evaluated by vectorially adding up the contributions from all the coils.

The stator and field currents used in the finite element solution under both no-load and load conditions are discussed and given in Section 4.4. At load, the machine is overexcited and operates with a power factor of 0.85 at rated voltage and current.

Using Eq. (4.22), the load angle is evaluated to 41.6 °. Then, the angle α given by Eq. (4.30) is 163.4 °, and the angle $\gamma - \beta$ in Eq. (4.32) is 41.74 °, where α, γ and β are illustrated in Fig. 4.7. Assuming that β is zero, the magnetic axis of phase A coincides with the x-axis and the angle γ is 41.74 °. The current densities have been computed using Eq. (4.28) and are given in Table 5.14 where J_a, J_b and J_c are the current densities in the stator winding, and J_f is the current density in the field winding. Figure 5.30 illustrates the position of the d-axis with respect to the x-axis.

Table 5.14 Applied current densities in the stator and field windings under both no-load and load conditions.

		no-load condition	load condition
Re $\{J_a\}$ [A/m^2]	top half-coil	0	–4 689 961
	bottom half-coil	0	–5 268 690
Im $\{J_a\}$ [A/m^2]	top half-coil	0	0
	bottom half-coil	0	0
Re $\{J_b\}$ [A/m^2]	top half-coil	0	–4 241 621
	bottom half-coil	0	–4 765 027
Im $\{J_b\}$ [A/m^2]	top half-coil	0	0
	bottom half-coil	0	0
Re $\{J_c\}$ [A/m^2]	top half-coil	0	8 931 582
	bottom half-coil	0	10 033 716
Im $\{J_c\}$ [A/m^2]	top half-coil	0	0
	bottom half-coil	0	0
J_f [A/m^2]	normal coil	3 221 834	12 226 860
	pole coil	3 228 219	12 251 091

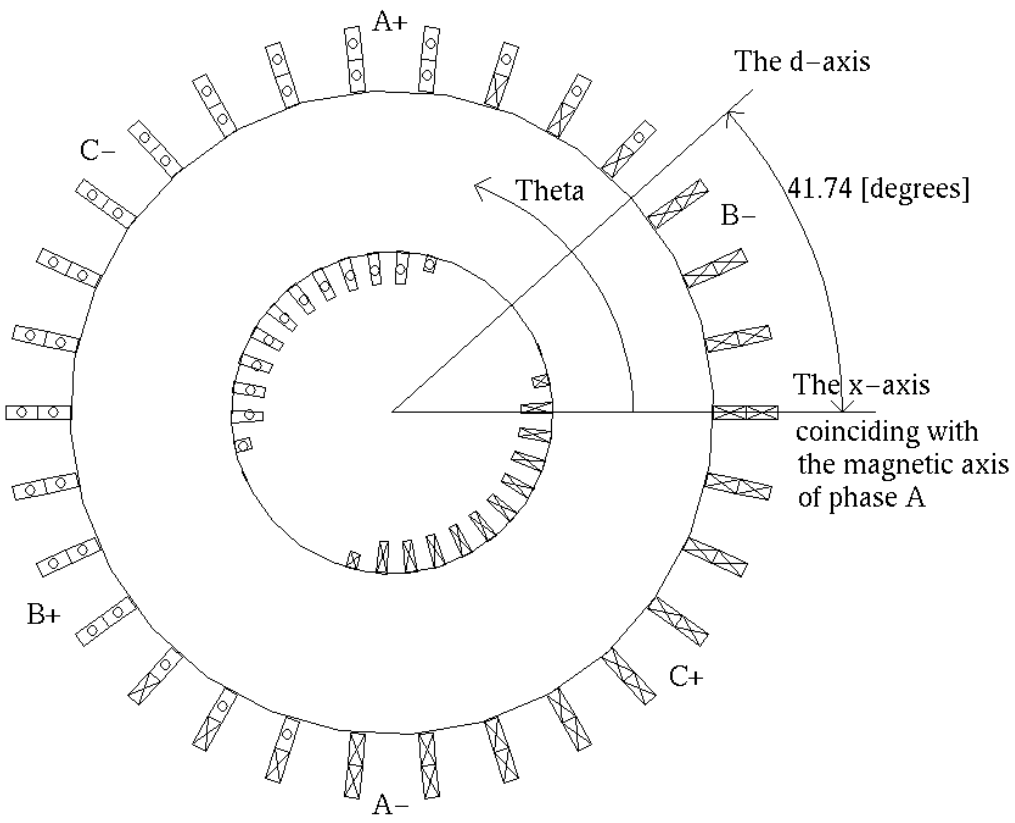

Figure 5.30 Position of the d-axis with respect to the x-axis.

5.5.2 Results and Discussion

The Free-space Field

At load and in the air gap, the radial components of the contributions to the resultant free-space field $\boldsymbol{H}_S$, due to the field windingalone and the stator winding alone, as well as the radial component of the resultant field $\boldsymbol{H}_S$, due to both windings, are illustrated in Fig. 5.31, where θ is defined in Fig. 5.30. Since the d-axis lies at 41.74 ° with respect to the x-axis, the maximum of the fundamental wave of the field $\boldsymbol{H}_S$ due to the field winding occurs at this angle. Similarly, since the magnetomotive force of the stator lies at –121.66 ° with respect to the x-axis, the maximum of the fundamental wave of the field $\boldsymbol{H}_S$ due to the stator windingoccurs at this angle. In accordance with the discussion presented in Section 4.4, the maximum of the fundamental wave of the resultant field $\boldsymbol{H}_S$ occurs at 0 ° where the discretized model lies. Some harmonics observed in the curves of Fig. 5.31 cause the maxima of the curves not to lie at exactly the above mentioned angles.

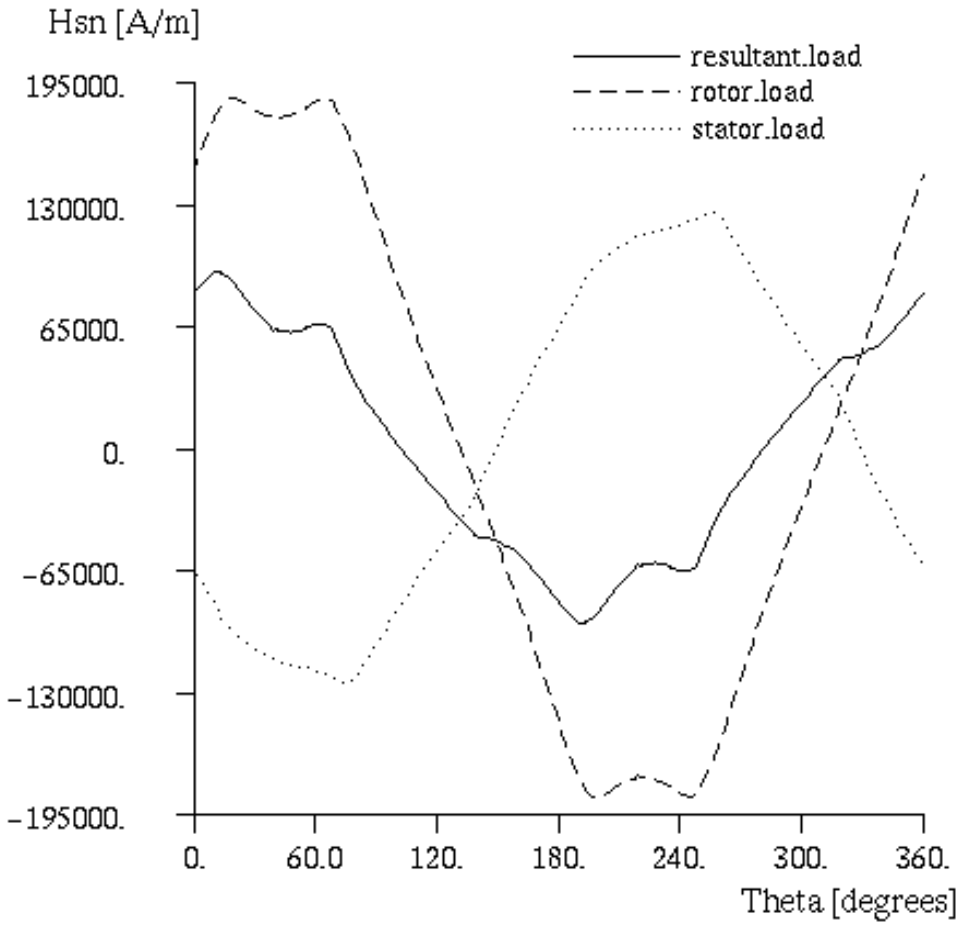

Figure 5.31 Radial components of the contributions to the resultant free-space field $\boldsymbol{H}_S$, due to the field winding alone and the stator winding alone, as well as the radial component of the resultant field $\boldsymbol{H}_S$, due to both windings, in the air gap.

Use of the Computational Resources

Table 5.15 lists some results of the solution of the turbogenerator model. For these computations, a CRAY Origin 2000 backend computer with sixty four 195 MHz MIPS R10000 CPUs with 9.5 GB RAM, to which many departments at the university are connected, was used. Because of the time sharing, it was not possible to compare the CPU times of different program runs.

Table 5.15 Some results of the solution of the turbogenerator model.

Formulations, finite elements	NEQNS	NZA	Iterations no load / load
$\boldsymbol{T}-\Psi, \Psi$, edge elements	89 394	2 273 622	242 / 255
$\boldsymbol{A}, \Psi$, nodal elements	94 126	2 616 102	641 / 587

Field Solution of the Turbogenerator Model at No Load

The field solutions of the model at no load obtained by the $\boldsymbol{T}-\Psi,\Psi$ and the $\boldsymbol{A},\Psi$ formulations are illustrated in Figs. 5.32 and 5.33. These figures show the x-component, i.e., the radial component, of the flux density along line C-D in the stator tooth and line A-B in the air gap, respectively. The results obtained by the two formulations and finite elements are in good agreement with each other. The flux density in the end region, from the first to the eighth lamination stack, is locally high since the magnetic saturation of iron is not taken into account.

The eddy-current density distribution at no load on the surface of the lamination stacks is shown as a filled contour plot in Fig. 5.34. The eddy-current density is concentrated to the lower part of the stator end region. The eddy-current losses in the model obtained by the $\boldsymbol{T}-\Psi,\Psi$ and the $\boldsymbol{A},\Psi$ formulations are 152 W and 153 W, respectively.

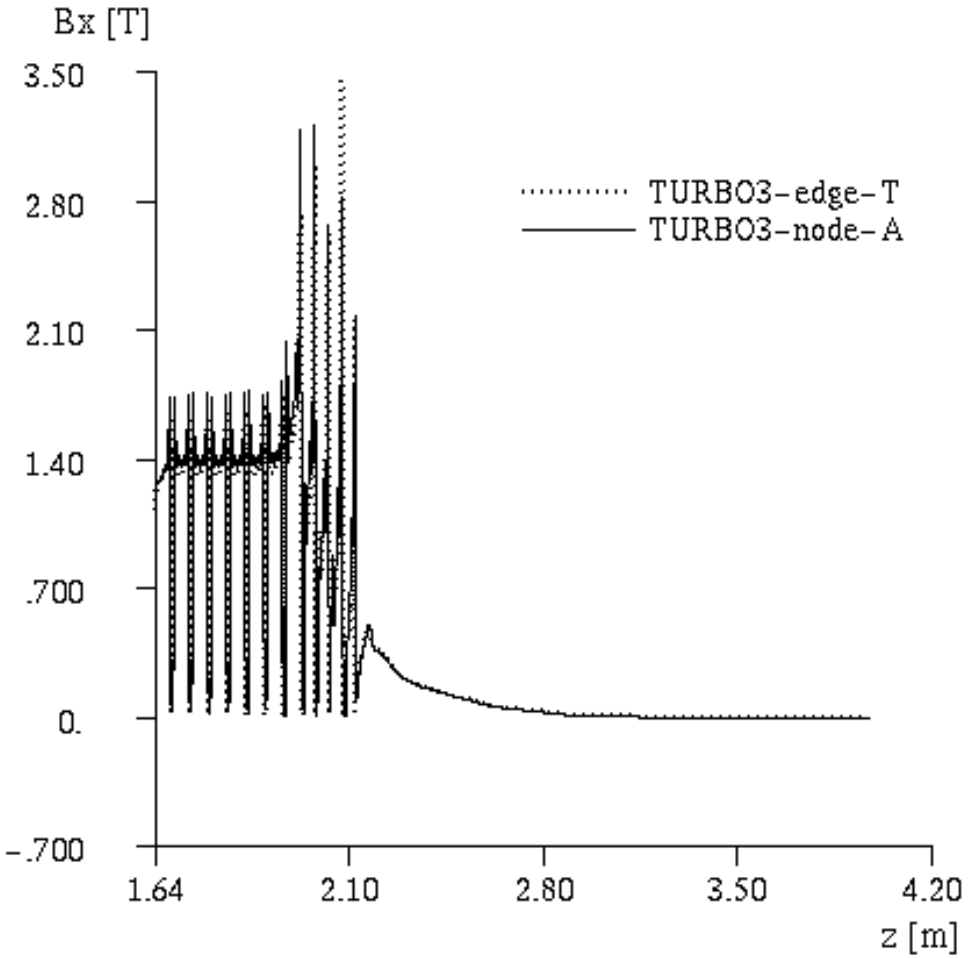

Figure 5.32 The x-component of the flux density along line C-D in the stator tooth of the turbogenerator model at no load.

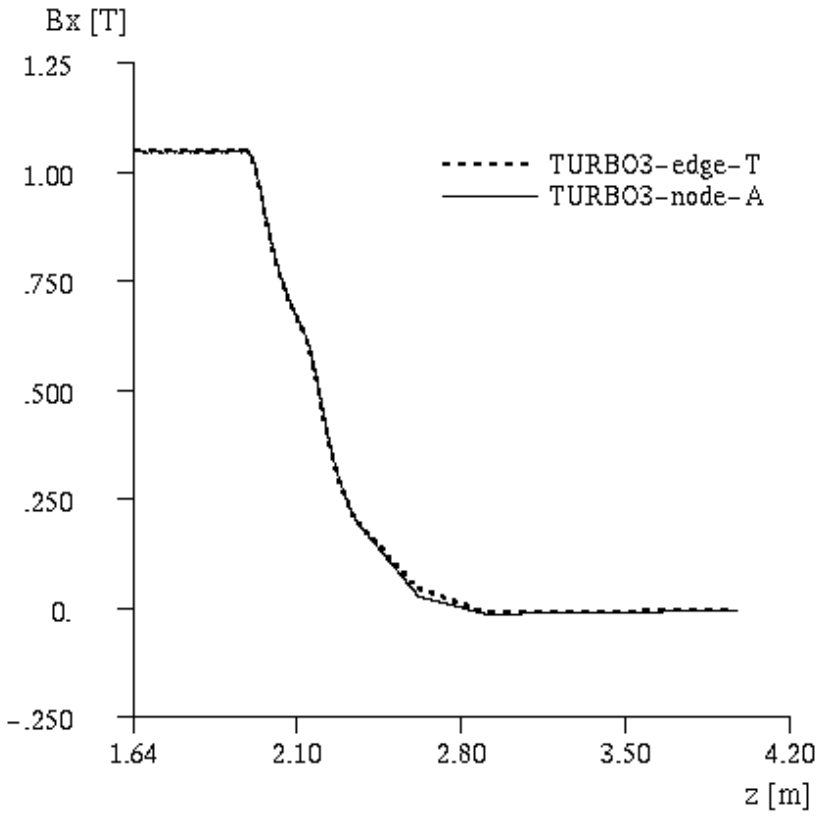

Figure 5.33 The x-component of the flux density along line A-B in the air gap of the turbogenerator model at no load.

Figure 5.34 Eddy-current density distribution on the surface of the lamination stacks of the turbogenerator model at no load.

Field Solution of the Turbogenerator Model at Load

The field solutions of the model at load obtained by the $\boldsymbol{T}-\Psi,\Psi$ and the $\boldsymbol{A},\Psi$ formulations are illustrated in Figs. 5.35 and 5.36. These figures show the x-component of the flux density along line C-D in the stator tooth and line A-B in the air gap, respectively. The results obtained by the two formulations and finite elements are in good agreement with each other.

The eddy-current density distribution at load on the surface of the lamination stacks is shown as a filled contour plot in Fig. 5.37. The eddy-current losses in the model obtained by the $\boldsymbol{T}-\Psi,\Psi$ and the $\boldsymbol{A},\Psi$ formulations are 289 W and 290 W, respectively. In the end region, the calculated eddy-current losses at load are

almost twice those at no load, because of the extra losses due to the axial component of the leakage fields caused by the stator end-winding currents.

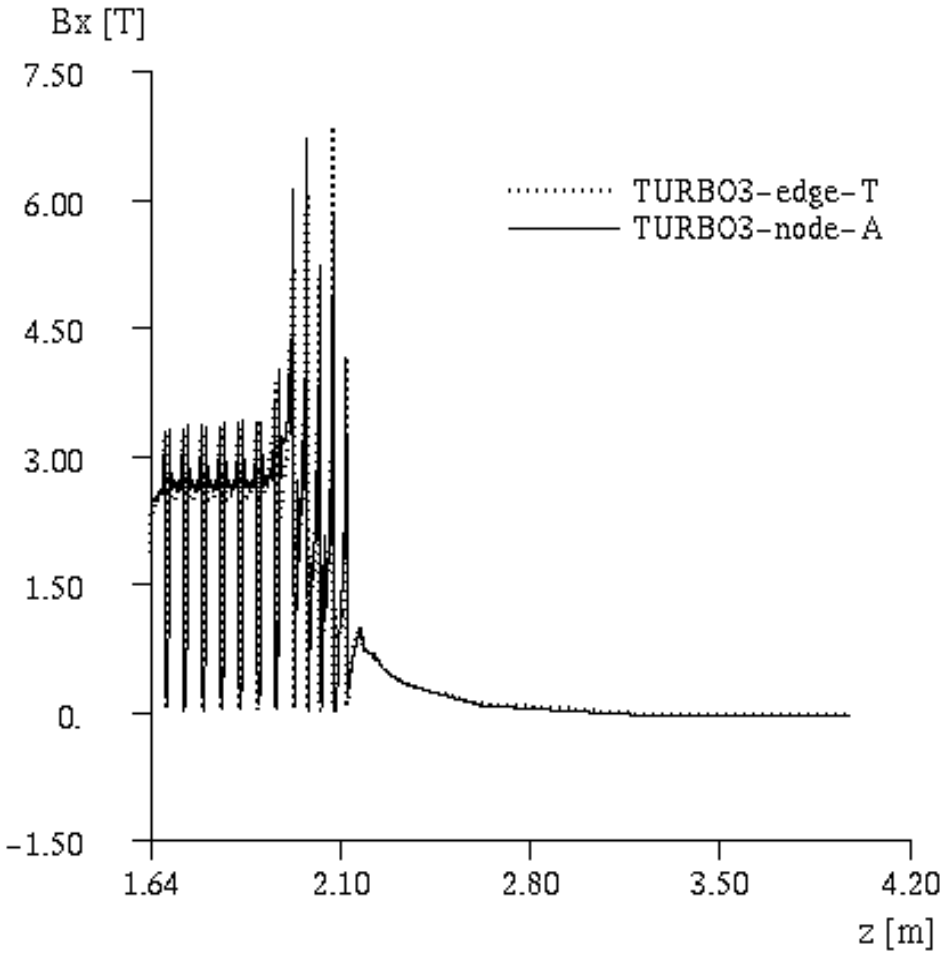

Figure 5.35 The x-component of the flux density along line C-D in the stator tooth of the turbogenerator model at load.

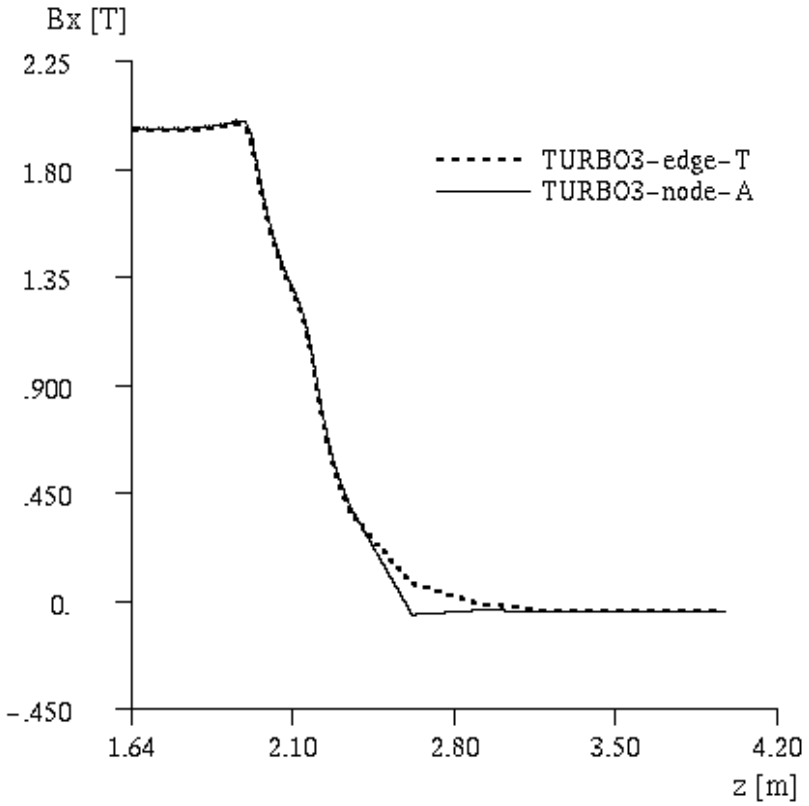

Figure 5.36 The x-component of the flux density along line A-B in the air gap of the turbogenerator model at load.

Figure 5.37 Eddy-current density distribution on the surface of the lamination stacks of the turbogenerator model at load.

5.6 Asynchronous Starting of a Synchronous Motor

5.6.1 Background

A 13 MVA, 10.5 kV four-pole synchronous motor is studied during the starting. The rotor is a salient pole rotor equipped with solid pole shoes, as shown in Fig. 5.38. The eddy currents induced in the solid pole shoes produce a starting torque, thus, eventually bringing the motor up to its operating speed. Consequently, during the starting, the motor operates as an asynchronous motor.

High eddy currents can cause high temperatures in the rotor during the starting process. In addition, the temperature distribution and, thus, the loss distribution

affect the waiting time required between subsequent starts of the motor. Therefore, measurements were carried out in order to investigate the temperature distribution arising on the rotor surface during starting. The experiments were performed in this research project at ABB Industrial Products.

To simplify the measurements, the rotor was locked in the experiments. In order to model the dependency of the field currents on the slip, the frequency of the stator voltage was varied. The amplitude of the stator voltage was also varied in order to control the flux level and the saturation. The flux level was kept under half the rated value because of the restricted capacity of the generator feeding the machine studied. Furthermore, since the rotor of the machine is a salient pole rotor, the torque pulsates and varies dependingon the position of the rotor with respect to the stator winding. Consequently, the eddy-current losses vary depending on the rotor position, whose influence on the results was also investigated. Before each measurement, the machine was cooled down in order to assure an almost homogeneous temperature in the machine.

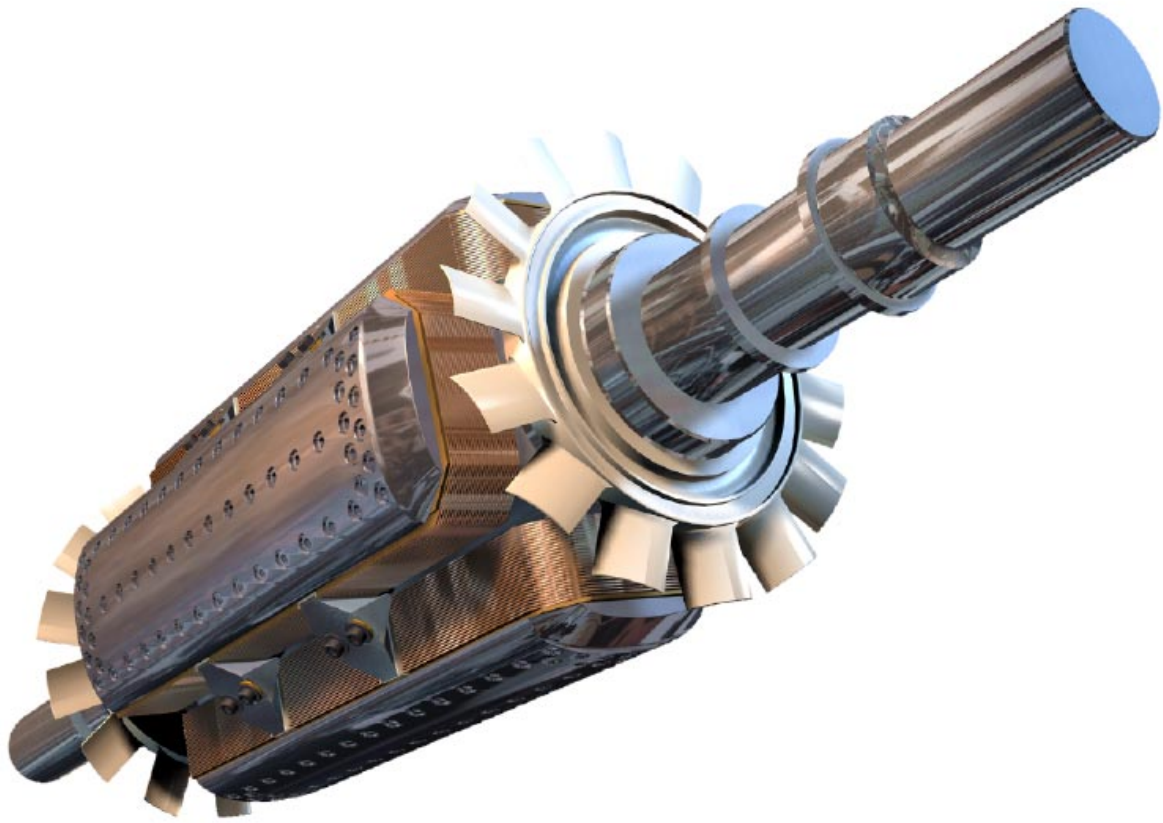

Figure 5.38 Rotor of the synchronous motor.

5.6.2 Measuring System

The adjustable frequency and voltage were obtained from a synchronous generator (GAE 1250) which fed the machine studied. The frequency was set by varying the speed of the dc machine driving the generator. The stator voltage was put on by adjusting the field current of the generator. The rotor of the machine studied was locked by means of a torque lever, and the position of the rotor was adjusted by rotating the coupling between the shaft and the torque lever. The bearings of the machine were equipped with forced oil lubrication in order to reduce the influence of friction on the measurements.

The measuring signals were recorded in each experiment by using two data acquisition systems and a sample frequency of 1000 Hz. The measured quantities and the measuring equipment are summarized in Table 5.16. The stator voltages and currents, as well as the field current and torque, were measured and recorded with one of the data acquisition systems. Magnetic flux density sensors (search coils) and temperature sensors (thermocouples) were placed on the rotor surface. Search coils were used to measure stator flux densities, and the air-gap flux density was measured by a Hall sensor. The flux densities and the temperatures were recorded with the other data acquisition system. The sampled signals obtained from the flux density and temperature sensors were anti-alias filtered with cut-off frequencies of 104,17 Hz and 90 Hz, respectively. Finally, temperatures between the coil sides of the stator winding were measured with Pt100 sensors and read before and after each experiment by using a Yokogawa hybrid recorder, type DR240. All the wires to the sensors were twisted, which reduces the unwanted voltage induced by the magnetic field in the machine.

Table 5.16 Measured quantities and measuring equipment.

Measured quantity	Measuring range	Number	Sensors
Rotor temperature	0–600 °C	12	Thermocouples (K-type)
Magnetic flux density on the rotor surface	0–2 T	12	Search coils
Magnetic flux density in the stator	0–2 T	3	Search coils
Magnetic flux density in the air gap	0–1 T	1	Hall sensor and Gaussmeter
Stator temperature	20 °C–50 °C	9	Pt 100

Stator voltage	0–4 kV	3	Voltage transformers
Stator current		3	Current transformers
Field current		1	Shunt resistor
Torque		1	Torque lever and force sensor
Frequency	50, 25, 12.5 Hz		
Rotor position	5 positions		

5.6.3 Measuring Equipment

The stator voltages were measured with voltage transformers (ABB WASA, type KGUGI 36), and the stator currents were measured with current transformers (ABB WASA, type KOWA 06A 1/E). The current of the short-circuited field winding was measured by means of a shunt resistor. The torque measurement was carried out by measuring the force, delivered by the torque lever, by a force sensor (DS Europe, type LT1A1 500 Kg) as illustrated in Fig. 5.39.

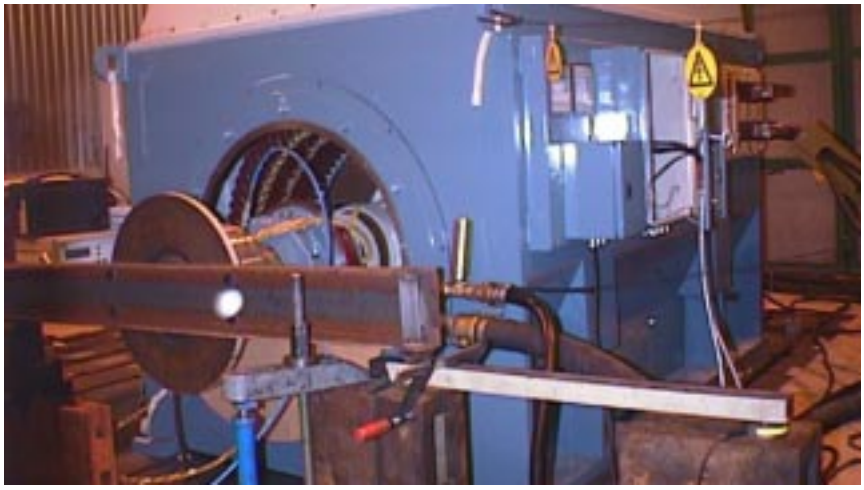

Figure 5.39 Torque lever and force sensor.

Search Coils for Measuring the Magnetic Flux Densities on the Rotor Surface

The magnetic flux densities on the rotor surface were measured with search coils as shown in Fig. 5.40. The geometry of the coils is illustrated in Fig. 5.41. The coils were made of 99 turns of fibreglass insulated nickel wire wound on a core. The insulation had a maximum temperature of 510 °C. The cores were made of macor, which is a glass-ceramic material having a low thermal expansion coefficient and which withstands a maximum temperature of 800 °C. The search coils were

fastened to the pole-shoe surface with ceramic glue withstanding a maximum temperature of 1300 °C.

Since the skin effect causes the eddy currents to circulate around the bolts fastening the pole shoes to the pole core, the maximum temperatures were expected to be there. The coil numbers and positions are shown in Fig. 5.42. Only 12 of the coils were used in the measurements; coils 11 and 12 served as a reserve.

Figure 5.40 Some search coils glued to the rotor surface.

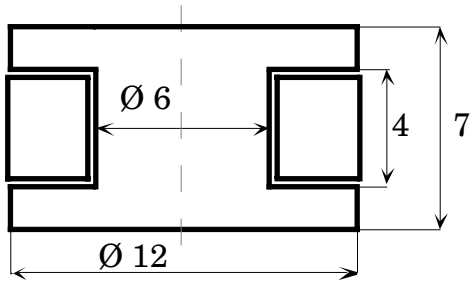

Figure 5.41 Geometry of the search coils used on the rotor surface. The dimensions are in millimeters.

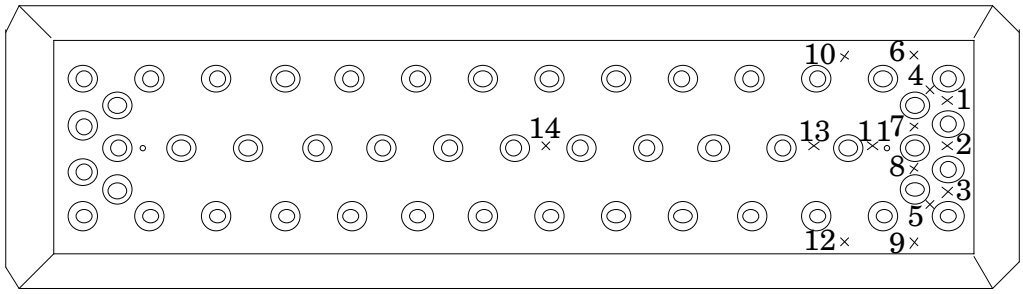

Figure 5.42 Positions of the flux and temperature sensors on the pole shoe.

Hall Sensor and Gaussmeter

The magnetic flux density in the air gap was measured with a Gaussmeter (F. W. Bell Model 9550). Either the radial or axial component of the air-gap flux was measured. In both cases, the probes were positioned in the air gap in a position corresponding to search coil number 2, but another pole shoe was used.

Thermocouples

The rotor temperatures were measured with type K thermocouples (Pentronic QTW-20K-K). The thermocouples were fibreglass insulated and had a maximum temperature of 650 °C. The thermocouples were wedged in holes drilledin the pole-shoe surface, as illustrated in Fig. 5.43. The thermocouples were numbered and positioned as the search coils in Fig. 5.42, but another pole shoe was used. Only 12 of the sensors were used in the measurements; sensors 11 and 12 served as a reserve.

Search Coils for Measuring the Magnetic Flux Densities in the Stator

The magnetic flux densities in the stator were measured with search coils made of teflon-insulated copper wire. The coils were wound (i) around a tooth in the outermost stack of the stator core, (ii) around the same tooth but in the middle stack of the stator core and (iii) around a pole pitch of the stator core. The numbers of winding turns were 5, 5 and 1, respectively. In the radial direction, the search coils were located on the air-gap side of the slot wedges. The positions of the search coils on the stator periphery are shown in Fig. 5.44.

Figure 5.43 Some thermocouples on the rotor surface.

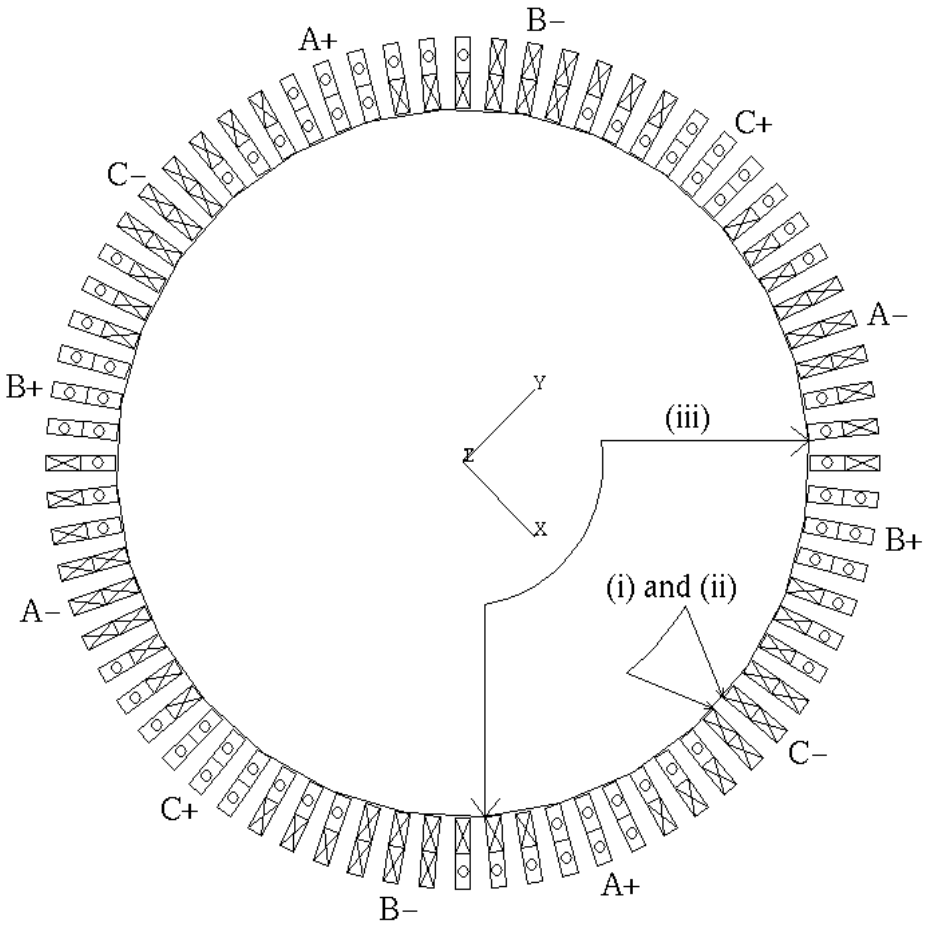

Figure 5.44 Positions of the flux sensors used in the stator. The coils were wound (i) around a tooth in the outermost stack of the stator core, (ii) around the same tooth but in the middle stack of the stator core and (iii) around a pole pitch of the stator core.

RotorPositions

A total of 5 different rotor positions were used in the measurements, as illustrated in Fig. 5.45. The position of the centerline of the pole with respect to the phase belt of phase C was used to define the rotor position. Position 1 corresponds to the middle of the phase belt, position 2 corresponds to half a phase belt, i.e., a 15 ° rotation towards the phase belt of phase B, position 3 corresponds to a 7.5 ° rotation, position 4 corresponds to a –7.5 ° rotation and position 5 to a –15 ° rotation.

5.6.4 Post-processing

The software package Matlab was used in the post-processing of the measured values. The results from the two data acquisition systems were synchronized so

that all the measured curves have the same time interval and the time interval starts as the voltage is turned on. The voltage curves of the flux density measurements (with the exception of the signal from the Gaussmeter) were integrated in order to calculate the flux densities. Then, the amplitudes and phase shifts of the fundamental-frequency components of the voltages, currents and flux densities were calculated at a time instant at which the voltage was stabilized.

The magnetic field in the machine induces voltages of stator frequency in the thermocouple leads. For the rotor temperatures, this noise was filtered with lowpass Butterworth filters of different orders and cut-off frequencies for the different stator frequencies. The slope and the mean value of a small interval of a rotor temperature signal were calculated at a time instant at which the voltage was stabilized, thus, giving an approximation of the initial slope of the temperature curve. Finally, the mean value of the different stator temperature sensor readings both before and after each experiment was calculated.

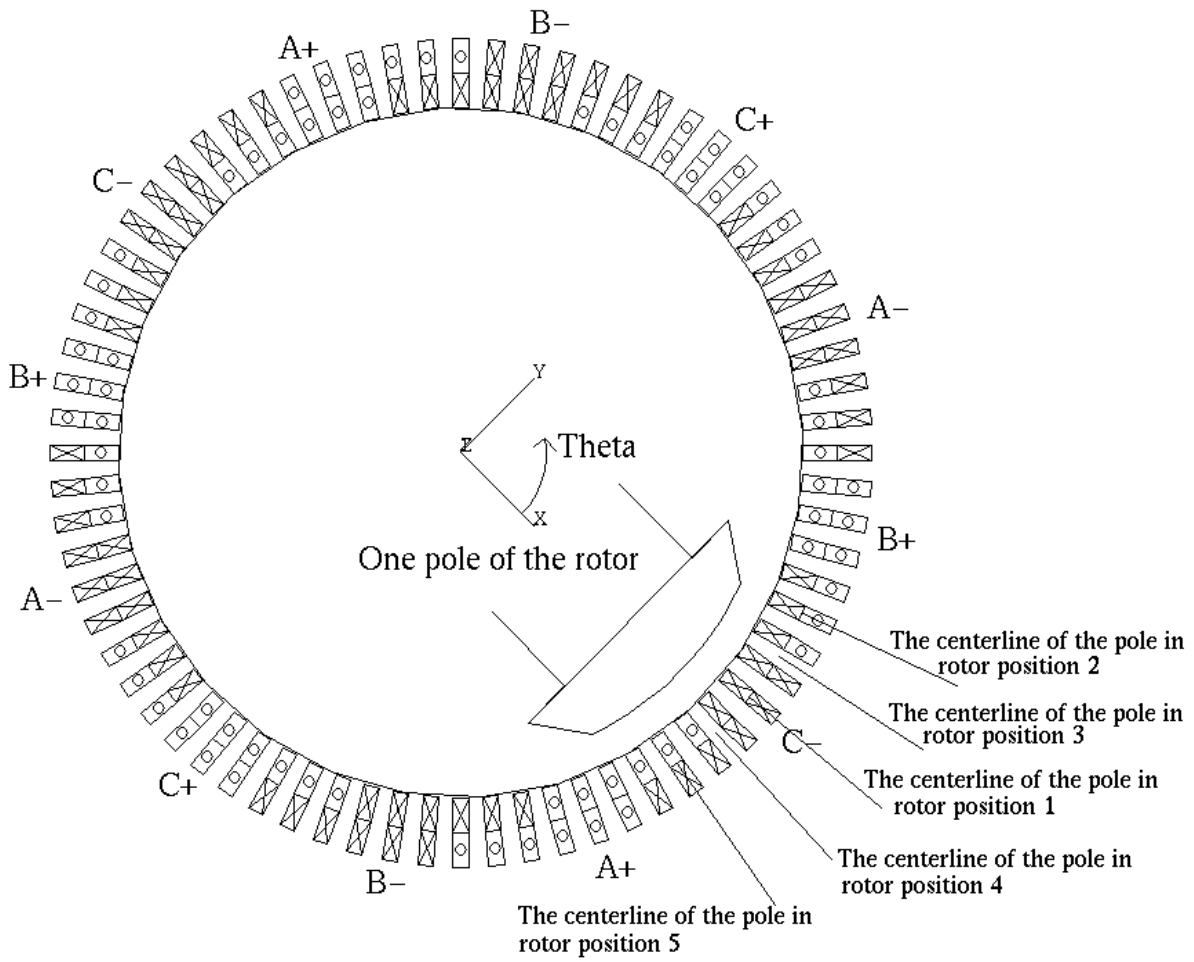

Figure 5.45 Five positions of the rotor.

5.6.5 Model of the Synchronous Motor

The model of the synchronous motor is illustrated in Fig. 5.46. The stator is represented as a Dirichlet boundary condition imposed on its surface in order to reduce the number of unknowns. The rotor consists of a solid pole shoe, pole core and rotor body. The model includes a pole pitch in the circumferential direction and extends from $z = 477$ mm to $z = 2033.5$ mm in the axial direction. The Cartesian x, y, z coordinate system has its origin in the middle of the machine shaft.

Assuming the air-gap magnetic field to be a rotating field, negative periodic boundary conditions are imposed as illustrated in Fig. 5.46. Geometric periodicity was implemented for the nodal finite elements. Cancellation problems occurred in the hydrogenerator model when the $\boldsymbol{T} - \Psi, \Psi$ formulation in conjunction with nodal elements was used. Therefore, a magnetic vector potential formulation was chosen where $\boldsymbol{A}$ was approximated by nodal basis functions. Even if the conductivity of the model studied was homogeneous, the $\boxed{\boldsymbol{A} - V, \Psi}$ formulation was used instead of the $\boldsymbol{A}, \Psi$ formulation, since the geometric periodicity was implemented for the $\boxed{\boldsymbol{A} - V, \Psi}$ formulation.

Hexahedral first-order nodal finite elements were used for the solution. The total number of nodes was 9 600, the number of nodes in the conducting region was 3 564, the number of finite elements was 7 834, the number of equations was 36 488 and the number of non-zero matrix elements was 2 532 735.

MaterialProperties

The pole shoe, pole core and rotor body form the conducting region because of the induced eddy currents in the rotor. The conductivity of the rotor was $5 \cdot 10^6$ Sm^{-1}. During starting, the magnetic flux in the rotor is greatly influenced by the skin effect, and the magnetic saturation of iron must be taken into account. This thesis, however, deals with linear eddy-current problems. The permeability of the rotor was, thus, assumed to be constant, and the relative permeability was chosen to be 526.4.

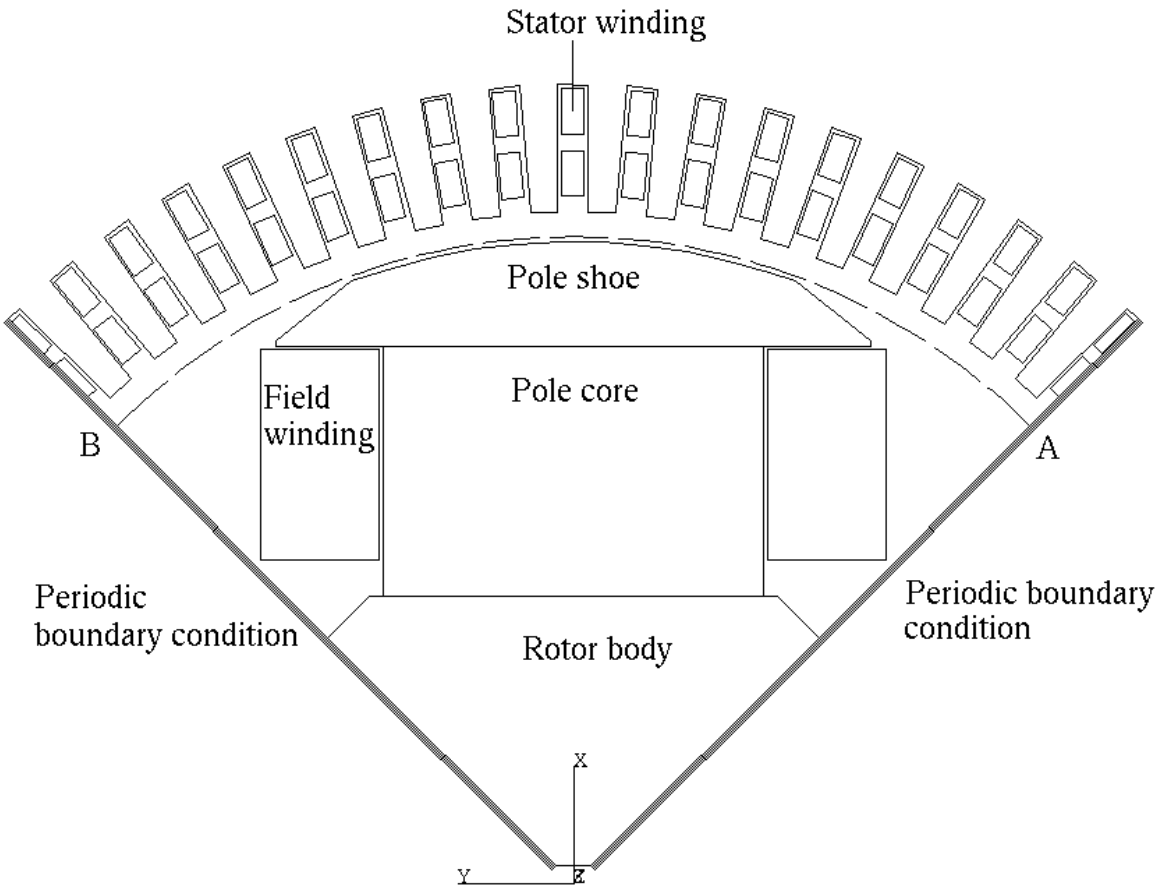

Figure 5.46 Model of the synchronous motor.

Modeling the Source Current

The stator winding is a double-layer diamond winding with 72 stator slots and 2 parallel paths. The geometrical slot angle is 5 °, and the number of slots per pole and phase is 6. The coils are short-pitched, and the coil span is 5/6 of the pole pitch. The current density is assumed to be uniformly distributed over the cross-section of the stator coils. The currents in the stator winding are given by

$$\begin{aligned} i_a(t) &= 275\cos(\omega t + 126.7^\circ) \quad \text{A} \\ i_b(t) &= 241\cos(\omega t \pm 24.4^\circ) \quad \text{A} \\ i_c(t) &= 143\cos(\omega t \pm 116.4^\circ) \quad \text{A} \end{aligned} \tag{5.3}$$

where the current amplitudes and phase shifts are obtained by the measured stator currents for the experiment corresponding to the lowest measured frequency and stator voltage; a frequency of 12.5 Hz and a stator terminal voltage of 250 V.

5.6.6 Results and Discussion

The Free-space Field

Figure 5.47 illustrates the radial component of the free-space field $\boldsymbol{H}_{\mathrm{s}}$, due to the stator winding,along a line defined by R = 464.5 mm, θ from 45 ° to 405 ° and z = 477 mm in the middle of the air gap. The cylindrical R, θ, z coordinate system has its origin in the middle of the machine shaft and the angle θ is defined in Fig. 5.45. In the stator reference frame, the space vector of the stator current is given by

$$\vec{i}_s^{\,s}(t) = \frac{2}{3}\left[i_a + e^{j\frac{2\pi}{3}}\, i_b + \left(e^{j\frac{2\pi}{3}} \right)^2 i_c \right] \tag{5.4}$$

Substituting Eq. (5.3) in Eq. (5.4) yields that at t = 0, the minimum of the fundamental wave of the field $\boldsymbol{H}_{\mathrm{s}}$ occurs at –22.7 °, which is equivalent to 337.3 °. Some harmonics observed in the curve of Fig. 5.47 cause the minimum of the curve not to lie at exactly the above mentioned angle.

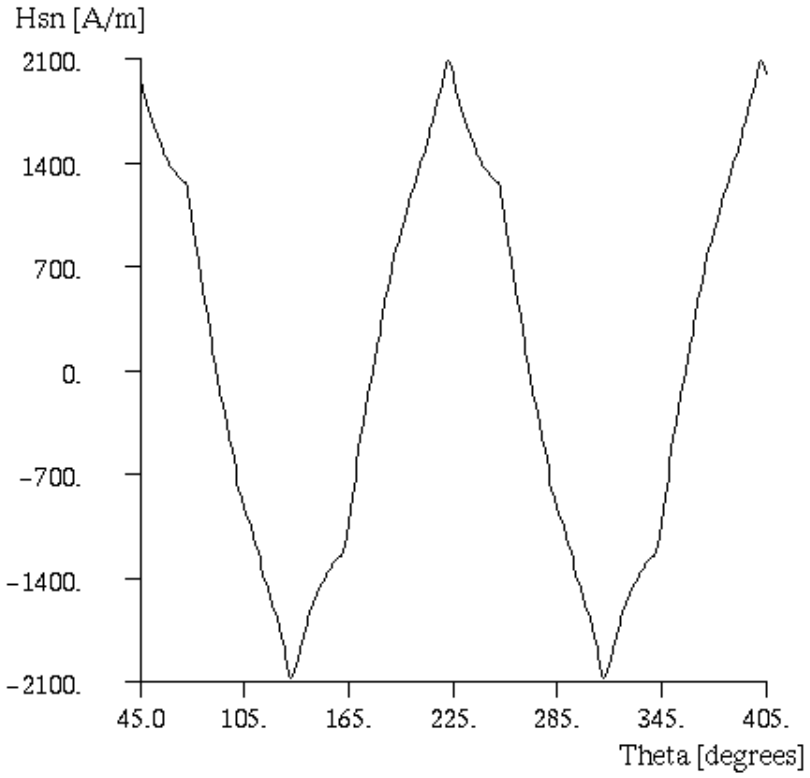

Figure 5.47 Radial component of the field $\boldsymbol{H}_{\mathrm{s}}$, due to the stator winding, in the air gap.

Field Solution of the Model and Comparison with the Measurements

The field solution of the model at the frequency of 12.5 Hz and the stator terminal voltage of 250 V is illustrated in Fig. 5.48. This figure shows the radial component of the magnetic flux density along line A-B (R = 457.5 mm, θ from –45 ° to 45 ° and z = 503.5 mm) in the air gap.

Table 5.17 shows the calculated and measured radial components of the magnetic flux density in the middle of the search coils on the rotor surface. The calculated flux densities are higher than the measured ones. The discrepancies are expected since the magnetic saturation of iron is not included in the calculations. The results demonstrate that the methods chosen work in the linear case. Consequently, the work will continue by applying a non-linear solution method to the problem in order to further investigate the synchronous motor in combination with measurements.

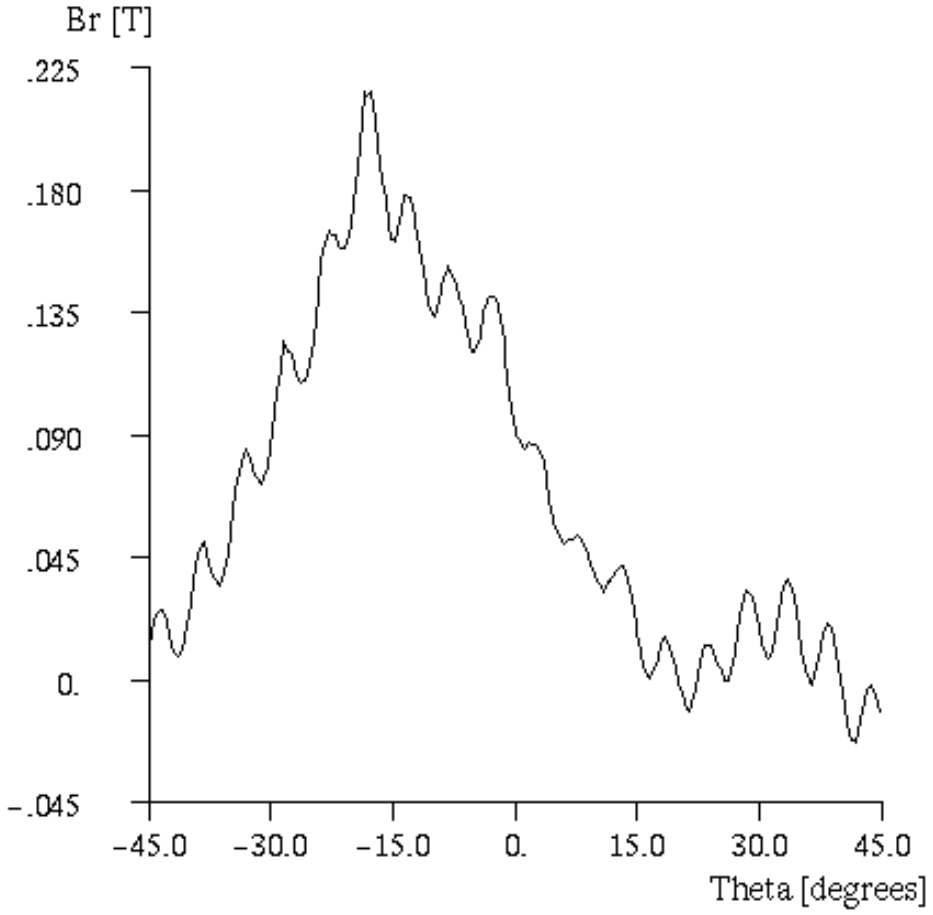

Figure 5.48 Radial component of the magnetic flux density along line A-B in the air gap.

Table 5.17 Calculated and measured radial components of the magnetic flux density in the middle of the search coils on the rotor surface. The radial and axial coordinates are in millimeters.

Search coil	Cylindrical coordinates (R, θ, z) of the middle of the search coils	Radial component of the magnetic flux density [T]	
		Calculated	Measured
1	(457.5, 9.3 °, 677)	0.229	0.077
2	(457.5, 0 °, 677)	0.279	0.081
3	(457.5, –9.3 °, 677)	0.325	0.097
4	(457.5, 11.7 °, 657)	0.219	0.075
5	(457.5, –11.7 °, 657)	0.343	0.088
6	(457.5, 16.9 °, 637)	0.179	0.068
7	(457.5, 4.6 °, 637)	0.238	0.084
8	(457.5, –4.6 °, 637)	0.298	0.086
9	(457.5, –16.9 °, 637)	0.377	0.084
10	(457.5, 16.9 °, 530)	0.069	0.061
13	(457.5, 0 °, 477)	0.084	0.064

6 Conclusions

The general aim of the work has been to evaluate the eddy-current losses in the end regions of synchronous machines efficiently. This aim has been achieved by a detailed study of various formulations and finite element types, as well as by modeling the windings and their contribution to the magnetic field.

Four finite element types were used: hexahedral and tetrahedral, first-order nodal and low-order edge finite elements. Four formulations for the solution of three-dimensional eddy-current problems were compared. Two formulations, $\boldsymbol{T}-\Psi,\Psi$ and $\boldsymbol{T}-\Omega,\Omega$, have been based on the electric vector potential $\boldsymbol{T}$ defined in the conducting region. The reduced and the total magnetic scalar potentials, Ψ and Ω, have been defined in the whole region of interest. The other two formulations, $\boldsymbol{A}-V,\Psi$ and $\boldsymbol{A},\Psi$, have been based on the magnetic vector potential $\boldsymbol{A}$ defined in the conducting region and Ψ in the non-conducting region. In the $\boldsymbol{A}-V,\Psi$ formulation, the reduced electric scalar potential V has also been defined in the conducting region. The scalar potentials Ψ, Ω and V have been approximated by nodal basis functions, whereas the vector potentials $\boldsymbol{T}$ and $\boldsymbol{A}$ have been approximated either by nodal basis functions or by edge basis functions.

The formulations chosen were first applied to two benchmark problems from International Eddy Current Workshops: the Bath Cube and the Asymmetrical Conductor with a Hole. These problems were used to compare the formulations, as well as the finite elements. Hexahedral edge finite elements give more accurate results for a given discretization than nodal elements and allow for a reduction of the computer storage and the CPU time for a given accuracy. This reduction is due to a sparser coefficient matrix. On the other hand, for a given mesh with tetrahedral finite elements, the edge elements are not favourable from the viewpoint of CPU time, number of unknowns, non-zeroes and iterations in comparison with nodal elements, especially in combination with the $\boldsymbol{A}-V,\Psi$ and the $\boldsymbol{A},\Psi$ formulations. In addition, the solution obtained by means of the tetrahedral elements is not as accurate as that obtained by means of the hexahedral elements. The $\boldsymbol{T}-\Psi,\Psi$ formulation leads to a shorter CPU time, as well as a smaller number of unknowns, non-zeroes and iterations than the $\boldsymbol{A}-V,\Psi$ formulation, but the accuracy obtained by these two formulations is roughly the same. Furthermore, the $\boldsymbol{T}-\Psi,\Psi$ formulation yields less unknowns than the $\boldsymbol{A},\Psi$ formulation, but these two formulations give roughly the same accuracy.

The use of Ω in the non-conducting region, comprising the current sources, necessitates the inclusion of these sources in the discretization. This inclusion increases the number of unknowns and complicates the construction of the finite element mesh especially in the presence of coils of geometrically complex shapes, such as the windings of electrical machines. The use of Ψ in the non-conducting region allows for the exclusion of the current sources from the discretization by evaluating the vector field $\boldsymbol{T}_0$, whose curl is the source current density. The most straightforward choice for $\boldsymbol{T}_0$ is $\boldsymbol{H}_s$, the magnetic field due to the current density in free space, which can be computed from Biot-Savart's law. On the other hand, the combination of Ψ and the nodal element representation of $\boldsymbol{H}_s$ cannot be recommended for high-permeability regions, since numerical difficulties may arise. The use of $\boldsymbol{T}$ shows a distinct advantage in laminated regions since one component of $\boldsymbol{T}$ is then enough to solve the field in these regions.

An efficient method for calculating the free-space field $\boldsymbol{H}_s$, due to the windings of electrical machines, is the surface-source modeling method based on Biot-Savart's law. A coil is subdivided into segments of the same cross-sectional area as that of the coil. The segments lie in the direction of the current density, and their sides are generally of a trapezoidal shape. The volume current density is replaced by equivalent distributions of fictitious magnetization, surface magnetic charge density and uniform surface current density. In nodal elements, $\boldsymbol{H}_s$ is first computed at the nodes of the finite element mesh of the problem studied. Then, $\boldsymbol{H}_s$ is approximated by means of the nodal basis functions. In edge elements, the line integrals of $\boldsymbol{H}_s$ are first computed along the edges of the finite element mesh. The field $\boldsymbol{H}_s$ is then approximated by means of the edge basis functions. For practical purposes, the stator and field windings of synchronous machines were parameterized for an automatic generation of winding models.

The described methods allow for the solution of the electromagnetic fields of synchronous machine problems. A 120 MVA hydrogenerator running at no load was investigated. The end-region model included a slot and half a tooth. The magnetic flux densities as well as the eddy-current losses obtained by the $\boldsymbol{T}-\Psi,\Psi$, the $\boldsymbol{T}-\Omega,\Omega$ and the $\boldsymbol{A}-V,\Psi$ formulations in association with hexahedral nodal and edge elements have been in good agreement with each other.

A 635 MVA turbogenerator running at no-load and at load was investigated. At load, the turbogenerator was overexcited and operated with a power factor of 0.85 at rated voltage and current. The end-region model included half a slot pitch. The

magnetic flux densities as well as the eddy-current losses obtained by the $\boldsymbol{T} - \Psi, \Psi$ formulation in association with hexahedral edge elements as well as by the $\boldsymbol{A}, \Psi$ formulation in association with hexahedral nodal elements have been in good agreement with each other. In the end region, the calculated eddy-current losses at load are almost twice those at no load, because of the extra losses due to the axial component of the leakage fields caused by the stator end-winding currents.

At the end of this work, a 13 MVA synchronous motor with solid pole shoes was studied during starting. Extensive measurements of the temperature and the magnetic flux density in the end regions of the motor with a locked rotor were carried out. The calculated results have demonstrated that the methods chosen work in the linear case. Consequently, future work will entail including the magnetic saturation of iron in the calculations in order to further investigate the synchronous motor in combination with measurements.

References

1 Touma, M., Lundmark, S. T., "Three-dimensional computation of eddy currents in end regions of synchronous generators". Göteborg, Sweden: Chalmers University of Technology, Department of Electrical Machines, Report No. 231L, 1996. 140p.

2 Touma, M., Tidblad, S., Luomi, J., "3D finite-element analysis of eddy-current losses in hydrogenerator end regions". *Stockholm Power Tech Conference,* Stockholm, Sweden, 18-22 June 1995, Electrical Machines and Drives, p. 379.

3 Zienkiewicz, O. C., Taylor, R. L. 1988. *The finite element method*. 4th ed. vol. 1.Maidenhead:McGraw-Hill.

4 Midtgård, O. M. 1997. "Construction and assessment of hierarchal edge elements for three-dimensional computations of eddy currents". Trondheim, Norway: Norwegian University of Science and Technology, Department of Electrical Power Engineering, 128 p.

5 Van Welij, J. S., "Calculation of eddy currents in terms of $\boldsymbol{H}$ on hexahedra". *IEEE Transactions on Magnetics* vol 21 (1985) 6, p. 2239-2241.

6 Dular, P., Genon, A., Hody, J.-Y., Legros, W., Mauhin, J., Nicolet, A., "Coupling between edge finite elements, nodal finite elements and boundary elements for the calculation of 3-D eddy currents". *IEEE Transactions on Magnetics* vol 29 (1993) 2, p. 1470-1473.

7 Barton, M. L., Cendes, Z. J., "New vector finite elements for three-dimensional magnetic field computation". *Journal of Applied Physics* vol 61 (1987) 8, p. 3919-3921.

8 Bossavit, A., "Mixed finite elements and the complex of Whitney forms". In: WHITEMAN, J.R. (ed.), *The Mathematics of Finite Elements and Applications VI*, London: Academic Press, 1988, p. 137-144.

9 Nedelec, J. C., "Mixed finite elements in R^3". *Numerische Mathematik* vol 35 (1980), p. 315-341.

10 Webb, J. P., "Edge elements and what they can do for you". *IEEE Transactions on Magnetics* vol 29 (1993) 2, p. 1460-1465.

11 Ratnajeevan, S., Hoole, H., *Finite elements, electromagnetics and design*. Amsterdam: Elsevier Science B.V., 1995. 342 p.

12 Mur, G., De Hoop, A. T., "A finite-element method for computing three-dimensional electromagnetic fields in inhomogeneous media". *IEEE Transactions on Magnetics* vol 21 (1985) 6, p. 2188-2191.

13 Nedelec, J. C., "A new family of mixed finite elements in R^3". *Numerische Mathematik* vol 50, (1986), p. 57-81.

14 Ren, Z., Vérité, J. C., "Application of a new edge element for 3-D eddy currents computation". *Beijing International Symposium on Electromagnetic fields in Electrical Engineering (BISEF'88)*, 1988, Proceedings, p. 596-599.

15 Mur, G., "Edge elements, their advantages and their disadvantages". *IEEE Transactions on Magnetics* vol 30 (1994) 5, p. 3552-3557.

16 Lee, J. F., Sun, D. K., Cendes, Z. J., "Tangential vector finite elements for electromagnetic field computation". *IEEE Transactions on Magnetics* vol 27 (1991) 5, p. 4032-4035.

17 Ahagon, A., Fujiwara, K., Nakata, T., "Comparison of various kinds of edge elements for electromagnetic field analysis". *IEEE Transactions on Magnetics* vol 32 (1996) 3,p. 898-901.

18 Kameari, A., "Calculation of transient 3D eddy current using edge-elements". *IEEE Transactions on Magnetics* vol 26 (1990) 2, p. 466-469.

19 Wang, J. S., Ida, N., "Curvilinear and higher order 'edge' finite elements in electromagnetic field computation". *IEEE Transactions on Magnetics* vol 29 (1993) 2, p. 1491-1494.

20 Yioultsis, T. V., Tsiboukis, T. D., "Development and implementation of second and third order vector finite elements in various 3-D electromagnetic

field problems". *IEEE Transactions on Magnetics* vol 33 (1997) 2,p. 1812-1815.

21 Yioultsis, T. V., Tsiboukis, T. D., "Multiparametric vector finite elements: a systematic approach to the construction of three-dimensional,higher order, tangential vector shape functions". *IEEE Transactions on Magnetics* vol 32 (1996) 3,p. 1389-1392.

22 Coulomb, J. L., Zgainski, F. X., Maréchal, Y, "A pyramidal element to link hexahedral, prismatic and tetrahedral edge finite elements". *IEEE Transactions on Magnetics* vol 33 (1997) 2, p. 1362-1365.

23 Webb, J. P., Forghani, B., "Hierarchal scalar and vector tetrahedra". *IEEE Transactions on Magnetics* vol 29 (1993) 2, p. 1495-1498.

24 Morisue, T., "Magnetic vector potential and electric scalar potential in three-dimensional eddy current problem". *IEEE Transactions on Magnetics* vol 18 (1982) 2, p. 531-535.

25 Emson, C. R. I., Simkin, J., "An optimal method for 3-D eddy currents". *IEEE Transactions on Magnetics* vol 19 (1983) 6, p. 2450-2452.

26 Rodger, D., Eastham, J. F., "A formulation for low frequency eddy current solutions". *IEEE Transactions on Magnetics* vol 19 (1983) 6, p. 2443-2446.

27 Bíró, O., Preis, K., "On the use of the magnetic vector potential in the finite element analysis of three-dimensional eddy currents". *IEEE Transactions on Magnetics* vol 25 (1989) 4, p. 3145-3159.

28 Simkin, J., Trowbridge, C. W., "On the use of the total scalar potential in the numerical solution of field problems in electromagnetics". *International Journal for Numerical Methods in Engineering* vol 14 (1979), p. 423-440.

29 Simkin, J., Trowbridge, C. W., "Which potential? A comparison of the various scalar and vector potentials for the numerical solution of the non-linear Poisson problem". Oxford, United Kingdom: Rutherford Laboratory, Report RL-78-009/B, 1978. 19p.

30 Mayergoyz, I. D., Chari, M. V. K., D'Angelo, J., "A new scalar potential formulation for three-dimensional magnetostatic problems". *IEEE Transactions on Magnetics* vol 23 (1987) 6, p. 3889-3894.

31 Webb, J. P., Forghani, B., "A single scalar potential method for 3D magnetostatics using edge elements". *IEEE Transactions on Magnetics* vol 25 (1989) 5, p. 4126-4128.

32 Bíró, O., Preis, K., Renhart, W., Vrisk, G., Richter, K. R., "Computation of 3-D current driven skin effect problems using a current vector potential". *IEEE Transactions on Magnetics* vol 29 (1993) 2, p. 1325-1328.

33 Bíró, O., Preis, K., Vrisk, G., Richter, K. R., Ticar, I., "Computation of 3-D magnetostatic fields using a reduced scalar potential". *IEEE Transactions on Magnetics* vol 29 (1993) 2, p. 1329-1332.

34 Nakata, T., Takahashi, N., Fujiwara, K., Okada, Y., "Improvements of the $\boldsymbol{T}$-Ω method for 3-D eddy current analysis". *IEEE Transactions on Magnetics* vol 24 (1988) 1, p. 94-97.

35 Hammond, P., "Use of potentials in calculation of electromagnetic fields". *IEE Proceedings* vol 129 Pt. A (1982) 2, p. 106-112.

36 Carpenter, C. J., "Comparison of alternative formulations of 3-dimensional magnetic-field and eddy-current problems at power frequencies". *IEE Proceedings* vol 124 (1977) 11, p. 1026-1034.

37 Albanese, R., Rubinacci, G., "Formulation of the eddy-current problem". *IEE Proceedings* vol 137 Pt. A (1990) 1, p. 16-22.

38 Morisue, T., "A new formulation of the magnetic vector potential method in 3-D multiply connected regions". *IEEE Transactions on Magnetics* vol 24 (1988) 1, p. 110-113.

39 Read, R. C., *Graph theory and computing*. New York: Academic press, 1972.

40 Brown, M. L., "Calculation of 3-dimensional eddy currents at power frequencies". *IEE Proceedings* vol 129 Pt. A (1982) 1, p. 46-53.

41 Albanese, R., Rubinacci, G., "Solution of three dimensional eddy current problems by integral and differential methods". *IEEE Transactions on Magnetics* vol 24 (1988) 1, p. 98-101.

42 Albanese, R., Rubinacci, G., "Integral formulation for 3D eddy-current computation using edge elements". *IEE Proceedings* vol 135 Pt. A (1988) 7, p.457-462.

43 Bíró, O., Preis, K., "Finite element analysis of 3-D eddy currents". *IEEE Transactions on Magnetics* vol 26 (1990) 2, p. 418-423.

44 Sande, G. 1993. "Computation of induced currents in three dimensions". Trondheim, Norway: Norwegian University of Science and Technology, Department of Electrical Power Engineering, 108 p.

45 Tokumasu, T., Doi, S., Ito, K., Yamamoto, M., "An electric vector potential method approach for 3-D electromagnetic field in turbine generator stator core end". *IEEE Transactions on Power Apparatus and Systems* vol PAS-103 (1984) 6, p. 1330-1338.

46 Emson, C. R. I., Simkin, J., Trowbridge, C. W., "Further developments in three dimensional eddy current analysis". *IEEE Transactions on Magnetics* vol 21 (1985) 6, p. 2231-2234.

47 Nakata, T., Takahashi, N., Fujiwara, K., Muramatsu, K., Cheng, Z. G., "Comparison of various methods for 3-D eddy current analysis". *IEEE Transactions on Magnetics* vol 24 (1988) 6, p. 3159-3161.

48 Albanese, R., Rubinacci, G., "Magnetostatic field computations in terms of two-component vector potentials". *International Journal for Numerical Methods in Engineering* vol 29 (1990), p. 515-532.

49 Kameari, A., "Three dimensional eddy current calculation using edge elements for magnetic vector potential". In: Miya, K. (ed.), *Applied Electromagnetics in Materials*, Oxford: Pergamon Press, 1989, p. 225-236.

50 Nakata, T., Takahashi, N., Fujiwara, K., Shiraki, Y., "Comparison of different finite elements for 3-D eddy current analysis". *IEEE Transactions on Magnetics* vol 26 (1990) 2, p. 434-437.

51 Nakata, T., Takahashi, N., Fujiwara, K., "Investigation of a model to verify softwares for 3-D nonlinear eddy current analysis". *IEEE Transactions on Magnetics* vol 26 (1990) 2, p. 501-504.

52 Nakata, T., Takahashi, N., Fujiwara, K., Imai, T., Muramatsu, K., "Comparison of variouis methods of analysis and finite elements in 3-D magnetic field analysis". *IEEE Transactions on Magnetics* vol 27 (1991) 5, p. 4073-4076.

53 Albanese, R., Rubinacci, G., "Numerical procedures for the solution of nonlinear electromagnetic problems". *IEEE Transactions on Magnetics* vol 28 (1992) 2, p. 1228-1231.

54 Golias, N. A., Tsiboukis, T. D., "Magnetostatics with edge elements: a numerical investigation in the choice of the tree". *IEEE Transactions on Magnetics* vol 30 (1994) 5,p. 2877-2880.

55 Albanese, R., Rubinacci, G., "Analysis of three-dimensional electromagnetic fields using edge elements". *Journal of Computational Physics* vol 108 (1993), p. 236-245.

56 Bíró, O., Preis, K., Richter, K. R., "On the use of the magnetic vector potential in the nodal and edge finite element analysis of 3D magnetostatic problems". *IEEE Transactions on Magnetics* vol 32 (1996) 3, p. 651-654.

57 Nakata, T., Takahashi, N., Fujiwara, K., Imai, T., "Effects of permeability of magnetic materials on errors of the $\boldsymbol{T}-\Omega$ method". *IEEE Transactions on Magnetics* vol 26 (1990) 2, p. 698-701.

58 Fujiwara, K., Nakata, T., Takahashi,. N., Ohashi, H., "On the continuity of the magnetizing current density in 3-D magnetic field analysis with edge element". *IEEE Transactions on Magnetics* vol 31 (1995) 3, p. 1364-1367.

59 Ren, Z., "Influence of the R.H.S. on the convergence behaviour of the curl-curl equation". *IEEE Transactions on Magnetics* vol 32 (1996) 3, p. 655-658

60 Fujiwara, K., Nakata, T., Ohashi, H., "Improvement of convergence characteristic of ICCG method for the $\boldsymbol{A}$-ϕ method using edge elements". *IEEE Transactions on Magnetics* vol 32 (1996) 3, p. 804-807.

61 Dular, P., Hody, J.-Y., Nicolet, A., Genon, A., Legros, W., "Mixed finite elements associated with a collection of tetrahedra, hexahedra and prisms". *IEEE Transactions on Magnetics* vol 30 (1994) 5, p. 2980-2983.

62 Dular, P., Nicolet, A., Genon, A., Legros, W., "A discrete sequence associated with mixed finite elements and its gauge condition for vector potentials". *IEEE Transactions on Magnetics* vol 31 (1995) 3, p. 1356-1359.

63 Bossavit, A., "Whitney forms: a class of finite elements for three-dimensional computations in electromagnetism". *IEE Proceedings* vol 135 Pt. A, (1988) 8, p. 493-500.

64 Webb, J. P., Forghani, B., "The low-frequency performance of $\boldsymbol{H}$-ϕ and $\boldsymbol{T}$-Ω methods using edge elements for 3D eddy current problems". *IEEE Transactions on Magnetics* vol 29 (1993) 6, p. 2461-2463.

65 Bossavit, A., Vérité, J. C., "A mixed FEM-BIEM method to solve 3-D eddy-current problems". *IEEE Transactions on Magnetics* vol 18 (1982) 2, p. 431-435.

66 Bossavit, A., Vérité, J. C., "The "TRIFOU" code: solving the 3-D eddy-currents problem by using $\boldsymbol{H}$ as state variable". *IEEE Transactions on Magnetics* vol 19 (1983) 6, p. 2465-2470.

67 Bossavit, A., "Le calcul des courants de Foucault en trois dimensions par éléments finis et éléments de frontières accociés". *Rev. Roum. Sci. Techn., Electrotechn. et Energ.*, vol 31 (1986) 4, p. 365-377.

68 Bossavit, A., "A rationale for "edge-elements" in 3-D fields computations". *IEEE Transactions on Magnetics* vol 24 (1988) 1, p. 74-79.

69 Vérité, J. C., "Advanced 3D electromagnetic formulations and applications". In Y.R. Crutzen et al. (ed.), *Industrial Application of Electromagnetic Computer Codes*, 1990, p. 137-160.

70 Onuki, T., Wakao, S., Shimazaki, M., "3D eddy current analysis by the hybrid FE-BE method using magnetic field intensity ***H***". *IEEE Transactions on Magnetics* vol 28 (1992) 5, p. 2259-2261.

71 Wakao, S., Onuki, T., "Electromagnetic field computations by the hybrid FE-BE method using edge elements". *IEEE Transactions on Magnetics* vol 29 (1993) 2, p. 1487-1490.

72 Keskinen, E. 1992. "Applicability of vector potentials in the finite element solution of three-dimensional eddy current problems". Helsinki, Finland: *Acta PolytechnicaScandinavica*, Electrical Engineering Series No. 71, 99 p.

73 Kristensen, T., "Konjugerte gradient type metoder med prekondisjoneringi forbindelse med FEM-analyse av elektomagnetiske felter", M.Sc. Thesis, Norwegian Institute of Technology, 1989.

74 Korneliussen, G., "Ligningslösere brukt ved beregning av elektromagnetiske felter", M.Sc. Thesis, Norwegian Institute of Technology, 1989.

75 Houbak, N., 1985. Users guide for SESYS: A sparse matrix linear equation solver. Laboratory for Energetics, Technical University of Denmark, 31 p.

76 Torsein, A., "Beräkning av härvändsinduktans". Göteborg, Sweden: Chalmers University of Technology, Department of Electric Power Engineering, Report No. 1401-6184, 1998. 82 p.

77 Urankar, L. K., "Vector potential and magnetic field of current-carrying finite arc segment in analytical form, part I: filament approximation". *IEEE Transactions on Magnetics* vol 16 (1980) 5, p. 1283-1288.

78 Hagel, R., Gong, L., Unbehauen, R., "On the magnetic field of an infinitely long helical line current". *IEEE Transactions on Magnetics* vol 30 (1994) 1, p. 80-84.

79 Lawrenson, P. J., "The magnetic field of the end-windings of turbo-generators". *IEE Proceedings* vol 108 (1961), p. 538-553.

80 Reece, A. B. J., Pramanik, A., "Calculation of the end-region field of a.c. machines". *IEE Proceedings* vol 112 (1965) 7, p. 1355-1368.

81 Urankar, L. K., "Vector potential and magnetic field of current-carrying finite arc segment in analytical form, part II: thin sheet approximation". *IEEE Transactions on Magnetics* vol 18 (1982) 3, p. 911-917.

82 Hammond, P., "The calculation of the magnetic field of rotating machines part 1.— the field of a tubular current". *IEE Proceedings* vol 133 (1959), p. 158-164.

83 Ashworth, D. S., Hammond, P., "The calculation of the magnetic field of rotating machines part 2.—the field of turbo-generator end-windings". *IEE Proceedings* vol 108 (1961), p. 527-537.

84 Tegopoulos, J. A., "Determination of the magnetic field in the end zone of turbine generators". *IEEE Transactions on Power Apparatus and Systems* vol 82 (1963), p. 562-572.

85 Okuda, H., "Calculation of magnetic field distribution in the end zone of generatorwinding". *Electrical Engineering in Japan* vol 89 (1969) 11, p. 27-33.

86 Diserens, N. J., "A search for faster magnetic field routines for curved conductors". *IEEE Transactions on Magnetics* vol 19 (1983) 6, p. 2304-2306.

87 Azzerboni, B., Cardelli,E., Tellini,A., "Computation of the magnetic field in massive conductor systems". *IEEE Transactions on Magnetics* vol 25 (1989) 6, p. 4462-4473.

88 Azzerboni, B., Cardelli, E., Raugi, M., Tellini, A., Tina, G., "Analytic expressions for magnetic field from finite curved conductors". *IEEE Transactions on Magnetics* vol 27 (1991) 2, p. 750-757.

89 Urankar, L., "Vector potential and magnetic field of current-carrying circular finite arc segment in analytical form — part V: polygon cross section". *IEEE Transactions on Magnetics* vol 26 (1990) 3, p. 1171-1180.

90 Collie, C., J., "Magnetic fields and potentials of linearly varying current or magnetisation in plane-bounded region". Oxon., UK: Rutherford Lab., Chilton, Report RL-76-037, 1976.

91 Urankar, L. K., "Vector potential and magnetic field of current-carrying finite arc segment in analytical form, part III: exact computation for rectangular cross section". *IEEE Transactions on Magnetics* vol 18 (1982) 6, p. 1860-1867.

92 Urankar, L. K., "Vector potential and magnetic field of current-carrying finite arc segment in analytical form, part IV: general three-dimensional current density". *IEEE Transactions on Magnetics* vol 20 (1984) 6, p. 2145-2150.

93 Babic, S., Krstajic, B., Milojkovic, S., Andjelic, Z., "An efficient approach for the calculation of 3D magnetostatic field of current-carrying regions of typical form". *IEEE Transactions on Magnetics* vol 24 (1988) 1, p. 423-426.

94 Babic, S., Andjelic, Z., Krstajic, B., Salon, S., "Analytical calculation of the 3D magnetostatic field of a torroidal conductor with rectangular cross section". *IEEE Transactions on Magnetics* vol 24 (1988) 6, p. 3162-3164.

95 Azzerboni, B., Cardelli, E., "Magnetic field evaluation for disk conductors". *IEEE Transactions on Magnetics* vol 29 (1993) 6, p.2419-2421.

96 Bodner, B., Köfler, H., Sammer, J., "3-Dimensional magnetic field calculation for an arrangement of S.C. coils with an outer magnetic core". *IEEE Transactions on Magnetics* vol 28 (1992) 2, p. 1402-1405.

97 Ciric, I. R., "New models for current distributions and scalar potential formulations of magnetic field problems". *Journal of Applied Physics* vol 61 (1987) 8, p. 2709-2717.

98 Ciric, I. R., "Surface source models and formulas for the magnetic field of polygonal cross section conductors". *IEEE Transactions on Magnetics* vol 24 (1988) 6, p. 3132-3134.

99 Ciric, I. R., "Simple analytical expressions for the magnetic field of current coils". *IEEE Transactions on Magnetics* vol 27 (1991) 1, p. 669-673.

100 Ciric, I. R., "Formulas for the magnetic field of polygonal cross section current coils". *IEEE Transactions on Magnetics* vol 28 (1992) 2, p. 1064-1067.

101 Cheng, D. K. 1989. *Field and wave electromagnetics*. 2nd ed. Canada: Addison-Wesley. 703 p.

102 Luomi, J. 1998. *Transient phenomena in electrical machines*. Göteborg: Chalmers University of Technology. 98 p.

103 Luomi, J. 1997. *Magnetic field calculations and electrical machines*. Göteborg: Chalmers University of Technology.

104 Slemon, G. R. 1992. *Electric machines and drives*. United States of America: Addison-Wesley Publishing Company, Inc. 556 p.

105 Turner, L., "Benchmark problems for the validation of eddy current computer codes". *COMPEL — The international Journal for Computation and Mathematics in Electrical and Electronic Engineering* vol 9 (1990) 3, p. 123-216.

106 MSC/PATRAN Installation & Operations Guide for UNIX. Publication No. 903002, Version 7.5, January 1998. The MacNeal-Schwendler Corporation, Los Angeles.

107 Kettunen, L., Turner, L. R., "How to define the minimum set of equations for edge elements". *International Journal of Applied Electromagnetics in Materials* vol 3 (1992), p. 47-53.

108 Bíró, O., "Use of a two-component vector potential for 3-D eddy current calculations". *IEEE Transactions on Magnetics* MAG-24 (1988) 1, p. 102-105.

109 Fujiwara, K., Nakata, T., "Results for benchmark problem 7 (Asymmetrical Conductor with a Hole)". *COMPEL — The International Journal for Computation and Mathematics in Electrical and Electronic Engineering* vol 9 (1990) 3, p. 137-154.

110 Touma Holmberg, M., Luomi, J., "Comparison of vector potentials and finite element types in 3D eddy-current problems". *4th International Workshop on Electric and Magnetic Fields*, Marseille, France 12–15 May 1998. Proceedings, pp. 367–372.

Appendix Treatment of the Indeterminacy of the Free-space Field $\boldsymbol{H}_{\mathrm{s}}$

The expressions obtained by Ciric [99] become indeterminate for field points lying on lines OC, DE, FG and the z"-axis of a trapezoidal side g, as illustrated in Fig. A.1, where x", y", z" is the local Cartesian coordinate system corresponding to the side g. This appendix treats the indeterminacy of the free-space field $\boldsymbol{H}_{\mathrm{s}}$ at these field points.

The trapezoidal side has either a uniform surface current density $\boldsymbol{J}_{\mathrm{sc}}$ or a surface charge density ρ_{sc}. The current density $\boldsymbol{J}_{\mathrm{sc}}$ flows in the direction of the positive z"-axis and is given by Eq. (4.15). The charge density ρ_{sc} varies linearly from $\rho_{\mathrm{sc}} = 0$ at $y" = 0$ to $|\rho_{\mathrm{sc}}| = \rho_d$ at $y" = d$ where d is the width of the side and ρ_d is given by Eq. (4.16). The field $\boldsymbol{H}_{\mathrm{s}}$ at the field point $(x"_{\mathrm{f}}, y"_{\mathrm{f}}, z"_{\mathrm{f}})$ is to be calculated in the global x, y, z coordinate system shown in Fig. 4.6.

Integrating the third and the fourth terms in the right-hand side of Eq. (4.10) on the trapezoidal side yields

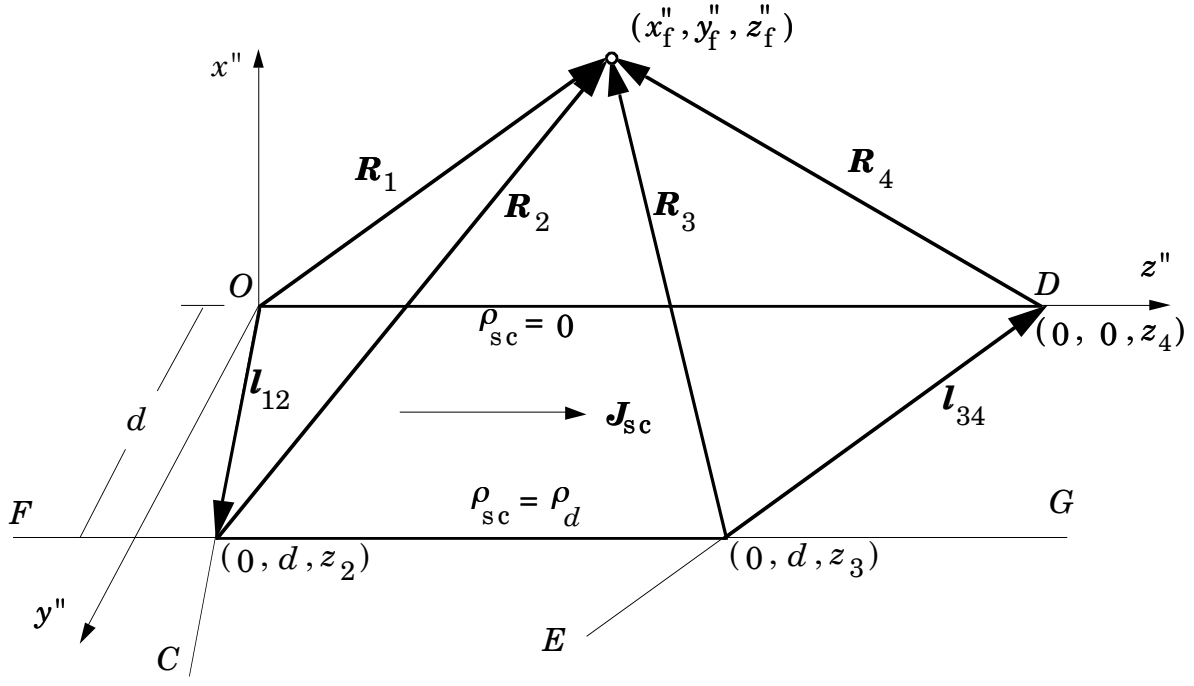

Figure A.1 Trapezoidal side of a coil segment.

$$H_{J\mathrm{sc}} = \frac{1}{4\pi}\int_{S'} \frac{J_\mathrm{c}\, a\, \boldsymbol{z}'' \times \boldsymbol{R}}{R^3}\,\mathrm{d}S' = \frac{J_\mathrm{c}\, a}{4\pi}\int_0^d \mathrm{d}y'' \int_{l_{12}(y'')}^{l_{34}(y'')} \frac{\boldsymbol{z}'' \times \boldsymbol{R}}{R^3}\,\mathrm{d}z'' \tag{A.1}$$

$$H_{\rho\mathrm{sc}} = \frac{1}{4\pi\,\mu_0}\int_{S'} \frac{\rho_d\, y''\, \boldsymbol{R}}{d\, R^3}\,\mathrm{d}S' = \frac{\rho_d}{4\pi\,\mu_0\, d}\int_0^d \mathrm{d}y'' \int_{l_{12}(y'')}^{l_{34}(y'')} \frac{y''\, \boldsymbol{R}}{R^3}\,\mathrm{d}z'' \tag{A.2}$$

where $\boldsymbol{l}_{12}$ and $\boldsymbol{l}_{34}$ are the vectors along the non-parallel sides of the trapezoid as illustrated in Fig. A.1 and $\boldsymbol{R}$ is given by

$$\boldsymbol{R} = x''_\mathrm{f}\,\boldsymbol{x}'' + \left(y''_\mathrm{f} - y''\right)\boldsymbol{y}'' + \left(z''_\mathrm{f} - z''\right)\boldsymbol{z}'' \tag{A.3}$$

with $\left(x'', y'', z''\right)$ an arbitrary source point on the trapezoidal side. Thus, Eqs (A.1), (A.2) and (A.3) yield for the x''-, y''- and z''-components of $\boldsymbol{H}_{J\mathrm{sc}}$ and $\boldsymbol{H}_{\rho\mathrm{sc}}$

$$H_{J\mathrm{sc},x''} = \frac{-J_\mathrm{c}\, a}{4\pi}\int_0^d \left(y''_\mathrm{f} - y''\right) K\,\mathrm{d}y'' = \frac{-J_\mathrm{c}\, a\, y''_\mathrm{f}}{4\pi} K_0 + \frac{J_\mathrm{c}\, a}{4\pi} K_1 \tag{A.4}$$

$$H_{J\mathrm{sc},y''} = \frac{J_\mathrm{c}\, a\, x''_\mathrm{f}}{4\pi}\int_0^d K\,\mathrm{d}y'' = \frac{J_\mathrm{c}\, a\, x''_\mathrm{f}}{4\pi} K_0 \tag{A.5}$$

$$H_{J\mathrm{sc},z''} = 0 \tag{A.6}$$

$$H_{\rho sc,x''} = \frac{\rho_d\, x''_\mathrm{f}}{4\pi\,\mu_0\, d}\int_0^d y''\, K\,\mathrm{d}y'' = \frac{\rho_d\, x''_\mathrm{f}}{4\pi\,\mu_0\, d} K_1 \tag{A.7}$$

$$
\begin{aligned}
H_{\rho sc,y''} &= \frac{\rho_d\, y''_{\mathrm{f}}}{4\pi\,\mu_0\, d}\int_0^d y''\,K\,\mathrm{d}y'' - \frac{\rho_d}{4\pi\,\mu_0\, d}\int_0^d y''^2\,K\,\mathrm{d}y'' \\
&= \frac{\rho_d\, y''_{\mathrm{f}}}{4\pi\,\mu_0\, d}K_1 - \frac{\rho_d}{4\pi\,\mu_0\, d}\;K_2
\end{aligned}
\tag{A.8}
$$

$$
\begin{aligned}
H_{\rho sc,z''} &= \frac{\rho_d}{4\pi\,\mu_0\, d}\int_0^d y''\left(K\,z''_{\mathrm{f}} - K_3\right)\mathrm{d}y'' \\
&= \frac{\rho_d\, z''_{\mathrm{f}}}{4\pi\,\mu_0\, d}K_1 - \frac{\rho_d}{4\pi\,\mu_0\, d}\;K_4
\end{aligned}
\tag{A.9}
$$

where

$$
\begin{aligned}
K &= \int_{l_{12}(y'')}^{l_{34}(y'')}\frac{\mathrm{d}z''}{R^3} \\
&= \left[\frac{1}{x''^2_{\mathrm{f}} + \left(y''_{\mathrm{f}} - y''\right)^2}\,\frac{z'' - z''_{\mathrm{f}}}{R}\right]_{l_{12}(y'')}^{l_{34}(y'')} \\
&= \frac{1}{x''^2_{\mathrm{f}} + \left(y''_{\mathrm{f}} - y''\right)^2}\left(\frac{l_{34}(y'') \pm z''_{\mathrm{f}}}{\sqrt{x''^2_{\mathrm{f}} + \left(y''_{\mathrm{f}} - y''\right)^2 + \left(z''_{\mathrm{f}} - l_{34}(y'')\right)^2}} + \right. \\
&\qquad \left. \pm \frac{l_{12}(y'') \pm z''_{\mathrm{f}}}{\sqrt{x''^2_{\mathrm{f}} + \left(y''_{\mathrm{f}} - y''\right)^2 + \left(z''_{\mathrm{f}} - l_{12}(y'')\right)^2}}\right)
\end{aligned}
\tag{A.10}
$$

$$
K_0 = \int_0^d K\,\mathrm{d}y'' \tag{A.11}
$$

$$
K_1 = \int_0^d y''\,K\,\mathrm{d}y'' \tag{A.12}
$$

$$
K_2 = \int_0^d y''^2\,K\,\mathrm{d}y'' \tag{A.13}
$$

$$
K_3 = \int_{l_{12}(y'')}^{l_{34}(y'')}\frac{z''\,\mathrm{d}z''}{R^3} \tag{A.14}
$$

$$K_4 = \int_0^d y'' K_3 \, dy'' \tag{A.15}$$

When performing the integrations in Eqs. (A.11) and (A.12) for field points lying on line FG and the z''-axis, these expressions become indeterminate. However, the expressions for field points lying on lines OC and DE can be determined and the contributions $\boldsymbol{H}_{J\mathrm{sc}}$ and $\boldsymbol{H}_{\rho\mathrm{sc}}$ of these field points are given in the following.

Field Points Lying on Line OC

By using Eqs. (A.4), (A.5) and (A.6), the components of the field $\boldsymbol{H}_{J\mathrm{sc}}$ at field points lying on line OC and produced by the surface current density $\boldsymbol{J}_{\mathrm{sc}}$ can be expressed as

$$\begin{aligned} H_{J\mathrm{sc},x''} &= \lambda' \\ H_{J\mathrm{sc},y''} &= 0 \\ H_{J\mathrm{sc},z''} &= 0 \end{aligned} \tag{A.16}$$

with

$$\begin{aligned} \lambda' = \frac{z_3 - z_4}{l_{34}} \ln\left(\frac{Q_{34} + \sqrt{{Q_{34}}^2 + {P_{34}}^2}}{Q_{34} - {l_{34}}^2 + \sqrt{\left(Q_{34} - {l_{34}}^2\right)^2 + {P_{34}}^2}} \right) + \\ + \frac{P_{34}}{|P_{34}|} \ln\left(\frac{P_{34}\left(z_2 y''_{\mathrm{f}} - z_3 d\right) + d\,|P_{34}|\,R_3}{P_{34}\left(z_2 y''_{\mathrm{f}} - z_4 d\right) + d\,|P_{34}|\,R_4} \right) + \\ + \left(\frac{z_2}{l_{12}} - \frac{P_{34}}{|P_{34}|} \right) \ln\left| \frac{y''_{\mathrm{f}} - d}{y''_{\mathrm{f}}} \right| \end{aligned} \tag{A.17}$$

where z_p with $p = 2, 3, 4$ are the z''-coordinates of the vertices of the trapezoidal side, $\boldsymbol{R}_3$ and $\boldsymbol{R}_4$ are the position vectors of the field point with respect to the vertices 3 and 4, respectively. The quantity P_{34} is equal to twice the projection of the area vector $\left(\boldsymbol{R}_3 \times \boldsymbol{R}_4\right)/2$ along the normal to the trapezoidal side, i.e.,

$$P_{34} = \boldsymbol{x}'' \cdot \left(\boldsymbol{R}_3 \times \boldsymbol{R}_4\right) \tag{A.18}$$

whereas Q_{34} is the scalar product given by

$$Q_{34} = \pm \boldsymbol{R}_4 \cdot \boldsymbol{l}_{34} \tag{A.19}$$

By using Eqs. (A.7), (A.8) and (A.9), the components of the field $\boldsymbol{H}_{\rho \mathrm{sc}}$ due to the surface charge density ρ_{sc} can be expressed as

$$H_{\rho \mathrm{sc},\, x''} = 0 \tag{A.20}$$

$$\begin{aligned} H_{\rho \mathrm{sc},\, y''} = \frac{\rho_d}{4\,\pi\,\mu_0\,d} \Bigg[& \left(\frac{d^2}{{l_{34}}^2}\,\frac{P_{34}}{l_{34}} \pm y_{\mathrm{f}}''\,\frac{z_3 - z_4}{l_{34}}\right) \\ & \ln\left(\frac{Q_{34} + \sqrt{{Q_{34}}^2 + {P_{34}}^2}}{Q_{34} - {l_{34}}^2 + \sqrt{\left(Q_{34} - {l_{34}}^2\right)^2 + {P_{34}}^2}}\right) + \\ & \pm y_{\mathrm{f}}''\,\frac{P_{34}}{|P_{34}|}\ln\left(\frac{P_{34}\left(z_2\,y_{\mathrm{f}}'' - z_3\,d\right) + d\,|P_{34}|\,R_3}{P_{34}\left(z_2\,y_{\mathrm{f}}'' - z_4\,d\right) + d\,|P_{34}|\,R_4}\right) + \\ & + \left(y_{\mathrm{f}}''\,\frac{P_{34}}{|P_{34}|} \pm \frac{z_2\,y_{\mathrm{f}}''}{l_{12}}\right)\ln\left|\frac{y_{\mathrm{f}}'' - d}{y_{\mathrm{f}}''}\right| + \\ & \pm \frac{z_2\,d}{l_{12}} \pm \frac{(z_3 - z_4)\,d}{{l_{34}}^2}\,(R_3 - R_4)\Bigg] \end{aligned} \tag{A.21}$$

$$\begin{aligned} H_{\rho \mathrm{sc},\, z''} = \frac{\rho_d}{4\,\pi\,\mu_0\,d} \Bigg[& \pm \frac{d}{l_{34}}\left(y_{\mathrm{f}}'' + P_{34}\,\frac{z_3 - z_4}{{l_{34}}^2}\right) \\ & \ln\left(\frac{Q_{34} + \sqrt{{Q_{34}}^2 + {P_{34}}^2}}{Q_{34} - {l_{34}}^2 + \sqrt{\left(Q_{34} - {l_{34}}^2\right)^2 + {P_{34}}^2}}\right) + \\ & + \frac{d\,y_{\mathrm{f}}''}{l_{12}}\ln\left|\frac{y_{\mathrm{f}}'' - d}{y_{\mathrm{f}}''}\right| + \\ & + \frac{d^2}{l_{12}} + \frac{d^2}{{l_{34}}^2}\,(R_3 - R_4)\Bigg] \end{aligned} \tag{A.22}$$

Field Points Lying on Line DE

By using Eqs. (A.4), (A.5) and (A.6), the components of the field $\boldsymbol{H}_{J\mathrm{sc}}$ at field points lying on line DE and produced by the surface current density $\boldsymbol{J}_{\mathrm{sc}}$ can be expressed as

$$
\begin{aligned}
H_{J\mathrm{sc},x''} &= \lambda'' \\
H_{J\mathrm{sc},y''} &= 0 \\
H_{J\mathrm{sc},z''} &= 0
\end{aligned}
\tag{A.23}
$$

with

$$
\begin{aligned}
\lambda'' = {} & \frac{z_2}{l_{12}} \ln\left(\frac{Q_{12} - {l_{12}}^2 + \sqrt{\left(Q_{12} - {l_{12}}^2\right)^2 + {P_{12}}^2}}{Q_{12} + \sqrt{{Q_{12}}^2 + {P_{12}}^2}} \right) + \\
& + \frac{P_{12}}{|P_{12}|} \ln\left(\frac{P_{12}\left[\left(z_3 - z_4\right)y_{\mathrm{f}}'' - \left(z_2 - z_4\right)d\right] + d\,|P_{12}|\,R_2}{P_{12}\left[\left(z_3 - z_4\right)y_{\mathrm{f}}'' + z_4\,d\right] + d\,|P_{12}|\,R_1} \right) + \\
& - \left(\frac{z_3 - z_4}{l_{34}} + \frac{P_{12}}{|P_{12}|} \right) \ln\left| \frac{y_{\mathrm{f}}'' - d}{y_{\mathrm{f}}''} \right|
\end{aligned}
\tag{A.24}
$$

where $\boldsymbol{R}_1$ and $\boldsymbol{R}_2$ are the position vectors of the field point with respect to the vertices 1 and 2, respectively. The quantity P_{12} is equal to twice the projection of the area vector $\left(\boldsymbol{R}_1 \times \boldsymbol{R}_2\right)/2$ along the normal to the trapezoidal side, i.e.,

$$
P_{12} = \boldsymbol{x}'' \cdot \left(\boldsymbol{R}_1 \times \boldsymbol{R}_2\right) \tag{A.25}
$$

whereas Q_{12} is the scalar product given by

$$
Q_{12} = \boldsymbol{R}_1 \cdot \boldsymbol{l}_{12} \tag{A.26}
$$

By using Eqs. (A.7), (A.8) and (A.9), the components of the field $\boldsymbol{H}_{\rho\mathrm{sc}}$ due to the surface charge density ρ_{sc} can be expressed as

$$
H_{\rho\mathrm{sc},x''} = 0 \tag{A.27}
$$

$$
\begin{aligned}
H_{\rho sc,\,y''} = \frac{\rho_d}{4\,\pi\,\mu_0\,d}\Bigg[& \left(\frac{d^2}{{l_{12}}^2}\,\frac{P_{12}}{l_{12}} \pm \frac{y_f''\,z_2}{l_{12}}\right) \\
& \ln\left(\frac{Q_{12} - {l_{12}}^2 + \sqrt{\left(Q_{12} - {l_{12}}^2\right)^2 + {P_{12}}^2}}{Q_{12} + \sqrt{{Q_{12}}^2 + {P_{12}}^2}}\right) + \\
& \pm y_f''\,\frac{P_{12}}{|P_{12}|} \\
& \ln\left(\frac{P_{12}\left[\left(z_3 - z_4\right)y_f'' - \left(z_2 - z_4\right)d\right] + d|P_{12}|R_2}{P_{12}\left[\left(z_3 - z_4\right)y_f'' + z_4\,d\right] + d\,|P_{12}|\,R_1}\right) + \\
& + \left(y_f''\,\frac{P_{12}}{|P_{12}|} + y_f''\,\frac{z_3 - z_4}{l_{34}}\right)\ln\left|\frac{y_f'' - d}{y_f''}\right| + \\
& + \frac{d\left(z_3 - z_4\right)}{l_{34}} \pm \frac{d\,z_2}{{l_{12}}^2}\,(R_1 - R_2)\Bigg]
\end{aligned}
\tag{A.28}
$$

$$
\begin{aligned}
H_{\rho sc,\,z''} = \frac{\rho_d}{4\,\pi\,\mu_0\,d}\Bigg[& \frac{d}{l_{12}}\left(y_f'' + \frac{z_2\,P_{12}}{{l_{12}}^2}\right) \\
& \ln\left(\frac{Q_{12} - {l_{12}}^2 + \sqrt{\left(Q_{12} - {l_{12}}^2\right)^2 + {P_{12}}^2}}{Q_{12} + \sqrt{{Q_{12}}^2 + {P_{12}}^2}}\right) + \\
& \pm \frac{d\,y_f''}{l_{34}}\ln\left|\frac{y_f'' - d}{y_f''}\right| + \\
& - \frac{d^2}{l_{34}} + \frac{d^2}{{l_{12}}^2}\,(R_1 - R_2)\Bigg]
\end{aligned}
\tag{A.29}
$$